Structure and petrology of gouge and breccia bearing shallow crustal shear zones of detachment faults in Death Valley, California

Nicholas W. Hayman

A dissertation submitted in partial fulfillment of the requirements for the degree of

Doctor of Philosophy

University of Washington

2003

Program Authorized to Offer Degree:
Department of Earth and Space Sciences

University of Washington
Graduate School

This is to certify that I have examined this copy of a doctoral dissertation by

Nicholas W. Hayman

and have found that it is complete and satisfactory in all respects,
and that any and all revisions required by the final
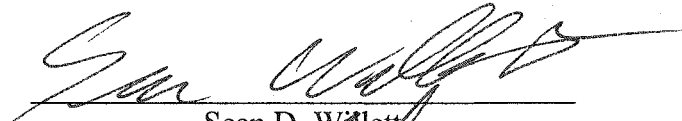examining committee have been made.

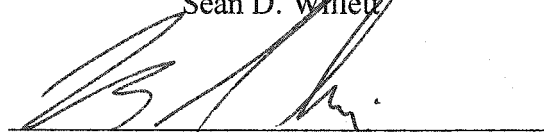Chair of Supervisory Committee:

_____
Darrel S. Cowan

Reading Committee:

_____
Darrel S. Cowan

_____
Sean D. Willett

_____
Mark Ghiorso

_____
Trenton T. Cladouhos

Date: _12/4/03_____

University of Washington

Abstract

Structure and petrology of gouge and breccia bearing shallow crustal shear zones of detachment faults in Death Valley, California

Nicholas W. Hayman

Chairperson of the Supervisory Committee: Professor Darrel S. Cowan

Department of Earth and Space Sciences

The Black Mountain (Death Valley, CA) low angle normal, detachment faults place Pliocene-Quaternary sediment against crystalline rocks. High angle normal faults extend the sedimentary section and define earthquake scarps on the valley floor. The high angle faults do not offset and are coupled with the detachments. The wedge-shaped hanging wall is critically stable when the effective friction of the detachment is weakened by roughly 50% of typical earth materials. The weakening is partly because of gouge and breccia within the detachment shear zones. The fault rocks exhibit well-developed mesoscopic foliation but do not exhibit evidence for deformation from high-temperature deformation mechanisms. Measurements of the anisotropy of magnetic susceptibility (AMS) and shape-preferred orientation (SPO) of >50-micron grains define fabric with orientations consistent with the transport and extension directions of the faults. Magnetic experiments and microscopy demonstrate that the magnetic carriers within the gouge and breccia are dominantly nanometer-to-micrometer grains that grew within the shear zones prior to the most recent deformation. The kinematic development of SPO and AMS is best treated as owing to the rotation of passive markers within a passively yielding matrix. However, the similarity of fabric defined by clasts (SPO) and matrix (AMS) is more consistent with deformation via cataclastic and granular flow, each producing distinctive microstructures. Accompanying the development of the fabric was the growth of new minerals within pore spaces and the dissemination of new minerals along reaction fronts. The youngest phases are dominantly oxides and some orthoclase and dolomite, whereas earlier phases are phyllosilicates, including polytypes of illite and chlorite with interstratified swelling clays. The mineralogy can be separated into three different

assemblages that grew along a retrograde reaction pathway. The reactions occurred between meteoric water and the footwall, over the last 6Ma, and from >120°C to near surface temperatures. Fault rock development does not appear to have been accompanied by elevated fluid pressure, or large water-rock ratios. Therefore, the weakening of the detachment and its propensity for seismic slip may be/have been dependent on the development of the new minerals and the change in deformation mechanism from cataclastic to granular flow.

Table of Contents

List of Figures

Figure number

List of Tables

Preface

Studies of fault systems in nature address one of three problems: What is the geometry of faults that bound contrasting map units or terranes? In what direction and by how much did the faults slip? How were the faults mechanically able to slip? Understanding the structure of a given region requires recognizing faults. Determining the kinematics of fault slip is essential to restore an area to its undeformed state, or find areas that are under tectonic stresses and thereby susceptible to earthquakes. Investigating the mechanisms by which large potions of the crust are able to move on meter- or even millimeter-scale surfaces is an inquiry into a great paradox with implications for understanding the earthquake process and the tectonic evolution of the crust.

The first chapter in this dissertation was published in Geology (Hayman et al., 2003) with coauthors Knott, Cowan, Nemser, and Sarna-Wojcicki. Jeffrey Knott and Andrei Sarna-Wojcicki correlated several volcanic sediments in the Black Mountains (Knott et al., 1999). During my field research of 1999 I recognized a system of high angle normal faults that, where exposed, did not offset the detachment faults. Eliza Nemser and I mapped these faults along the Black Mountain front. It soon became apparent that the system of normal faults offset the Quaternary tephra, but that extension across them must have also been accrued by the detachment. An incidental finding from this structural relationship is that the earthquake rupture that created the scarps on the valley floor must also have traveled up the detachment fault plane. Darrel Cowan and I drafted the manuscript recognizing the important implications for Death Valley research. Additional structural data and interpretations of the high angle fault system are presented in Nemser (2002). Also presented in Chapter 1 is a model that explains active slip on low angle

detachments, the Coulomb wedge model. The short Matlab script in Appendix 1 used to explore the model was written with the assistance of Drew Stolar. This model illustrates how periods of high angle faulting alternate with translation on the detachment. We propose that the properties of the detachment fault govern the structural style of extension across the hanging-wall sediment. According to the model, translation occurs when the effective friction, or resistance to shear stress, is lowered from typical values for rocks. Such weakening occurs either through the elevation of fluid pressure or the development of rocks within the faults that have anomalously low static friction. Still to be reconciled by future work is how to reconcile the kinematics of the fault system with this dynamic model. Equally important, properly relating extensional basin architecture to the range front (e.g. identifying the back-stop, determining the propagation direction of the faults) has not been adequately done.

The second chapter is a paper currently in review at Journal of Geophysical Research with coauthors Bernie Housen, Trent Cladouhos, and Ken Livi. In an effort to develop a kinematic model — a description of the motion of particles — for the deformation within the detachments, Cladouhos (1999a) determined that grains within the fault rock defined a shape preferred orientation (SPO). Bernie Housen and I measured the magnetic fabric of the fault rocks and found that the magnetic and shape fabrics had striking similarities and systematic differences. However, magnetic experiments and petrography, including Transmission Electron Microscopy attained with the assistance of Ken Livi, demonstrate that the dominant magnetic particles within the fault rock are in the fine-grained "matrix" whereas the grains used to measure the SPO are larger clasts. Therefore, all particles within the fault rock respond in a systematic and similar fashion

to strain. This finding provided a unique opportunity to implement a kinematic model and relate the SPO and AMS to different increments of strain, the net tectonic transport direction on the fault, and the type of fault rock that was accommodating the strain at a given time.

The third chapter of this dissertation starts with the assumption that the fault rocks within the detachments have some relationship with the weakening effect predicted by the Coulomb Wedge model. This weakening comes about either through fluids that permeate the fault zone, or through the development of clay minerals with a weak static friction or, as proposed here, a complex rheology of fault rocks. I explore the composition of the fault rock using data both from my own efforts, and also data collected by Peter Vrolijk and Trent Cladouhos. These data include X-ray Fluoresence (major element oxide composition) analyses of bulk rock and size-separates, powder X-ray diffraction (phase-identification), optical and electron microscopic images attained with the assistance of Dave Joswiak, Scott Kuehner, Ken Livi, and David Veblen, and particle size distribution data attained with sedigraphs and coulter counters courtesy of Chuck Nittrouer and Ron Sletten. Unlike other fault zones described in the literature, the Death Valley detachments do not exhibit hydrothermally produced compositional heterogeneity. Veins, mineral deposits, and large bulk rock compositional variation are absent. Despite the fact that the detachments appear to have been a chemically conservative system, there are several conspicuous mineralogical properties owing to fluid-rock interaction. An assemblage of hydrous clay mineral phases required a specific fluid chemistry and temperature. Using some principles of chemical kinetics and aqueous geochemistry, clay minerals can qualitatively indicate the quantity and composition of

reactive fluid interstitial to the grains within the fault rock. Other minerals present in the detachments include feldspars and oxides that also aid in developing models for the evolution of the fault rock over time. Given the data, I propose that there are at least three mineral assemblages that represent the *local equilibrium* assemblages at a given time during the evolution of the detachment. The changes in these deformation mechanisms may have coincided with changes in deformation mechanism within the detachment. If true, the weakening effect of the fault rock may not depend upon the static state of stress, but rather the dynamic response of the fault rock that is changing over time, partly in response to mineral growth.

The seed for this dissertation research was a project conducted by Darrel Cowan with post-doctoral researchers Julia Morgan and Trent Cladouhos in 1996 and 1997 on the Death Valley fault rocks. At the time I was studying thrust geometry and greenschist metamorphism of pelitic rocks. The thread that I shared, and still share, in common with the original "fault rock team" is that the interplay of fluids and particulate flow — the accommodation of strain by the rotation and translation of particles as opposed to a change in their shape — is important for slip on tectonically significant faults. While my interests broadened considerably during this dissertation research, "messy rocks", those rocks that do not have a single metamorphic assemblage or simple structure, continue to be my primary focus. Hopefully the reasons for focusing on such rocks is clear on reading this dissertation. Enjoy.

ACKNOWLEDGMENTS

Chapter 1: Quaternary low-angle slip on detachment faults in Death Valley, California.

1.1. Introduction

Low-angle normal, or detachment, faults are recognized in extended regions worldwide. Detachment faulting is a controversial process that seemingly defies a mechanical explanation despite its prevalence and its possible role in accommodating large-magnitude extension and denudation (Wernicke,1985). Two general questions are currently debated: (1) Can slip occur on normal faults that dip 30° or less (Buck, 1988; Wills and Buck, 1997)?, and (2) Is slip on detachments seismogenic (Wernicke, 1995; Jackson and White, 1989)? One reason that these questions remain outstanding is that there are few documented examples of detachment faults that have been active in the Quaternary Period (Wernicke, 1995).

The literature contains arguments for and against low-angle, normal-sense slip on detachments. For example, the rolling-hinge model for extension hypothesizes that detachments originated as steeply dipping normal faults that were tilted and became deactivated as the footwalls isostatically responded to exhumation (Buck, 1988; Wernicke and Axen, 1988). In contrast, geologic and geophysical evidence from some extended regions indicates that slip occurred on normal faults dipping ≤ 30° (Axen, 1999; Axen et al., 1999; Abbott et al., 2001). We report geologic evidence from Death Valley that strongly supports the argument that seismogenic slip occurred on low-angle normal faults in Quaternary time.

1.2. Black Mountain detachments

Death Valley is in the southwestern part of the Basin and Range province, an exemplar of intracontinental extensional tectonics. Since late Miocene–early Pliocene time, the Death Valley pull-apart basin between the Black Mountains and Panamint Mountains extended between the Northern Death Valley and Southern Death Valley dextral strike-slip fault systems (Fig. 1.1) (Burchfiel and Stewart, 1966). The extension has been accommodated on the eastern margin of Death Valley along the Black Mountains fault zone, which comprises gently (range 19°–36°, average 25°) and steeply (~60°) dipping normal faults with local oblique-to-strike-slip components (Keener et al., 1993). We studied three localities in the Black Mountains fault zone where the detachments and hanging walls are exposed above the basin floor: Badwater, Mormon Point, and South Mormon Point (Fig. 1.1). We investigated the stratigraphy and structure of the hanging walls and the relationship of faults in the hanging walls to the detachments.

In a typical exposure of a detachment fault at these localities, a well-defined principal slip plane separates the hanging wall from a 0-7 m-thick zone of gouge and breccia (Miller, 1996). Above the detachments, hundreds of steeply dipping and listric faults cut the hanging-wall sediments (Fig. 1.2). In exposures, these faults sole into or are cut by the principal slip plane, and hanging-wall sediment is locally present within the pervasively deformed fault rocks. These observations collectively indicate that slip on the detachments and on the hanging-wall faults occurred during the same interval of geologic time.
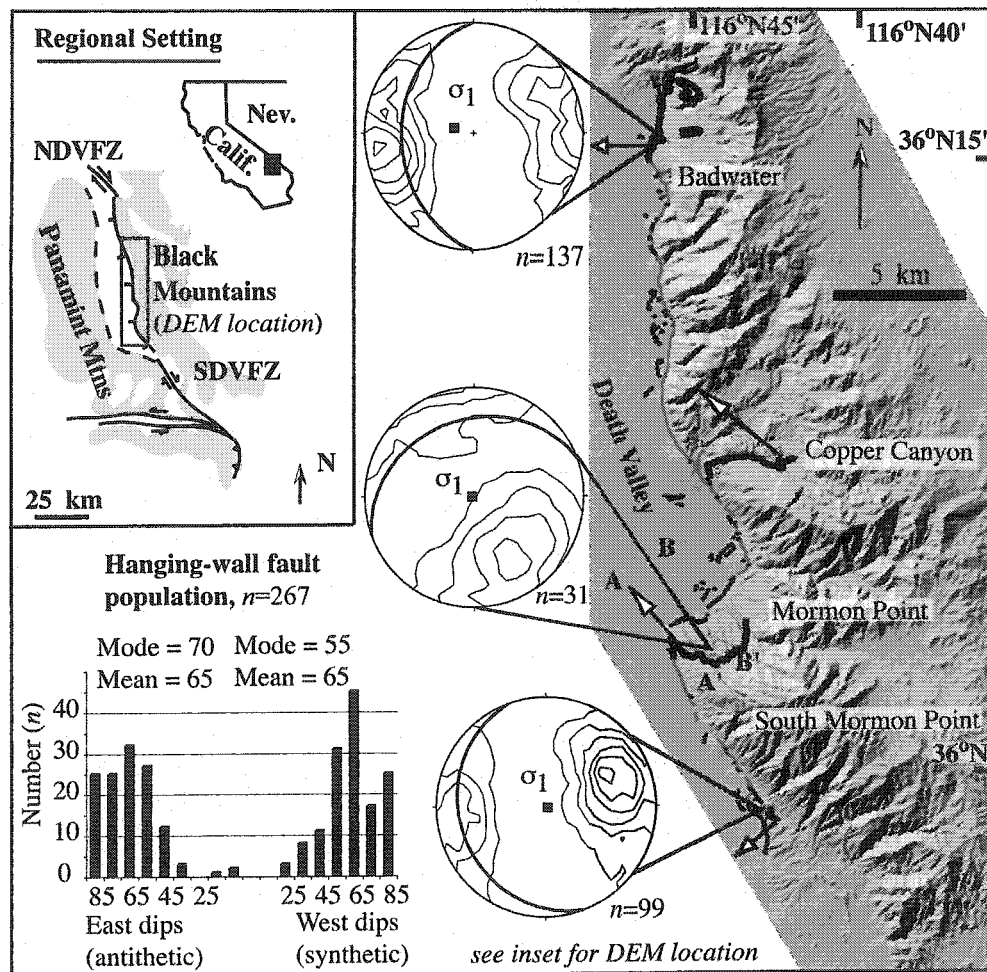
Figure 1.1. Death Valley is a pull-apart basin between Northern and Southern Death Valley fault zones (NDVFZ and SDVFZ, respectively). The Black Mountains (shown in compiled 30 m U.S. Geological Survey DEM [digital elevation model]) are bound by a fault system that consists of scarps on valley floor (traces from Brogan et al., 1991) and low-angle detachments (traces from Drewes, 1963, and Miller, 1991). Hanging walls, to the west of and above traces of detachments, consist of Pliocene to Holocene sediments. These sediments are cut by steeply dipping faults (histogram) that do not cut detachments. Stereographic projections (plotted with Stereonet by R. Allmendinger) of 2σ contours of poles to hanging-wall fault planes at each locality define modes that are synthetic (Mormon Point and South Mormon Point) and antithetic (Badwater) to detachment plane (continuous great circles). Striae on detachments (arrows) are parallel to slip direction on hanging-wall fault populations and the overall slip direction of the two fault systems is normal to range front. Orientation of maximum principal stress, σ_1, is inferred to be steep to vertical and to bisect acute angle between modes of hanging-wall fault population (histogram and square symbols on stereonet). Cross sections A–A' and B–B' are shown in Figure 1.2. Strike and Dip data is presented in Tables 1.2-1.6.
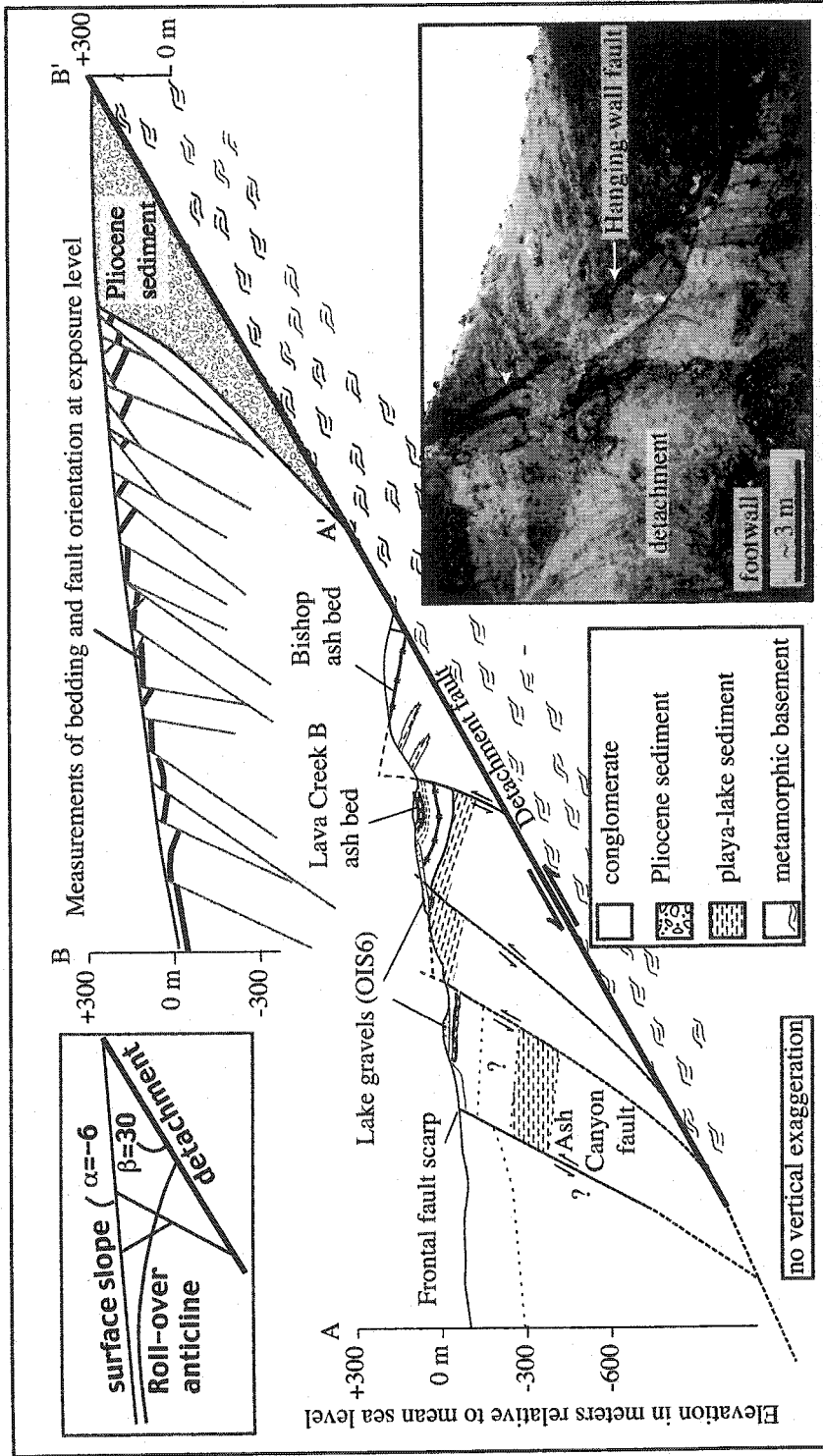
Figure 1.2. Cross-section A–A' across Mormon Point illustrating (1) sedimentary horizons of known or inferred ages and (2) amounts of slip on more significant normal faults. Intersections between hanging-wall faults are inferred where not exposed, such as depth trace of the frontal fault scarp. Projected above section A–A' is an adjacent cross section, B–B', depicting a hanging-wall rollover anticline, the density of significant faults, and the presence of Pliocene sediments at the up-dip, easternmost part of section. For locations of cross sections, see Figure 1.1. Photograph is a south-facing view of a hanging-wall fault, in Quaternary sediment, soling into the detachment at Mormon Point.

1.3. Hanging-wall tephrochronology

Sediments constituting the hanging walls at Badwater and Mormon Point were deposited in playa-lake and alluvial-fan environments that are similar to those of today. The most continuous exposures of hanging-wall sediments are at Mormon Point, where the section contains several pronounced tephra layers (Fig. 1.2). The central tephra is 100–200 cm thick and is correlated with 0.77 Ma the Bishop ash on the basis of glass composition and the nature of biotite phenocrysts (Table 1.1). The Bishop ash is also intercalated with alluvial-fan breccias at Badwater.

There are prominent tephra layers stratigraphically above and below the Bishop ash exposed at Mormon Point. The younger tephra correlates with the Lava Creek B tephra (0.64 Ma, Lanphere, et al., 2002), and the older with 0.8–1.2 Ma upper Glass Mountain tephra (Knott et al., 1999). These lower to middle Pleistocene sediments are overlain by 0.18–0.12 Ma (oxygen isotope stage [OIS] 6) Lake Manly gravel (Ku et al., 1998). At a few localities the Bishop ash is cut by gently dipping detachment faults. Most of the section above and below the Bishop ash is only slightly tilted from its depositional orientation. This evidence demonstrates that some slip on the detachments is younger than 0.77 Ma.

1.4. Hanging-wall faults

We measured the strikes and dips of 267 hanging-wall faults above the Badwater, Mormon Point, and South Mormon Point detachments (Table 1.2-1.5). There is a bimodal

distribution of the fault dips (Fig. 2.1). West-dipping faults that are synthetic to the detachments have a mode of 55° and mean of 65°, and the east-dipping, antithetic set has a less well-defined mode near 70° and a mean of 65°. Coulomb materials with an angle of internal friction of 30° fail along conjugate pairs of normal faults wherein the maximum principal compressive stress, s_1, bisects an acute angle of intersection of 60°. The modes of the fault-population data are compatible with a steep to vertically oriented σ_1. This conclusion is consistent with Andersonian mechanics, which predicts that σ_1 is normal to the Earth's surface (Anderson, 1951). Above the detachments, the surfaces of the hanging walls have a 0–6° slope (Fig. 1.2). We argue that the near-vertical σ_1 indicates that neither the strata in the hanging walls nor the populations of normal faults have been tilted more than a few degrees.

The hanging-wall faults are *kinematically coupled* with the detachments: The general directions and amounts of slip observed on the hanging-wall faults have been equivalently resolved on the detachments, and the detachments and the hanging-walls have not independently tilted. The evidence for kinematic coupling of the two fault systems includes the following: (1) We note that none of the observed hanging-wall faults cuts completely across a principal slip plane and related fault rocks (Fig. 1.2). Moreover, many hanging-wall faults are listric and curve to join the principal slip plane. (2) The mode of the strikes of the hanging-wall fault populations at each locality is parallel to the local strike of the related detachment (Fig. 1.1). (3) There is a normal sense of separation of strata across exposed faults, and a net down-to-the-west or –northwest throw across the population of faults. The presence of a conjugate set in the bulk

population is consistent with dip-slip on the hanging-wall fault system. (4) Striae on the principal slip planes of the detachments are parallel to the modal dip direction of the hanging-wall faults and the direction of net extension across the hanging-wall fault system (Table 1.6).

We note that there are striae and other kinematic indicators recording lateral and oblique slip on parts of the Black Mountain fault system (Keener et al., 1993). Local deviations from pure dip-slip on the faults that we studied are spatially coincident with the hinges of the lower-plate antiforms (Wright et al., 1974; Holm et al., 1994), unmapped irregularities in the detachment surface (Nemser, 2001), or the influence of dextral slip on the Northern and Southern Death Valley fault zones (Keener et al., 1993).

1.5. Discussion

1.5.1. Age of Slip and Original Orientation of the Detachments

At Mormon Point and Badwater the Bishop tephra (0.77 Ma) is directly cut by the detachment, and the youngest sediment in the overlying strata is the 0.18–0.1 Ma (OIS 6) gravel. These Quaternary strata are relatively flat lying except in a rollover anticline (Fig. 1.2) where a significant listric hanging-wall fault places the Quaternary section against Pliocene sediment. The high-angle fault system that cuts the entire Quaternary section is kinematically coupled with the detachment. Moreover, the modes of the fault populations are most compatible with a s_1 that is normal to the surfaces of the hanging walls. Collectively, these observations are evidence that the detachments have not tilted from an

initial dip of 19°–36°. Any kinematic model for detachment tilt without corresponding hanging-wall tilt would conflict with these observations and would require structures that are not observed (e.g., young breakaway basins or extensional duplexes).

The field relationships only require that the detachment and hanging-wall fault system slipped since 0.18–0.1 Ma. However, slip restricted to the last 0.18 Ma would be incompatible with the observed extension across the fault system. We estimate ~600 m net horizontal extension, or roughly 14% elongation along the now-5 km NW-SE section across the high-angle faults in the Quaternary sediments at Mormon Point. This estimate is derived from hundreds of small-displacement (<1m) normal faults and several large-displacement (>10-100m) faults (Fig. 1.2) and is a minimum because it does not include translation on the detachments that was unaccompanied by hanging-wall deformation. We adopt a value for slip rates of <1 mm/yr, supported by geodesy and paleoseismology of the Basin and Range (Wernicke et al., 2000). For example, 600 m of extension since the deposition of the 1.2 Ma upper Glass Mountain tephra would have proceeded at an average slip rate of 0.5 mm/yr.

The Pliocene sediments above the Copper Canyon detachment, and correlative sediments at Mormon Point and Badwater, contain a similar hanging-wall fault system (Table 1.7, 1.8)(Holm et al., 1994). The kinematics in these older sections are more complicated to reconstruct than in the Quaternary section yet are compatible with coupled slip on low-angle detachments and hanging-wall faults in Pliocene time.

1.5.2. Application of the Extensional Coulomb Wedge Model

Our observations and inferences concerning Quaternary slip on detachment faults are at odds with most models for detachment faulting. For example, a strict application of the rolling-hinge model predicts that low-angle detachments are inactive in the shallow crust (Buck, 1988; Wernicke and Axen, 1988). Other models for the initiation of, and slip on, low-angle normal faults involve rapid extension rates, the rotation of the stress field relative to the fault plane, or the elevation of fluid pressure (Wills and Buck, 1997). To provide an alternative explanation for active slip on this fault system we propose that the wedge-shaped sedimentary sections along the Black Mountains are extensional Coulomb wedges (Fig. 1.3) (Xiao et al., 1991). This model predicts that a critically or subcritically tapered wedge is stable and therefore can slide on a detachment without undergoing internal deformation. Hanging-wall wedges that have tapers greater than critical, however, will fail and extend by normal faulting in the hanging wall; slip on each fault is resolved onto the detachment.

One control on the maintenance of the critical taper is the effective basal friction of the detachment (μ_{eff}). When μ_{eff} is lowered from typical values of 0.6-0.85 ($\phi=30°$, $\mu=\tan(\phi)$) the detachment is weakened. One mechanism for weakening could be the development of fault rocks with unusually low static friction (μ). Alternatively, if the ratio of fluid pressure to lithostatic pressure along the detachment (λ_b) is higher than that within the wedge (λ), then $\mu_{eff}=\mu[(1-\lambda_b)/(1-\lambda)]$ and $\mu_{eff}<\mu$. We use the observed taper at
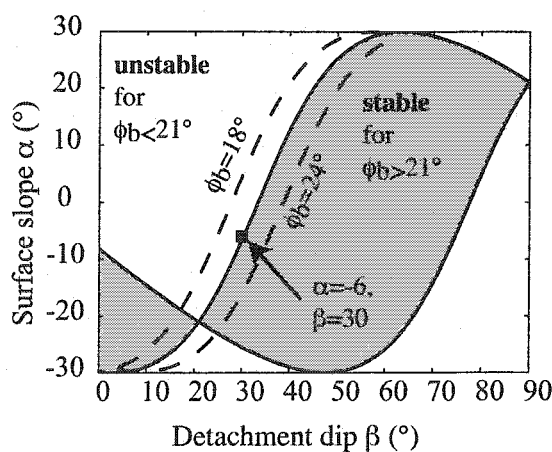
Figure 1.3. The solution to the extensional critical Coulomb wedge problem described by Xiao et al. (1991) is: $\alpha+\beta= \psi_1-\psi_0$ where a is the surface slope, β is the detachment dip, ψ_0 is the stress-angle, and ψ_1 is a function of friction, ϕ, basal friction, ϕ_b, and a. As explained by Dahlen (1984), ψ_1 is a periodic function with two minima and the extensional solution is for $-\pi/2<\psi_0<0$. Thus, any given α and β has two critically stable solutions that we solved for numerically and plot here as the curves bounding the shaded region. Any α and β that plots on this curve or within the shaded region, is either critically stable or stable, respectively, and can translate down the detachment dip without internal faulting. Any α and β that plots within the un-shaded region is unstable and hanging-wall faulting is required for the wedge to accommodate tectonic extension. The mechanisms for maintaining criticality vary in nature, but we consider fb to be the controlling parameter wherein, for the wedge at Mormon Point (α=-6, β=30), the wedge is critically stable for ϕ_b=21. However, if $\phi_b>21$, then the boundary for the stability field would shift to the right (the dashed line for ϕ_b=24) and the wedge would become unstable. Alternatively, if $\phi_b<21$ then the boundary would shift to the left (the dashed line for ϕ_b=18) and the wedge would become stable. The mechanism for changes in the friction of the detachment could be either the presence of fault rocks with anomalously low friction, or elevated fluid pressure.

Mormon Point with a surface slope (α) of -6° and a basal dip (β) of 30° (Fig. 1.2), and we

assume that the sediment is cohesionless, that λ does not deviate from hydrostatic

throughout the wedge, and that ϕ=30° for the wedge materials. The extensional solution

to the Coulomb wedge problem (Fig.1.3) (Appendix 1) (Dahlen, 1984; Xiao et al., 1991)

predicts that when μ_{eff}>0.4 or ϕ_b >21°, then the observed taper is supercritical. If the

detachment were to be weakened such that $\phi_b\leq 21°$ then the wedge would be stable or

critically stable. If m=0.6-0.85 for the fault rocks within the detachment, then the fluid

pressure is the dominant control on detachment weakening requiring that λ_b=0.7 for

λ=0.5; the latter is a nominal value for the hydrostatic fluid pressure. Such an elevation of

fluid pressure within a fault zone is within the range of measured fluid pressures within

faults (Xiao et al., 1991). Regardless of the assumptions used to apply the model or the

mechanism for the modest weakening of the detachment, the extensional Coulomb wedge

model adequately describes the behavior on the Black Mountain fault zone.

1.5.3. Seismic Slip on the Detachments

The Black Mountains fault zone includes range-front fault scarps in upper

Pleistocene or Holocene alluvial-fan and playa sediments (Fig. 1.1) (Brogan et al., 1991).

The scarps are the surface expression of steeply dipping faults that in central Death

Valley accrue dominantly normal slip (Brogan et al., 1991). The intersections of the

frontal faults and the detachments are buried beneath the valley floor (Fig. 1.2). It has

been argued that either the frontal faults resolve themselves on the detachments

(Hamilton, 1988; Burchfiel et al., 1995) or, alternatively, cut the detachments at depth

(Miller, 1991; Keener et al., 1993; Chichanski, 2000). In the latter case, Holocene and possibly older slip on the frontal faults would have superseded any slip on the detachments and necessarily deactivated them.

We propose that the steep frontal faults belong to the larger population of hanging-wall faults that resulted from extension of the hanging-wall wedges. It is probable that some of the members of the population that are now situated above the floor of the valley once defined the mountain front, just as the youngest scarps do today. According to our hypothesis, the frontal faults do not cut the buried downdip continuations of the detachments; rather, slip on them is kinematically coupled to slip on the buried detachments. If our hypothesis is true, then the seismic ruptures thought to be responsible for the young scarps in Death Valley (Brogan et al., 1991) must have propagated up the detachment faults. Our proposal that at least some slip on the detachments was seismogenic accords with recent interpretations made elsewhere in the Basin and Range Province (Axen, 1999; Axen et al., 1999; Abbott et al., 2001).

1.6. Conclusions

Structural and stratigraphic data from the hanging wall of the Black Mountain detachments require that the detachments accrued low-angle, normal-sense slip in the Quaternary, likely since the Pliocene and into Recent time. The detachment slip was coupled with slip on a system of high-angle faults in the hanging wall. A modest slip rate, a steep to vertically oriented principal stress, and the angular relationship between the surface of the hanging walls and the detachments support the best mechanical explanation

for detachment faulting in this setting: The sediment overlying the detachment forms an extensional Coulomb wedge. Our conclusions lead to the interpretation that the seismic slip that created the high-angle fault scarps on the valley floor originated on the detachments at depth.

Table 1.1. Electron microprobe analysis of volcanic glass shards from middle Pleistocene tephra layers, Death Valley, California, and comparative compositions

Sample	SiO$_2$	Al$_2$O$_3$	Fe$_2$O$_3$	MgO	MnO	CaO	TiO$_2$	Na$_2$O	K$_2$O	Total(O)*	S.C.[†]
JRK-DV-99	77.1	13	0.69	0.03	0.03	0.43	0.05	3.37	5.34	93.6	1.0000
JRK-DV-93	76.8	13.2	0.7	0.03	0.03	0.43	0.05	3.54	5.21	91.9	0.9942
OL92-1024#	76.9	13	0.7	0.03	0.03	0.44	0.05	4.04	4.85	95.2	0.9937
BT-7	77.5	12.6	0.76	0.03	0.03	0.45	0.05	3.86	4.66	94.6	0.9758
JRK-DV-42	77.6	12.6	0.72	0.03	0.03	0.44	0.06	3.78	4.7	94.3	0.9622
JRK-DV-43	77.3	12.9	0.76	0.03	0.03	0.44	0.06	4.2	4.34	93.9	0.9588
Standard** (wca)	75.7	11.4	2.12	0.05	0.15	0.12	0.21	5.25	4.53	99.6	
Standard‡ (ema)	74.9	11.5	2.12	0.05	0.15	0.1	0.19	5.15	4.42	98.5	
±s	0.65	0.1	0.04	0.01	0.01	0.01	0.01	0.16	0.05	0.65	

Provided by Jeffrey Knott

Values given are in weight-percent oxide, recalculated to 100% fluid-free basis.

*Total (o) - original oxide totals before recalculation are given to indicate the

approximate degree of hydration of the volcanic glass.

†S.C. – similarity coefficient of Borchardt and others (1972) using Si, Al, Fe, Ca and Ti

for quantitative comparisons of the tephra samples where 1.0000 represents a

perfect match.

#Data for correlative samples: OL92-1024: Bishop air-fall ash, Owens Lake, Calif. core,

312 m below ground surface (Sarna-Wojcicki and others, 1997); BT-7: Base of

Bishop ash-flow tuff, 11 km N. of Bishop, Calif. (~0.77, Sarna-Wojcicki and others,

2000)

**Standard (wca): wet chemical analysis (Macdonald and others, 1992).

‡Standard (ema): electron-microprobe analysis reported here. Charles E. Meyer and

James P. Walker, analysts, U.S. Geological Survey, Menlo Park, Calif.

Table 1.2. Orientation data of Eliza Nemser. Hanging-wall faults at Badwater and South Mormon Point. See Nemser (2001) for more detailed information.

Badwater						South Mormon Point					
Strike	Dip	Direction	Strike	Dip	Direction	Strike	Dip	Direction	Strike	Dip	Direction
28	75	SE	320	64	NE	358	85	E	15	60	E
0	55	E	190	54	SE	149	55	SW	353	67	E
0	85	E	355	90		338	75	NE	3	68	E
170	86	SW	60	60	S	343	80	NE	352	64	E
179	82	SW	345	64	E	143	70	SW	130	63	SW
335	72	NE	175	80	W	355	77	NE	245	90	
175	84	SW	175	84	W	339	56	NE	115	50	SW
0	80	E	354	42	E	345	71	NE	168	50	W
0	58	E	345	78	E	295	57	N	168	90	
180	82	W	355	85	E	115	47	S	325	90	
0	59	E	30	69	E	20	76	SE	140	85	SW
345	54	NE	338	75	NE	10	81	SE	335	90	
197	76	NW	154	32	W	30	70	SE	30	70	SE
18	68	SE	10	90		29	80	SE	200	35	NW
40	66	SE	155	49	S	46	80	SE	200	55	NW
28	84	SE	288	90		35	73	SE	5	58	SE
17	84	SE	133	55	S	34	57	SE	25	65	SE
213	59	NW	140	55	SW	67	55	S	30	76	SE
207	88	NW	145	68	SW	178	87	W	190	39	NW
196	65	NW	145	60	SW	230	90		169	49	SW
352	80	NE	155	55	SW	330	90		325	42	NE
358	49	E	155	57	SW	340	65	E	170	55	SW
176	74	W	138	60	SW	345	64	E	123	48	SW
47	70	E	135	40	SW	357	62	E	40	70	SE
329	60	E	135	84	SW	323	90		32	90	
141	81	W	145	52	SW	309	54	E	247	64	NW
178	66	W	155	89	SW	320	78	NE	205	60	NW
335	69	E	148	66	SW	130	50	SW	160	60	SW
158	76	W	145	25	SW	350	50	NE	150	35	SW
342	85	E	49	65	SW	335	50	NE	150	40	SW
158	84	SW	349	64	NE	345	86	NE	320	62	NE
340	62	NE	149	78	SW	320	40	NE	345	55	NE
345	60	NE	165	78	SW	350	45	NE	349	80	W
320	58	E	320	75	NE						
48	86	S	358	80	E						

Table 1.3. Paced Transect across South Mormon Point

strike	dip	direction	Pace direction	Paces (0.5m/pc)	Order of magnitude (in meters) throw	Notes
165	55	W	N25-40 E		1	
350	69	E			10	
305	90			60	1	
175	55	W			1	
150	65	W		103	1	
160	60	W		237		right lateral?
215	75	W		245		right lateral?
355	90			280		right lateral?
205	75	W		292	10	
180	45	W	N10E		1	
170	55	W			1	
150	60	W		40	10	
310	90			53	1	top of listric
160	65	W				bottom of listric
350	50	E		69		
155	80	S		100		
180	50	W		160		
60	90			205		
10	90					
160	60	W	in slot canyon			
210	20	W		12	1	
180	75	W		42	1	
175	60	W		56	1	
340	90			149	1	
140	60	W		159	1	
177	90	S	north	7	1	
175	55	W		24	1	
130	55	S		37	1	
145	55	W		56	1	listric
180	35	W		101	1	normal
105	40	S			1	
150	65	W	South slot		1	cuts below
355	70	E			1	
170	70	W		26	1	
335	70	E			1	
140	55	W			1	horse tails
160	70	W			1	on low angle structure
335	70	E			1	
355	70	E	adjacent wash	2	1	right lateral?
345	65	E				Cuts colluvium
350	70	E		36		

Table 1.3. Continued

strike	dip	direction	Pace direction	Paces (0.5m/pc)	Order of magnitude (in meters) throw	Notes
300	75	N		400	10	
140	65	S		414	1	
10	75	E			1	
95	60	S		485	1	
160	30	W		535	1	
125	70	S			100	
190	35	W		698	10	
230	60	W			1	
100	58	W			1	
340	60	W			1	w/ detachment
20	55	E	2nd canyon north		1	
0	90					
175	75	W	060 trend		1	
355	60	E			1	
150	70	W		75	1	
165	65	W		110	1	
330	62	E		147	1	
205	62	W	eastern wing of wash	127	1	
125	50	S	slope ~15deg			
135	65	W			1	
165	45	W		150	1	
30	60	E	next wash	116	10	fault rocks
168	30	W	S60E	20	1	

Table 1.4. Paced transect across Badwater.

strike	dip	direction	Pace direction	Paces (0.5m/pc)	Order of magnitude (in meters) throw	Notes
210	68	W	Badwater (D1)			
210	65	W	Little Amphitheater			
0	60	E	Natural Bridge			
175	60	W				
15	70	E				
195	55	W	slot	10		
125	55	W				
135	45	W		15		
165	59	W		25		
165	89	W	At the bridge	88		
25	8	E		175		
335	8	E		300		
290	75	E		312		
330	65	E		505		
260	40	W	UP fault (Elf)			
195	64	W				red /grey contact
350	70	E				
180	79	W				
215	80	W	South of Elf			
5	80	E			10	
10	72	E			1	3 faults
200	55	W			10	
80	45	E			100	4 faults
0	45	E	Nose Canyon			
180	65	W	Up faults			
195	60	W	Up faults			
195	65	W	south of Nat. BR.			
172	60	W	next canyon south			
190	70	W			1	
30	70	E			1	
0	90				10	
230	65	W	next canyon south			

Table 1.5. Mormon Wash transect

Strike	Dip	Dip Direction	Location (X)	Location (Y)	Location (Z)	Distance on transect	Throw (order of magnitude)	kinematics
260	65	N	-210	7	632	211	1	bedding offset down-dip
245	70	W	-259	9	629	259	1	bedding offset down-dip
285	69	N	-295	10	626	295	1	bedding offset in thrust sense
285	80	N	-595	20	605	597	1	
270	63	N	-805	41	589	808	1	listric fault
270	70	N	-805	41	589	808	1	
90	65	S	-877	44	584	881	10	bedding offset down-dip
270	55	N	-1304	215	552	1325	10	bedding offset down-dip
245	55	N	-1437	237	542	1460	10	listric fault
230	80	W	-1542	254	535	1567	10	mixed sense
270	80	N					1	bedding offset down-dip
10	52	S	-2200	778	475	2340	10	
200	55	W	-2271	803	469	2416	10	
20	45	S	-2271	803	469	2416	10	
240	55	N	-2663	951	440	2835	10	striae and grooves : mixed sense
205	65	N	-2663	951	440	2835	10	striae and grooves : mixed sense
215	60	W	-3099	1258	399	3354	10	
205	50	W	-3222	1307	389	3486	10	mixed sense
50	80	S	-3091	1712	378	3544	1	
235	60	W	-3394	1880	352	3891	1	
212	40	W	-3442	1907	348	3946	1	
78	67	S	-3616	2003	333	4146	1	
210	40	W	-3664	2030	329	4201	10	bedding offset down-dip
80	70	S	-3730	2066	323	4276	10	striae are transverse
230	39	N	-3730	2066	323	4276	1	
230	30	N	-3730	2066	323	4276	1	
205	65	W	-3811	2111	316	4369	1	
190	25	W	-3921	2172	306	4495	1	mixed sense
90	70	S	-4559	2639	252	5282	1	
220	60	W	-4634	2682	246	5369	1	bedding offset down-dip
30	15	E	-4797	2777	231	5558	1	above Willow Spring Fault

Table 1.6. Detachment faults and kinematic indicators. UTM coordinates are approximated.

Location	UTM	UTM	Strike	Dip	Direction	Trend	Plunge	Direction	Comment
Copper Canyon									
Basalt Ramp	3998000	524000	192	23	W	270	20	N	striae
			164	24	W	220			
			106	30	S				
			122	44	S	212	44		striae
Lower Corrugations	3997750	523700	200	20	W				
			55	15	W	310	12	W	striae
			213	54	W	317	54		striae
			85	15	N				
			65	25	N	288	17		striae
			175	40	S				
			167	35					
			185	25					
Range-front	3997200	523300	172	40	W				striae
Mormon Point									
Melange Pedastal	3989300	522000	118	40	N	350	29		striae
			310	30	E				traces into melange
			140	39	N				
			120	30	N				
			113	28	N	315	9		striae
Yin Yang	3989200	522000	105	21	N	305	12		
			113	24	N				fold-hinge
			80	22	N	310	10	N	striae
			90	38	N	150	34		striae
Collier Canyon	3989200	521600	345	15	W				Collier
			296	30	E				
			73	24	NW	317	20		striae
West Mormon Point	398900	521600	150	42	W	285	28		
			165	45	W				
			162	22	W				
			165	18	W				
			175	30	W				
			175	21	W				
			340	24	W				
			10	20	E				
			250	28	W				
			80	20	W				
Mormon Wash	3988700	523000	135	9	N				
			135	40	N				
			135	24	N				
			135	18	N				
			115	24	N	335	20		striae
			119	22	N				
			70	30	W				
			305	29	E				folded detachment
Willow Wash	3989600	524800	15	35	W				back of fan by FW clast
Size 36	3981550	526000	155	25	W				rake = 120
			155	15	W				
			150	15	W				striae
			155	22	W				
			0	35	W				
			340	22	W				
			310	20	SW				
			10	20	W				
			176	20	N				

Table 1.6. Continued

Location	UTM	UTM	Strike	Dip	Direction	Trend	Plunge	Direction	Comment
Badwater									
Elf	4014000	521000	100	38	N	55	30	N	striae
			180	38	W	276	36	W	striae
			180	34	W	270	32	W	striae
			0	35	W				
			340	35	W				
			0	34	W				striae
			0	35	W	270	35		
1 S. of Elf			315	30	S				
Wide	4012500	520600	214	25	W	18	16		striae
			218	25	W				
			215	25	W	3	18		striae
			215	25	W				
			215	25	W				
Green	4012500	520600	177	31	W	275	31		striae
			176	30	W	265	30		striae
Nose			340	30	W				
Nat Br	4015300	521000	0	25	W				
3 S of Nat BR	4015000	521000	350	40	W				

Table 1.7. Faults in the Pliocene section of Mormon Point

Strike	Dip	Dip Dir.	Location (X)	Location (Y)	Location (Z)	Distance on transect	Throw (order of magnitude)	kinematics
290	50	N	-4718	2691	239	5418	10	Above Willow Springs Fault
353	65	E	-4797	2710	237	5456	1	no markers, but good fabric
			-4797	2777	231	5558	1	"lake bed fault"
140	75	S	-4797	2777	231	5558	1	
330	70	N	-4797	2777	231	5558	1	SS-groove plunging 20E
15	85	S	-4838	2777	231	5558	1	weak normal sense indicators
35	45	S	-4838	2792	232	5602	1	dominantly normal sense
35	40	S	-4838	2792	232	5602	1	
40	30	S	-4838	2792	232	5602	1	low angle cuts high angle
40	60	S	-4838	2792	232	5602	1	
65	55	S	-4838	2792	232	5602	10	off marker beds
215	60	W	-4849	2792	232	5602	1	small displacements (<10c)
40	70	S	-4828	2821	232	5625	1	
20	60	S	-4908	2853	231	5623	1	
35	90		-4908	2876	226	5704	1	
115	60	S	-4908	2876	226	5704	1	deformation-band-like
180	15	W	-4908	2876	226	5704	1	
120	60	S	-4908	2876	226	5704	1	
220	70	W	-4908	2876	226	5704	1	
40	80	S	-4964	2876	226	5704	1	
320	40	E	-4997	3001	218	5815	1	extension of Lake-bed fault
120	60	W	-4922	3047	213	5869	1	graben
215	80	N	-4884	3093	208	5830	1	
225	65	W	-4884	3243	201	5879	1	
30	35	E	-4932	3243	201	5879	1	
215	85	W	-5022	3276	197	5938	1	
0	60	E	-5022	3335	188	6046	10	
320	75	E	-4965	3482	177	6082	1	3 sets like this one,
0	15	E	-4965	3482	177	6082	1	high angle offset low angle by 1/2m
160	60	W	-5089	3482	177	6082	1	
50	90		-5126	3578	164	6250	1	defm band-like
0	10	E	-4965	3595	162	6280	1	
120	65	W	-5199	3482	177	6082	1	
60	75	E	-4965	3646	155	6369	1	defm-band-like
170	55	W	-4965	3482	177	6082	1	
170	79	W	-4965	3482	177	6082	1	
230	30	W	-5089	3482	177	6082	1	
50	90		-5241	3569	165	6235	1	
340	30	E	-5247	3701	155	6439	1	

Table 1.7. Continued

Strike	Dip	Dip Dir.	Location (X)	Location (Y)	Location (Z)	Distance on transect	Throw (order of magnitude)	kinematics
165	55	W	-5312	3701	155	6439	1	cuts shallower one
55	90		-5290	3807	148	6536	1	gouge but no indicators
30	55	E	-5301	3807	148	6536	1	
255	75	W	-5290	3830	145	6576	1	def-band-like, no offset
80	30	S	-5290	3807	148	6536	1	
350	70	E	-5331	3807	148	6536	1	
10	20	E	-5305	3898	140	6602	1	
210	65	W	-5319	3898	140	6602	1	cuts the shallower one
165	50	W	-5319	3908	138	6620	1	
340	40	E	-5369	3908	138	6620	1	
20	15	E	-5395	3955	135	6689	1	high angle soles into low angle
20	70	E	-5395	3924	136	6690	1	
220	60	W	-5399	3924	136	6690	1	
165	85	W	-5395	3927	136	6696	1	
210	55	W	-5401	3924	136	6690	1	defm.-band-like (sketch)
160	70	W	-5405	3924	136	6690	1	throughgoing fault
60	90		-5407	4008	132	6735	1	
140	50	W	-5397	4022	130	6759	10	
175	90		-5559	4163	97	6926	1	
170	55	W	-5508	4201	92	6990	1	low angle cuts high angle
0	90		-5618	4163	97	6926	1	
170	70	W	-5508	4245	86	7064	1	
20	40	E	-5559	4163	97	6926	1	defm.-band-like
180	10	W	-5508	4201	92	6990	1	
15	90		-5618	4163	97	6926	1	larger displacement faults
30	65	E	-5508	4245	86	7064	1	
10	75	E	-5559	4163	97	6926	1	
180	30	W	-5508	4201	92	6990	1	
50	15	E	-5618	4163	97	6926	1	
225	75	W	-5508	4245	86	7064	1	
240	75	W	-5559	4163	97	6926	1	
45	50	E	-5508	4201	92	6990	1	cumulative 3m displacement
330	40	E	-5618	4163	97	6926	1	
45	90		-5508	4245	86	7064	1	
0	60	E	-5735	4163	97	6926	1	no striae
220	80	W	-5774	4282	74	7211	1	
40	80	E	-5791	4282	74	7211	1	possibly syn-depositional
15	75	E	-5791	4294	72	7233	1	
45	90		-5791	4294	72	7233	1	pink-against-green
205	80	W	-5791	4294	72	7233	1	conglomerate

Table 1.7. Continued

Strike	Dip	Dip Dir.	Location (X)	Location (Y)	Location (Z)	Distance on transect	Throw (order of magnitude)	kinematics
355	75	E	-5763	4294	72	7233	100	
30	90		-5763	4382	72	7263	1	pink against green
350	50	E	-5763	4382	72	7263	1	normal sense indicators, grey
0	50	E	-5763	4382	72	7263	1	against pink
340	50	E	-5763	4382	72	7263	1	
10	90		-5763	4382	72	7263	1	high angle soles into low angle
			-5787	4386	71	7269	1	pink/green
			-5822	4400	69	7293	1	pink/grey
220	78	W	-5841	4428	66	7338	1	grey/brown
35	40	E	-5858	4442	64	7362	1	w/clay smear
350	60	E	-5739	4455	62	7382	1	
0	90		-5739	4364	74	7233	1	cuts low angle fault
10	50	E	-5739	4364	74	7233	1	grey/red
55	90		-5903	4364	74	7233	1	12 faults
80	65	S	-5973	4511	52	7508	1	
240	60	W	-5973	4511	52	7508	1	higher angle soles into lower
235	80	N	-5988	4511	52	7508	1	angle with fabric
35	40	E	-5917	4523	51	7528	1	
110	50	S	-6116	4614	42	7528	1	criss-crossing fractures
0	70	E	-6151	4769	22	7781	1	
			-6151	4796	19	7825	1	1/2m of a graben-drop
60	60	E	-6151	4796	19	7825	1	
60	45	E	-6151	4796	19	7825	1	
55	55	E	-6151	4796	19	7825	10	
35	75	E	-6151	4796	19	7825	10	
35	65	E	-6151	4796	19	7825	1	
20	65	E	-6151	4796	19	7825	1	
30	45	E	-6151	4796	19	7825	1	
50	20	E	-6151	4796	19	7825	1	slot
165	55	W	-6151	4796	19	7825	1	
200	65	W	-6151	4796	19	7825	1	
350	75	E	-6151	4796	19	7825	1	
15	75	E	-6151	4796	19	7825	10	
15	65	E	-6151	4796	19	7825	10	
205	70	W	-6151	4796	19	7825	1	
15	70	E	-6151	4796	19	7825	1	
25	80	E	-6151	4796	19	7825	10	
16	75	E	-6151	4796	19	7825	1	
20	70	E	-6151	4796	19	7825	1	

Table 1.7. Continued

Strike	Dip	Dip Dir.	Location (X)	Location (Y)	Location (Z)	Distance on transect	Throw (order of magnitude)	kinematics
250	50	N	-6151	4796	19	7825	1	
40	90		-6151	4796	19	7825	10	
330	45	N	-6151	4796	19	7825	1	
60	80	E	-6151	4796	19	7825	1	
30	60	E	-6222	4796	19	7825	1	
40	90		-6222	5065	0	8049	1	
40	65	E	-6222	5065	0	8049	1	
230	69	W	-6222	5065	0	8049	1	
40	55	E	-6222	5065	0	8049	1	normal sense
30	55	E	-6222	5065	0	8049	1	soles into
35	50	E	-6221.696	5065	0	8049	1	detachment

Table 1.8. Faults in the Copper Canyon formation

Strike	Dip	Direction
301	50	W
183	62	W
174	54	W
236	67	W
340	15	W
55	80	W
30	79	E
204	73	W
230	60	SE
193	57	E
200	69	E
200	71	E
198	59	W
348	60	W

Chapter 2: Comparing magnetic and clast fabric in gouge and breccia from the Black Mountain detachments, Death Valley, CA: Implications for the micro-mechanics and kinematics of shallow crustal shear zones.

2.1. Introduction

Faulting in the top few kilometers of the crust occurs on sharp millimeter-scale dislocations and across broad meter-scale shear zones. The broad shear zones are filled with breccia and gouge, fault rocks with clast-in-matrix textures with gouge containing respectively larger amounts of clay-sized grains (Sibson, 1977). A noteworthy property of both gouge and breccia is the presence of fabric that is defined by the preferred orientation of grains. The fabric exhibits a systematic angular relationship between minor slip planes and the boundaries of the shear zone (Logan et al., 1979; Rutter et al., 1986). Fabric elements are important for the interpretation of the amount and direction of displacement across faults (Chester and Logan, 1987; Cowan and Brandon, 1994). The grain-scale kinematics that lead to fabric development also affect the rheology of shallow crustal shear zones because slip is partitioned between discrete planar structures and distributed deformation (Tikoff and Teyssier, 1994; Miller, 1996; Cowan et al., 2003). Any strain not accrued by distributed deformation across the shear zone is presumably accommodated by stick-slip behavior. Dynamically, the distributed deformation in gouges and breccias can favor both stable and unstable sliding that may scale to the seismic behavior of natural fault zones (Marone, 1990; Beeler et al., 1996; Scholz, 1998).

Furthermore, the constitutive minerals of gouges and breccias may mechanically control the static strength of faults (Wu, 1978; Morrow et al., 2000).

Despite the importance of fabric in shallow crustal rocks, it is more difficult to characterize and measure these inherently discontinuous fabrics than it is to characterize fabrics in deeper crustal rocks such as mylonites and phyllonites. The interpretation of the amounts of strain and grain-scale kinematics of the flow field within shallow crustal shear zones requires a methodology that addresses both the whole-rock fabric and the orientation of the constitutive particles. In an effort to understand the development of fabric in shallow crustal shear zones, we present measurements and interpretations of the shape preferred orientation (SPO) and the anisotropy of magnetic susceptibility (AMS) from gouge and breccia sampled from detachment faults exposed in Death Valley, CA. These faults are responsible for Pliocene-Quaternary extension and are coupled with subsidiary faults that define earthquake-scarps (Chapter 1; Hayman et al., 2003). The detachments contain centimeter-to-meter wide sections of gouge and breccia that have mesoscopic foliation (Miller, 1996; Cowan et al., 2003) and well-defined SPO (Cladouhos, 1999a). We also present the results of transmission and back-scattered electron microscopy, optical petrography, low temperature magnetic experiments, partial anhysterestic remanent magnetization (pARM), and anisotropy of pARM (ApARM). Collectively, these data indicate that the dominant magnetic carriers are *not* the >50 μm clasts that define the SPO. Therefore, we propose that the AMS measures the fabric of the finer-grained matrix in which the SPO-defining clasts are entrained.

Our results are adequately described by existing kinematic models that are based upon the early theories of fluid mechanics (Jeffery, 1922). The models treat clasts that define SPO as passive markers in a plastically or viscously yielding matrix (Ghosh and Ramberg, 1976; Ježek and Hrouda, 2002). However, the assumption that the medium in the Death Valley fault rocks yields to the rotation of passive markers may not be valid because the particles in the matrix attained a similar fabric to the clasts after the shear zone accrued enough shear strain. The mechanical implications of this are discussed after presentation of the data and the application of a simple kinematic model.

2.2 Methods

For the purposes of establishing a reference frame for sampling, we assume that the detachment shear zone is everywhere present and planar, and we use its dip direction as an index for the sample orientation. The samples were oriented in the field following the right hand rule with indices X_1 parallel to the strike of the shear plane, X_2 parallel to the dip of the shear plane, and X_3 normal to the shear plane. All thin sections were prepared by first embedding the samples in LR-White epoxy, fixed for over 24 hours at 60°C under vacuum. The samples were polished dry with 600 Grit polishing wheels. Once polished chips were prepared, no special methods were required to cut and polish the sections.

We measured SPO optically, primarily with ~25x magnification. Thin sections were traversed with a mechanical counting stage, and the length of the longest and shortest axes of each clast was recorded. Attempts to automate the process of determining

SPO with image processing were unsuccessful because of the low axial ratio of the clasts and the uneven contrast between clasts, matrix, and brittle microstructures. Cladouhos (1999a) presented a more systematic analysis of SPO, also summarized here, in the X_2-X_3 plane, using 31.25x, 125x, and 312.5x magnification on the optical microscope, and 48x and 200x scanning electron images (in back-scattered electron, BSE, mode) obtained on the University of Washington JEOL 733 Superprobe. Additional scanning electron microscopy was conducted at the University of Washington and on a JEOL 8600 at the Johns Hopkins University. Transmission electron microscopy (TEM), and high-resolution TEM (HR-TEM) were conducted at the Johns Hopkins University on a Philips CM300FEG 300-kV, field-emission gun electron microscope.

All measurements of the magnetic properties of the fault rocks were made at the Pacific NW Paleomagnetism Lab, Western Washington University. The fault-rock samples were cut into cubes 1.5-1.8 cm on a side and the MS was measured using a KLY3-S Kappabridge. We related the structural reference frame of the sampling localities to the geographic reference frame of the instrument by aligning X_1, X_2, and X_3 to N, W, and the vertical axis, respectively. We measured the MS of 200-300 mg sub-samples of the fault rocks from 77K to room temperature using a CS-3L cryostat. Partial anhysterestic remanent magnetization (pARM) was given to selected samples with a D-Tech D-2000 alternating field (a.f.) demagnetizer with a 0.5 mT DC field produced by a built in bias coil, and measured with a 2-G model 755 Superconducting Rock Magnetometer. Each of the four samples was first a.f. demagnetized with a 200 mT peak field. Measurements of pARM were taken using a specific window of 10 mT, between 5

to 195 mT. The specific window of measurement of the anisotropy of pARM was unique

to groups of specific samples and defined by the half-height width of the dominant peak

in the pARM spectrum. An 18-orientation measurement scheme, based on the rotatable

design matrix of Jelinek (1978) was used, with a.f.-demagnetization performed between

each step. X-ray fluorescence (XRF) analysis of major element composition of bulk-rock

powders and X-ray diffraction (XRD) analyses of clay separates were provided by P.

Vrolijk of ExxonMobil Upstream Research (1997, personal commun; Vrolijk et al.,

1997). Additional XRD patterns were attained at the University of Washington. Trends

and plunges of vectors were plotted on lower hemisphere stereonets, and Rose diagrams

of SPO data were plotted, using the program Stereoplot by R. Allmendinger. The

kinematic model was attained using the Matlab scripts of Jeˇzek and Hrouda (2002).

2.3 Black Mountains, Death Valley, CA

The Black Mountains bound the east side of Death Valley, CA, and are flanked by

low angle normal (detachment) faults that define the upper surface of domal, "turtleback"

landforms of Proterozoic metasedimentary rocks and Miocene plutons (Fig. 2.1)

(Drewes, 1963; Wright and Troxel, 1984; Holm et al., 1994). Recognition of several

Pliocene and Quaternary tephra in the overlying sediments and the amounts of throw

across subsidiary faults constrain the minimum age and amount of slip on the

detachments (Holm et al., 1994; Chapter 1; Hayman et al., 2003). The currently exposed

brittle detachments accrued approximately 1 km of slip in the Quaternary, including at

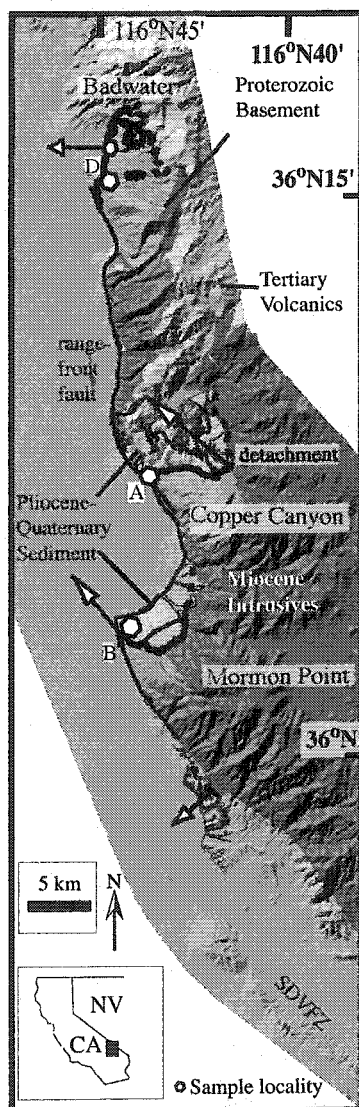Figure 2.1. Compiled 30m USGS DEM, with shaded map units. Traces of detachments (bold lines) are from Drewes (1963), Miller (1996), and Wright and Troxel (1984). Arrows are the trend of measured striae on the fault planes. Samples discussed in this study were acquired from localities A, B, and D. SDFZ is the Southern Death Valley Fault Zone whose trace is unclear north of a faulted, ca. 0.1 Ma cinder cone on the valley floor.

least a 14% stretch across the upper plate of the detachment. Given the exposed footwall and an estimated 0.5-1 mm/yr slip rate, there has been at least 3.5-4 km of slip and associated upper plate extension since the early Pliocene. These are minimum estimates and the detachments may have accrued many tens of kilometers of slip in Late Miocene time (Snow and Wernicke, 2000). Geodetic measurements of 2-4 mm/yr to the NW describe the relative motion of geodetic stations between the Black Mountains and Panamint Mountains to the west (Miller et al., 2001).

There are few focal mechanisms with a low angle normal sense of slip in the seismological record (Jackson and White, 1989), although coseismic deformation on low angle normal faults is recorded in some earthquake sequences (Axen, 1999). The modern detachments are above the seismogenic zone, and likely have been since the early Pliocene. There are, however, earthquake scarps on the valley floor that are defined by high angle faults that are coupled with the detachments (Chapter 1; Hayman et al., 2003). The rupture that created the scarps must have propagated up the detachments from hypocentral depths. Since coseismic displacement on a fault plane will decrease with distance from the hypocenter, and given the structural relationships exposed at the exposures of the detachments, we propose that the detachments have also slipped aseismically. By analogy with rock mechanics experiments the gouge and breccia may stabilize slip within faults under certain conditions (Beeler et al., 1996; Marone and Scholz, 1990), but also play an undocumented role in coseismic processes at the up-dip limit of significant faults.

The geometric relationship between the hanging-wall faults and the detachment is consistent with a geodynamic model for extension across a wedge of Coulomb material with a critical taper (Xiao et al., 1991; Chapter 1; Hayman et al., 2003). The Coulomb wedge analysis when applied to the hanging wall suggests that the static friction required for slip on the detachment is ~0.4. Typical materials have coefficients of friction between 0.6 and 0.85. It is probable that the effective friction of the gouge and breccia is lower than that of typical earth materials, either because of the elevation of fluid pressure or a deviation from simple Coulomb behavior.

In addition to the implications for fault mechanics, the Black Mountain detachments are important structures for understanding the neotectonics of the basin and range. In most places, the sense of motion across subsidiary faults, striae on slip surfaces, and kinematic indicators within the fault rock constrain the sense of slip on the detachment to be northwest-side-down, dip-slip (Chapter 1; Hayman et al., 2003; Cowan et al., 2003). Reports on this sense of motion differ and the key localities exhibit evidence for oblique components of slip on the detachment (Keener et al., 1993). In theory, the Black Mountain fault system participates in transtension associated with the Eastern California Shear Zone (Miller, 2001). The sense of motion across the Death Valley detachments is therefore something of an open but important problem. Locally, west-dipping fault surfaces should accrue some oblique slip in the larger NW-directed transtension even if the typical sense of motion is dip-slip.

2.4. Fault rocks

The most general term for rocks from faults and shear zones is *fault rock* (Sibson, 1977) although we use this term exclusive of mylonites and phyllonites that form at temperatures that promote crystal-plastic deformation and greenschist-facies metamorphism (circa 300°C). Below metamorphic temperatures, fracture is favored over creep mechanisms and the resulting rocks are referred to as cataclasites. The term cataclasite connotes *cataclastic flow*, a specific deformation mechanism wherein fracture accompanies the rolling and sliding of grains past one another (Engelder, 1974). While breccias are cataclasites, gouges do not exhibit transgranular fracture in thin sections (Fig. 2.2). However, determining the deformation mechanism that led to the clast-in-matrix textures observed in the gouge is not straightforward. Numerical experiments that describe granular flow — *granular flow* is used here to describe deformation where particles interact inelastically during rotation and translation (e.g. Wolf, 1998) — produce structures and fabric similar to those observed in nature (Morgan, 1999; Morgan and Boettcher, 1999). Alternative models for gouge deformation emphasize incremental comminution of the host rock by repeated and localized earthquake rupture (e.g. Chester and Chester, 1998), the rotation of particles within a viscous or plastic matrix — *plastic* is used in the sense of a Bingham material wherein after reaching its yield strength, the medium has no further linear stress-strain relationship, although there are alternative rheologic models to describe plastic-like or viscous-like failure —, or dispersive flow of particles with dynamics that might resemble a gas or fluid phase (Otsuki, 2003).
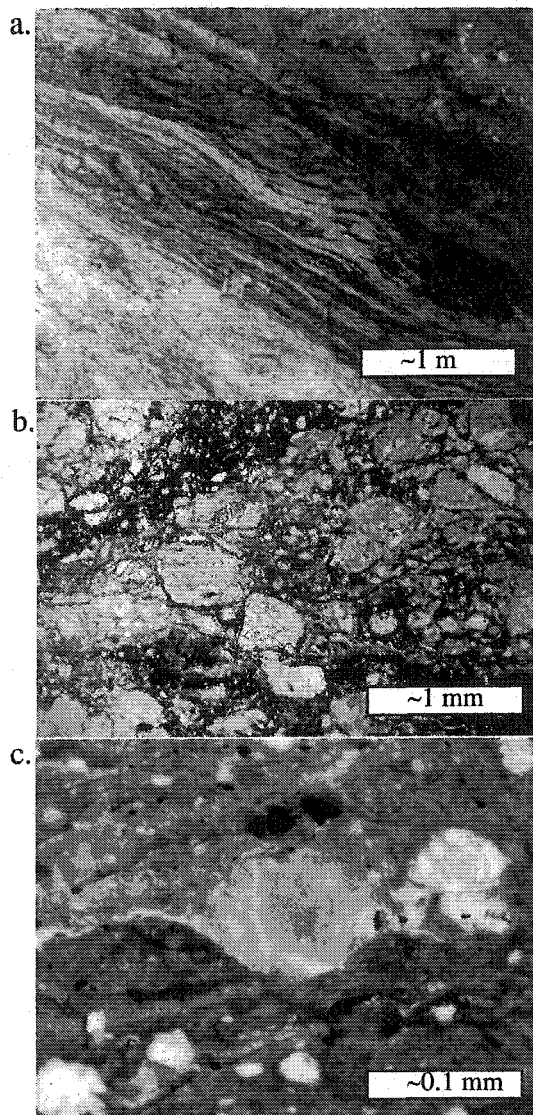
Figure 2.2. Texture of gouge and breccia a) Exposure of a detachment on the Badwater turtleback. Foliated breccias form the base of the exposure at the bottom left. Granular gouge with folded (by cataclastc flow) layers of dolomitic gneiss are in the center of the shear zone. Above this granular gouge unit are clay gouges, directly beneath the hanging wall at the top right. (b) Photomicrograph (in plane light) of a foliated breccia from Mormon Point. Note the trans-granular fractures and grain-on-grain contacts with interstitial clay-sized minerals and weak fabric. (c) Clay gouge from Copper Canyon turtleback. Note that any trans-granular fractures are relicts, there are few grain-on-grain contacts, and the abundant, foliated, clay-sized matrix. Careful inspection of the photomicrograph reveals both the larger opaque phases adjacent to the grain boundaries of the larger clasts, but also fine opaques within the matrix.

Fault rocks are subdivided based upon grain size and texture (Sibson, 1977; Cladouhos, 1999a; Cowan et al., 2003). *Breccia* has >20-30% visible, angular lithic clasts, *foliated breccia* is a breccia with a mesoscopic foliation, *granular gouge* has <20-30% visible, rounded clasts, *clay gouge* is defined primarily by the abundance of platy aggregates of clays and clay-sized minerals, and *scaly clay gouge* is a clay gouge wherein the clay-sized material is arranged in distinctive, anastomosing folia. At certain localities in the Black Mountains, the differentfault rocks are stratified across the detachment (Fig. 2.3) and a <1 mm-thick striated slip surface separates the foliated fault rocks from the hanging wall (Cowan et al., 2003).

The climate and topography of Death Valley produces excellent exposures of fault rocks along kilometers of strike-length. We have spent several years studying these exposures and have chosen representative samples for intensive study. The samples were collected from the Copper Canyon (A-series), Mormon Point (B-series), and Badwater (D-series) Turtlebacks. The fault rocksamples include foliated breccia (A3, B34, D3), granular gouge (A6, A13, B2, D2), clay gouge (A1, B1, D4, D11), highly comminuted material from a location adjacent to a striated slip surface (D14), and scaly clay gouge (A11) (Table 2.1).

The samples were oriented in the field with non-genetic indices X_1 parallel to the strike of the shear plane, X_2 parallel to the dip of the shear plane, and X_3 normal to the shear plane (Fig. 2.3). Slip surfaces and folia that have a systematic orientation are provided indices to help in their analysis. R refers to synthetic (down-dip facing) riedel structures, P refers to structures inclined to the shear plane, and Y refers to structures
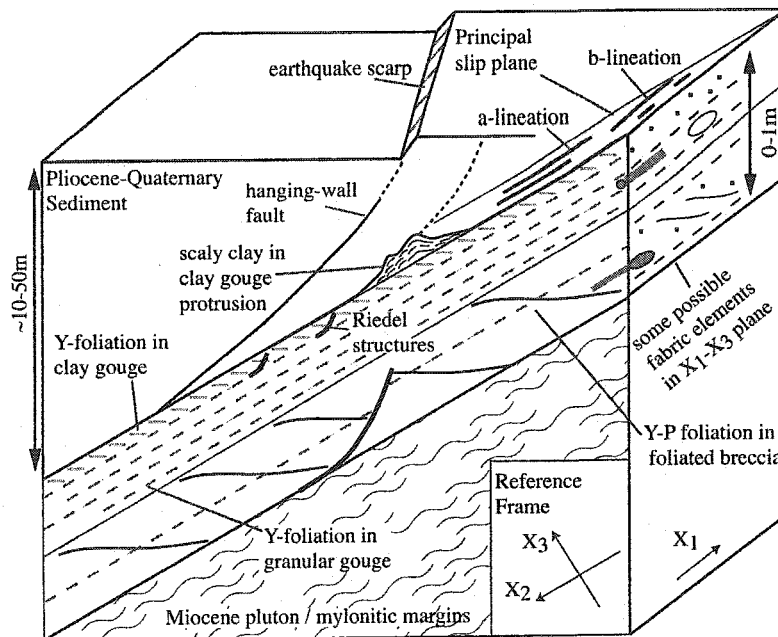
Figure 2.3. Schematic of the detachment system. The reference frame is a right-hand rule, orthogonal reference frame with X1 parallel to strike, X2 parallel to dip, and X3 normal to the fault plane; none of these axes are meant to indicate strain or stress directions. Other key elements of the detachment system depicted include: an earthquake-produced scarp cutting Pliocene-Quaternary sediment, hanging-wall faults that sole into the detachment, in places associated with clay gouge protrusions into the hanging wall, the stratification of fault rocks across the detachment below a sharp, striated slip plane, orientation of a and b lineation, riedel, P, and Y structures, and some possible structures in X1-X3 views.

parallel to the shear plane. This terminology shares similarities with the S-C terminology for mylonitic rocks (Berthé et al., 1979) although its usage is tailored specifically for shear bands in rock experiments investigating the brittle field (Tchalenko, 1968; Logan et al., 1979). These structural indices consistently describe fabric elements in natural shear zones (Chester and Logan, 1987).

2.5. Shape preferred orientation

SPO is a statistical measure of the orientation of the long axes of prolate or oblate grains (Rutter et al., 1986; Chester and Logan, 1987). There are several limitations in using SPO to study gouges and breccias. In practice, SPO is a labor-intensive measurement of thin-section scale >50 μm clasts that are entrained in a finer grained matrix. Because of heterogeneity at higher magnification, partly imposed by the narrower field of view, SPO does not efficiently measure the fabric in the finer, micron- and sub-micron scale matrix (Cladouhos, 1999a). Interpretations of SPO are inherently non-unique – the inclination of the SPO relative to the shear zone boundary is either interpreted as being directly proportional to the shear strain (March, 1932; Chester and Logan, 1987), or else as defining a line of net zero rotation within a flow field (Cladouhos, 1999b). One aspect of the non-uniqueness of interpreting SPO is the requirement of many models that the finer-grained matrix allows the larger grains to behave as passive markers for the flow field (Jeffery, 1922; Ghosh and Ramberg, 1976).

Cladouhos (1999a) presented SPO data from thin sections cut parallel to the plane defined by the X_2-X_3 axes (Table 2.1). We repeated these measurements on a select group

of samples and also measured SPO on thin sections cut parallel to the X_1-X_3 and X_1-X_2 planes (Table 2.2). We measured SPO optically, primarily with ~25x magnification. Thin sections were traversed with a mechanical counting stage, and the length of the longest and shortest axes of each clast was recorded; r is the axial ratio of the longest vs. the shortest axis (Table 2.1, 2.2). Grains with r<1.4 were not used to measure SPO. We made cursory identification of the mineralogy of each clast, primarily to identify the abundance of opaque, possibly ferrimagnetic grains.

We calculated the semicircular mean vector ($\bar{v}$):

$$\bar{v} = \frac{1}{2} \times \tan^{-1}\left(\frac{\sum \sin 2\theta_i}{\sum \cos 2\theta_i}\right) \qquad \text{(Agterberg, 1974)} \qquad (1)$$

and the vector strength ($|a|$):

$$|a| = \frac{1}{N}\left\{\left(\sum \sin 2\theta_i\right)^2 + \left(\sum \cos 2\theta_i\right)^2\right\}^{\frac{1}{2}} \qquad \text{(Agterberg, 1974)} \qquad (2)$$

for the population (N)measurements of orientation (θ_i) (Table 2.1, 2.2). The analysis of Cladouhos (1999a) revealed that $\bar{v}$ remains roughly constant at all magnifications, although $|a|$ is lower for SPO determined from higher magnifications.

The X_2-X_3 plane is cut parallel to the dip direction and normal to strike. Our measurements in X_2-X_3 define a shear zone-parallel, Y-oriented SPO or, alternatively, a shallow-plunging P-oriented SPO in all of the samples (Fig. 2.4). In some samples, such as the Badwater clay gouge, D11, the dispersion of data is best explained as a composite Y-P fabric. Granular gouges (D2, B1) have the best-defined Y-fabric, whereas clay gouges (A11, D11, D4) have the best-defined P or P-Y composite fabrics. The foliated
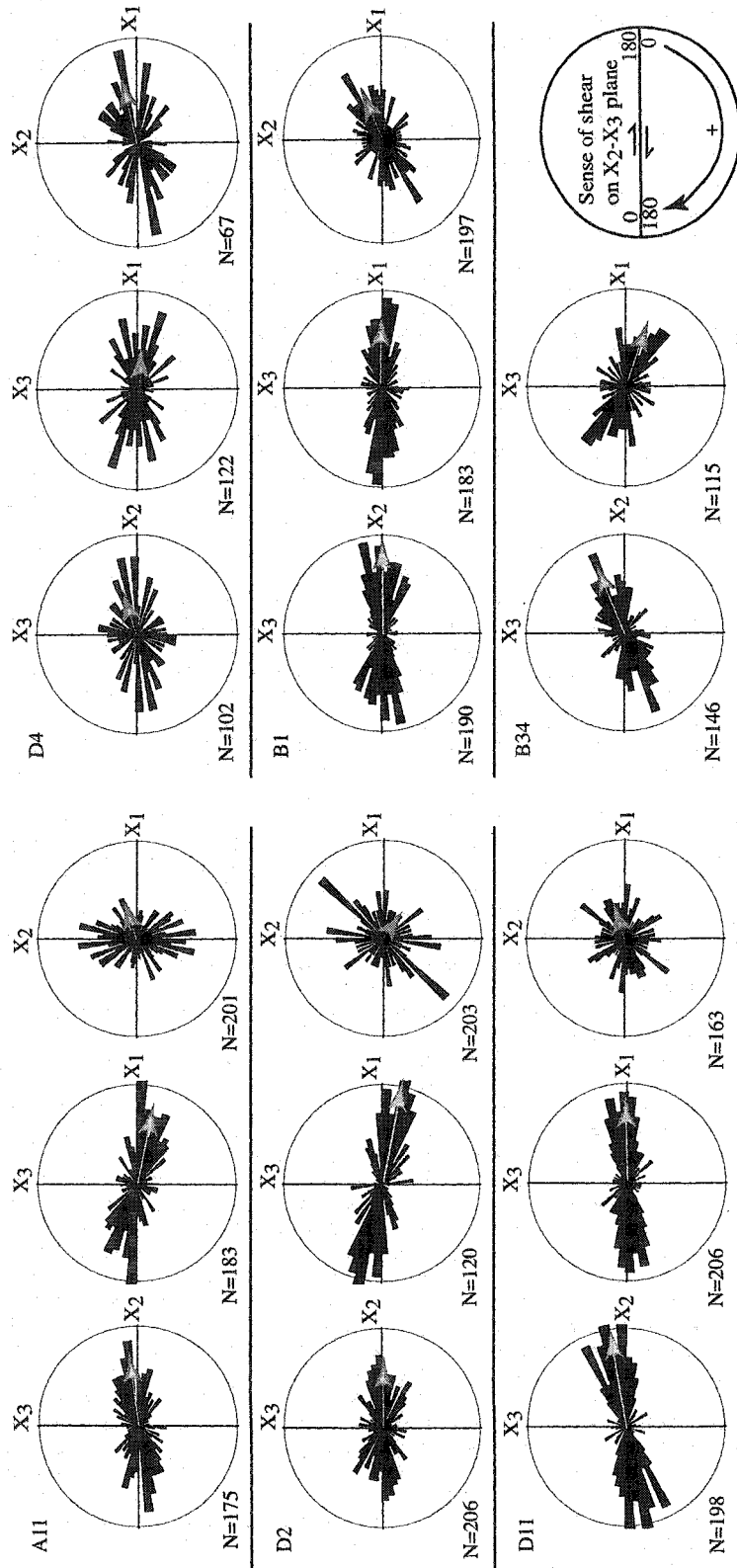
Figure 2.4. Rose diagrams of the shape preferred orientation measured on different planes of samples. Circles are 5% of the data. Vectors (in gray) are normalized such that the maximum vector strength is one unit-length, and others are the appropriate percentage length. Note that +X2 is on the right for X2-X3 planes, such that the sense of shear would be right-lateral if X2 is parallel to the slip direction. Measurements of angles are clockwise from the horizontal. These conventions were used to facilitate comparison of our results with those of Cladouhos (1999a).

breccia (B34) has the strongest P-fabric. These results are similar to those of Cladouhos (1999a) (Table 2.1), with the possible exception of the sample of Mormon Point granular gouge, B1. Cladouhos (1999a) found that B1 had an SPO with a synthetic riedel orientation, shallowly plunging in the $+X_2$ direction. In our analysis of sample B1 there is only a weak sub-fabric in this riedel orientation (Fig. 2.4). Despite the presence of localized slip planes in synthetic riedel orientations (Cladouhos, 1999a&b; Cowan et al., 2003), none of the samples exhibits a strong riedel-oriented SPO. In summary, the SPO measured in the X_2-X_3 planes of the samples considered here (Fig. 2.4) are well defined and parallel-to-slightly inclined to the shear plane. This is a configuration consistent with significant finite shear strain producing fabric elements consistent with those proposed by Logan et al. (1979) and others.

The X_1-X_3 plane is cut parallel to the strike direction. This plane of exposure has not been studied in as much detail as the X_2-X_3 plane because efforts to date have treated the detachments as an overall plane-strain environment (Cladouhos, 1999a&b; Cowan et al., 2003). At specific localities there are field and microstructural indicators in this plane-of-view to support treating the deformation within the detachments as plane strain within X_2-X_3 (Cladouhos, 1999a; Cowan et al., 2003). The assumption that deformation was plane strain is also necessary to proceed with certain structural analyses. However, there are field exposures of the X_1-X_3, strike-parallel plane that are rich with inclined fabric, fold axes, and slip planes that plunge and dip both along and into exposures. The SPO measured on the X_1-X_3 planes of the samples supports the notion that there is a component of out-of-plane strain; plane strain in X_2-X_3 would produce either Y-oriented

fabrics in X_1-X_3 (if the grains define an oblate SPO fabric in X_1-X_3) or would not produce a fabric at all (if the grains define a prolate SPO fabric in X_2-X_3 but not in X_1-X_3) (Fig. 2.3). Most of the samples, and particularly samples A11, D2, D4, and B34, have SPO that plunge shallowly-to-moderately towards $+X_1$ (Fig. 2.4). Only clay gouges B1 and D11 have roughly Y-oriented SPO in the X_1-X_3 plane such that no plane strain is evident.

Inclined fabrics in the X_1-X_3 plane could signify northward-directed motion of the hanging wall on the fault, producing fabrics with a riedel orientation. Alternatively, the inclined fabric in X_1-X_3 could be the consequence of intersecting Y-P foliations that anastomose within the X_2-X_3 plane and produce local plunges of the intersection lineation. Either interpretation may have applicability at specific localities. For example, some localities such as B1 that is near the hinge of a fold in the detachment, do preserve striae that pitch several degrees to the north.

The X_1-X_2 plane providesthe view facing directly down onto the shear plane. Any SPO in this view requires a preferred direction of stretch within the shear zone, or a prolate SPO normal to the slip direction, akin to the lineation-direction in a and b respectively (Fig. 2.3) (Sander, 1930). The X_1-X_2 view in sample B34 did not include enough grains with r>1.4 with which to measure SPO. Several of the samples have no SPO in X_1-X_2; D11 and D2 each have a<0.17, which is a minimum value for a significant SPO vector (Cladouhos, 1999a). Samples A11, D2, D11, and B1, each have weakly-to-strongly defined SPO in X_1-X_2. A11 has an apparent SPO in the X_2 direction (although $|a|$=1.7, and $\bar{v}$=163, towards X_1), D2 and B1 have a SPO roughly bisecting X_1 and X_2, and D4 has a SPO just oblique to X_1. The variability in the direction of the SPO

in X_1-X_2 is best interpreted as indicating variability within the flow field of the shear zone

or as tracking a pitch in tectonic transport.

To summarize the SPO results for all of the samples, the X_2-X_3 plane contains a Y

and/or Y-P oriented SPO, but no R fabric, the X_1-X_3 plane has either Y- or inclined,

probably R-oriented SPO, and X_1-X_2 has either no SPO, or an SPO towards the

northwest. There are two major obstacles to further developing a mature interpretation of

the SPO without additional information: (1) The SPO in the three planes of view cannot

be treated as principal directions or eigenvectors of the flow field, *a priori*. (2) The SPO

is not a strain marker in the strict sense. Rather, SPO is the preferred orientation of many

hundreds of discrete particles, and therefore does not correspond to stretched or

constricted grains. In fact, with the exception of sample A11, the average axial ratio of

grains varies by less than 10% between all three views and there is no systematic

relationship between vector, vector strength, axial ratio, fault rock lithology, and

sampling location (Table 2.2). Therefore, the application of lineation-based terminology

or descriptions of plane and non-plane strain only have bearing on the state of strain in

the detachments when accompanied by a developed kinematic model. We shall explore

this aspect of the SPO data in the Discussion, following further treatment of the data.

2.6. Anisotropy of magnetic susceptibility

Magnetic susceptibility (MS) is a third-rank tensor, k_{ij}, that relates the natural

magnetization, M_i, to an applied magnetic field, H_j:

$$M_i = k_{ij} \bullet H_j \tag{3}$$

The principal directions (eigenvectors) of the k_{ij} have values k_1, k_2, and k_3; in practice the principal vectors are normalized to a unit-length. For SI volume-normalized magnetic units, MS is dimensionless. The mean susceptibility k_{mean} is defined by:

$$k_{mean} = \frac{k_1 + k_2 + k_3}{3} \tag{4}$$

In samples that have $k_1 > k_3$, the MS has an anisotropy quantified by relations (Hrouda, 1982):

$$\text{(a)} \quad P = \frac{k_1}{k_3}; \quad \text{(b)} \quad L = \frac{k_1}{k_2}; \quad \text{(c)} \quad F = \frac{k_2}{k_3} \tag{5a-c}$$

and:

$$T = 2 \times \left[\frac{\left| \log\left(\frac{k_2}{k_3}\right) \right|}{\log\left(\frac{k1}{k3}\right)} \right] - 1 \tag{6}$$

The AMS ellipsoid corresponds closely to that of the finite strain ellipsoid in many instances (Borradaile, 1991) and provides a valuable tool for developing kinematic models of fabric development (Tarling and Hrouda, 1993; Jeˇzek and Hrouda, 2002). Although a bulk-rock property, the AMS ellipsoid effectively defines an SPO for magnetite, or a lattice preferred orientation (LPO) for most other minerals (Nye, 1985; Richter, 1991). While AMS is considered a more approximate indicator of fabric orientation and intensity than SPO, it is relatively labor-free, and can provide information on a larger spectrum of grain-sizes with one measurement.

One of the few generalities that can be made about the population of AMS data from the fault rock samples is that k_1 is shallowly plunging and k_3 is steeply plunging in

almost all samples (Fig. 2.5a, b, Table 2.3). Aside from the generality of an AMS

ellipsoids with long axes shallowly inclined to the Y-plane of the shear zones, the

orientations of the AMS ellipsoids do not systematically vary with respect to the

coordinate system. Some samples (e.g. D2) have k_1 parallel to X_2, some samples (e.g.

A13) have k_1 plunging parallel to X_1 and roughly normal to X_2, but most have k_1 oblique

to X_1 and X_2.

Interpreting the AMS data involves surmounting some of the same obstacles

confronting the interpretation of SPO data, but with two important exceptions. Unlike

SPO data, the AMS data is, by definition, the orientation and relative magnitude of

principal vectors that describe the MS. Therefore, much like strain, the AMS data of the

samples can be separated into prolate ellipsoids with $T<0$ (Table 2.3) and plot above the

$L/F=1$ line on a Flinn-type plot (D4, A6, and A13 on Fig. 2.5c) and oblate ellipsoids

with $T>0$ and plot below the $L/F=1$ line. The one outlier in the data is sample A11, the

only scaly clay gouge in the sample population. Sample A11 has an oblate AMS

ellipsoid, but an anomalously high anisotropy with $P=1.1296$. All of the other samples

have $P<1.1$. If the AMS can be equated to the SPO, an assumption we shall explore in a

following section, a preliminary interpretation of the AMS data would be as follows: (i)

Samples A6, A13, and D4 contain populations of prolate particles that have long-axes

preferentially aligned sub-parallel to X_1, normal to the dip and tectonic slip direction on

the detachments. (ii) Samples A11, A1, B1, B2, D11, D2, and D14 have populations of

oblate particles that anastomose about the Y-foliation with a preferential dip widely

dispersed around the X_2, slip direction. (iii) The remaining samples A3, D3, and B34 are
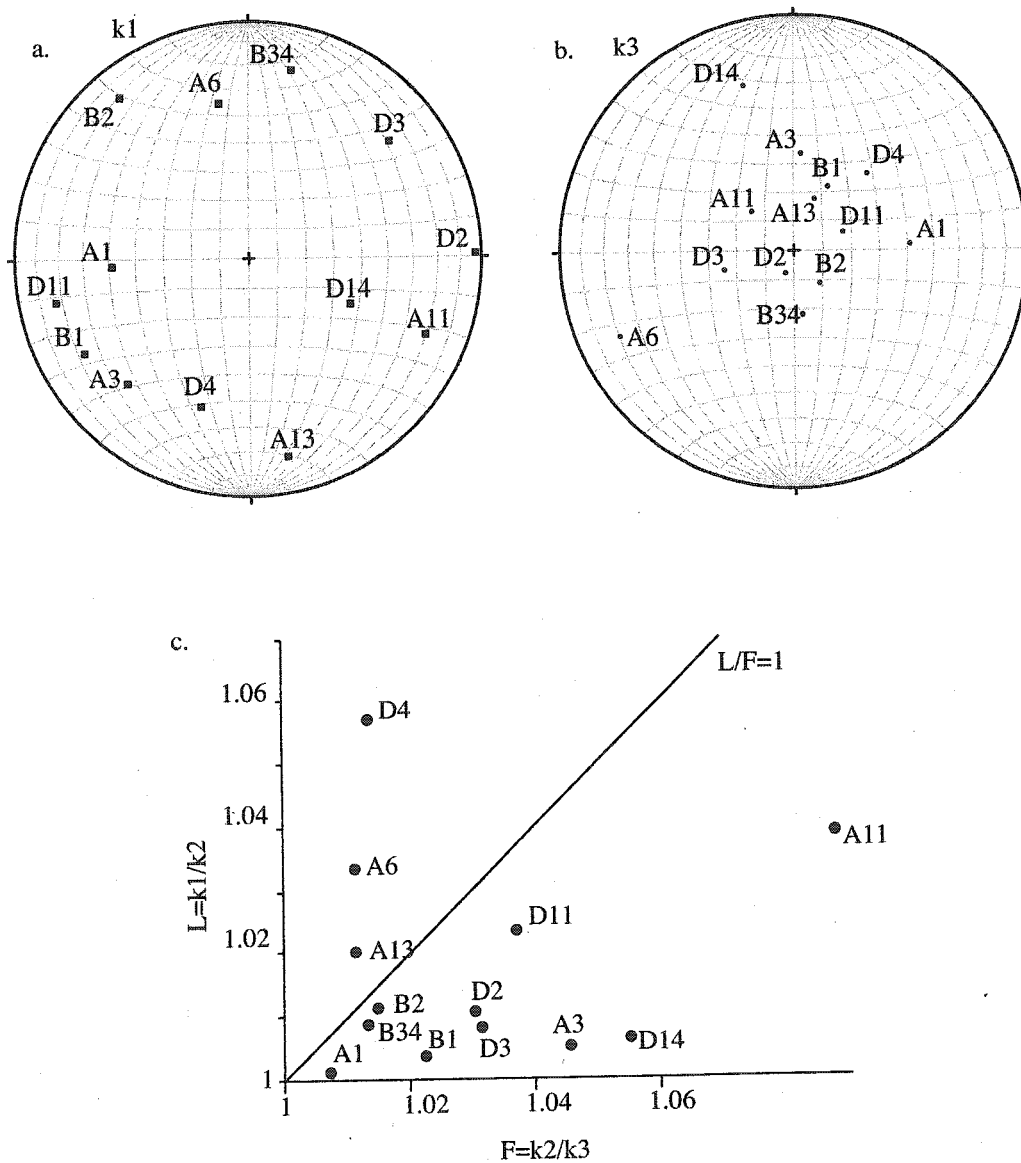
Figure 2.5. AMS data a. k1 in stereoprojection for all samples, b. k3 in stereoprojection for all samples, c. Flinn-type diagram of measures of anisotropy of magnetic susceptibility, L and F. Note that L/F=1 is, in theory, roughly equivalent to the K=1 line of a Flinn diagram of a strain marker. Data that plots below this line represent oblate ellipsoids, and data that plots above this line represent prolate ellipsoids. For Flinn diagrams of strain markers, volume change during strain has the effect of moving this line to the right (loss) or left (gain).

foliated breccias that have characteristic P-Y foliation. Relevant to the orientation of the

AMS ellipsoid in this latter group of samples, and samples in the first group, is that the

long axis of the AMS ellipsoid can be sensitive to the intersection of two foliations

(Housen, et al., 1993). Developing a more robust interpretation for the AMS data requires

additional information about the magnetic carriers and a working kinematic model.

2.7. Comparison of SPO and AMS

The systematic orientation of SPO and AMS relative to the shear plane indicates

that each type of data provides relevant information about the fabric of gouge and

breccia. One would expect differences between the orientation of the SPO and AMS

vectors for several reasons. Firstly, the SPO does not necessarily measure eigenvectors of

the flow field except in cases when the rotation of grains is restricted to one plane, such

as the X_2-X_3 dip-parallel section. Secondly, the AMS is dependent on the mineralogical

carriers of susceptibility and their distribution, shape, and orientation-distribution.

Therefore, the vectors of AMS and SPO should only be parallel in the case where AMS is

produced by the same grains that define the SPO, or the case when all of the particles in

the rock respond to fabric forming processes in the same way. An interesting outcome of

this study is that there are systematic relationships between the SPO and AMS

orientation.

Several of the samples have AMS and SPO vectors that lie in similar orientations.

If we define an angle, A, as the angle between k_1 and the SPO in the X_2-X_3 plane, sample

D2 has A=4° (Fig. 2.6). Samples with a bit more divergence between k_1 and the SPO in
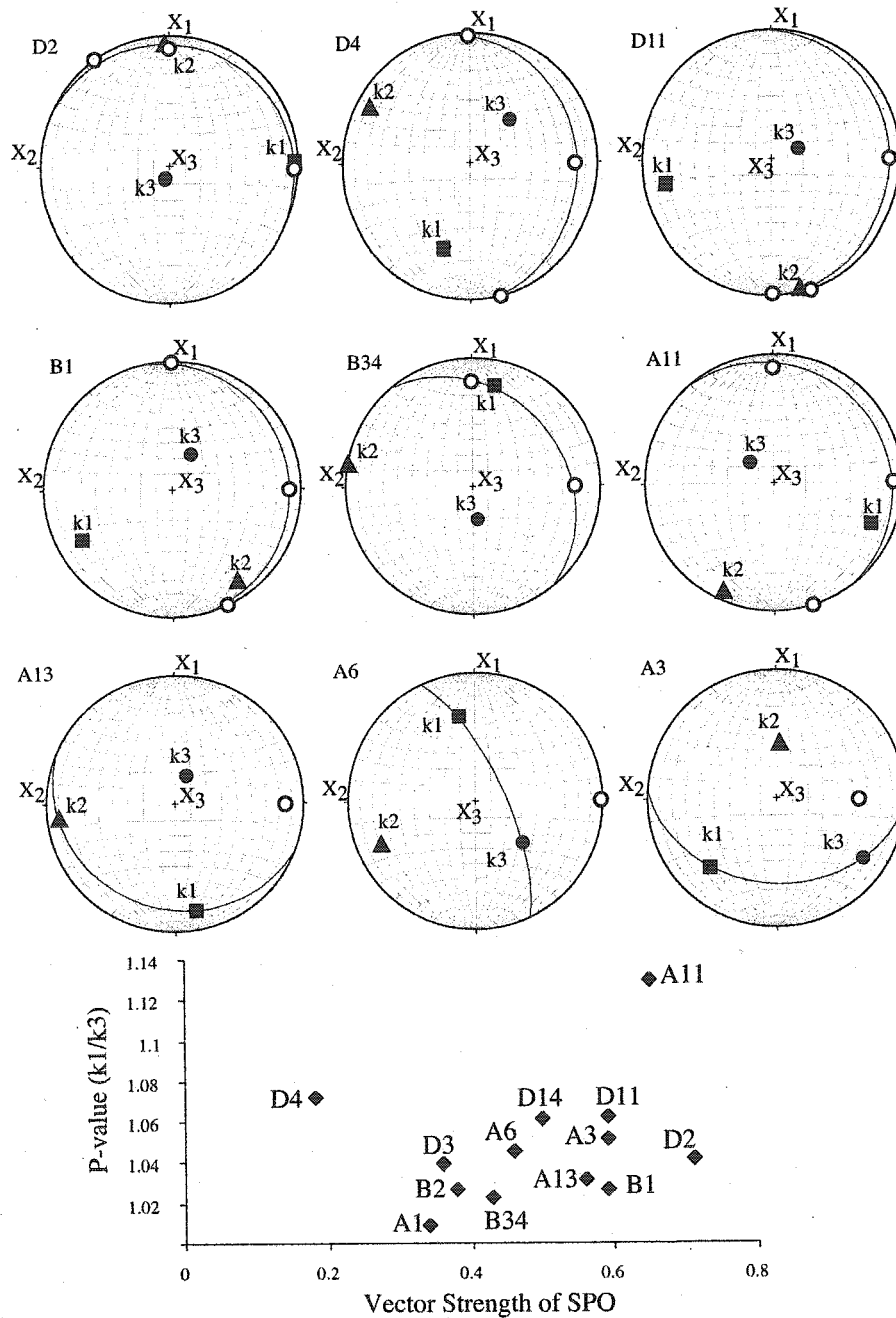
Figure 2.6a. Stereoplots of AMS and SPO data for samples discussed in the text. Circles are the average SPO in the X1-X2, X2-X3, X1-X3 planes; samples B34, A6, and A3 do not have SPO data for all three planes. Boxes are the maximum principal axes, triangles are the intermediate principal axes, and circles are the minimum principal axes of the AMS. 6b. Vector strength of the SPO plotted against a measure of the AMS (P). Although weak, there appears to be a positive correlation between SPO vector strength and P, demonstrating that each are measuring the anisotropy of the fabric.

the X_2-X_3 plane are samples D11 from the Badwater turtleback (A=29°), sample B1 from the Mormon Point turtleback (A=36°) and sample A11 from the Copper Canyon turtleback (A=25°), respectively. All four of these samples have AMS ellipsoids that are oblate (T>0) with a range in anisotropy between them from P=1.0262 to P=1.1296. The range of 32° in the dispersion of angular relationships of SPO and AMS between samples is in the long axes of oblate shapes about a shallowly plunging vector. The dispersion does not affect k_3, that is at a high angle to the shear plane for all samples. The 32° variation may be a natural bi-product of fabric elements that fluctuate ±16° about the idealized strong preferred orientation (AMS and SPO).

There are three samples with the maximum principal direction of the AMS ellipsoid oriented at a high angle and roughly normal to the SPO vector in the X_2-X_3 plane. Samples D4 and B34 have A=85°, and A=71°, respectively. Sample A13, for which we only have SPO measured in the X_2-X_3 plane, has A=75°. Sample D4 has a prolate AMS ellipsoid (T<0). Samples A13 and B34 have prolate and oblate AMS ellipsoids respectively, but in each case, L very nearly equals F (Fig. 2.5c). Equally important, sample B34 has two mesoscopic foliations, P and Y, and therefore the orientation of k_1 of the AMS ellipsoid is parallel to an intersection lineation.

Also related to the arrangement of particles in the rocks is an important effect displayed by samples A6 and A3. These samples likely display an *inverse* AMS fabric. The vectors k_1 and k_3 in sample A6 is inverted from that in sample A3 (Fig. 2.6). Inverse fabrics in granular materials are thought to arise from the orientation and/or distribution

of certain types of mineral particles (e.g., tourmaline, single-domain magnetite) (Rochette et al., 1999).

It is clear that the AMS and SPO are each measures of the orientation of particles in the gouge and breccia. It is also clear that there is some relationship between strain, AMS, and SPO. There is a weak, positive correlation between the vector strength of the SPO and the P-value of the AMS ellipsoid (Fig. 2.6b). As described above the AMS ellipsoid is present in samples with both prolate and oblate aspect ratios (Fig. 2.5c) and the prolate ellipsoids tend to be oriented at a high angle to X_2 — the direction of tectonic transport. Knowledge of amount of shear strain, or overall behavior of the material during its textural evolution, remains elusive despite the established relationship between the state of strain, the arrangement of particles, and the net AMS and SPO measure of the fabric of the gouges and breccias. Fault rocks such as these have a complicated strain history that possibly involves volume loss and multiple generations of minerals. In order to increase our understanding of the detachments, we must consider what the carriers of magnetization are, what we can glean about the history of the shear zone, and how to implement a kinematic model of the textural development.

2.8. Source of AMS

The most difficult aspect of interpreting the significance of AMS is that the magnetic carriers within the mineralogy of a rock are not initially known. In addition, determining what produces the *anisotropy* of the magnetic susceptibility poses an increased challenge. For single grains of paramagnetic phyllosilicates and clay minerals,

the AMS is produced by a crystallographic preferred orientation (CPO) (Nye, 1985). Assuming that phyllosilicates and clay minerals attain a shape preferred orientation via parallelism of [001] planes (e.g. Oertel, 1985), then AMS is a measurement of SPO of phyllosilicates and clay minerals. For single grains of magnetite, AMS is due to shape and not crystallographic orientation, and therefore a population of magnetite grains will produce an AMS that is directly proportional to the SPO of magnetite (Richter, 1991). Magnetite-produced and phyllosilicate-produced AMS may not fundamentally differ in orientation considering the capacity of magnetite grains to adhere to, and mix with foliation-defining phyllosilicates and clays (Kodama and Sun, 1990). Less useful for measuring fabric than the fore-mentioned sources is distribution anisotropy (Hargraves et al., 1991). Distribution anisotropy occurs in samples that have magnetic grains that are concentrated in domains thereby creating a bulk-rock AMS that represents a sub-volume of the sample. An additional source of AMS that may be unique to fault or clastic rocks is an *inherited* AMS wherein the clasts that we used to measure SPO contain an AMS arising from the mineral fabric within the clasts that could overwhelm the AMS within the matrix of the rock. In the following few paragraphs, we present data from a variety of methods in an effort to determine the magnetic carriers in the fault rocks.

2.8.1. Low-temperature susceptibility experiments

There are several low-temperature transitions in the magnetic susceptibility that are indicative of the magnetic carriers within a sample. Characteristic low-T transitions include the Verwey transition at 120K for magnetite, and the Morin transition at $-15°C$ for hematite (Dunlop and Ozdemir, 1997). Paramagnetic minerals, such as clay minerals,

follow the Curie-Weiss law wherein MS varies as a function of 1/T (Fig. 2.7). Therefore,

if the low-T data from the fault rock samples fit a 1/T curve well, the dominant carrier of

MS are probably clay minerals that are volumetrically significant in the fault rock

samples. A lack of such 1/T variation of MS with temperature would indicate that the MS

is carried by either ferrimagnetic (magnetite) and/or diamagnetic (calcite, quartz) phases.

All of the samples have a positive MS, ruling out the possibility that the carbonate and

quartz in the samples are the dominant MS carriers (Fig. 2.7). Many samples have a

noticeable increase in MS between 120 and 130K (Fig. 2.7a, b), consistent with the

Verwey transition. In some of these samples the only change in MS with T is the Verwey

transition, indicating that magnetite is the dominant carrier of MS. Other samples (Fig.

2.7c) have MS that is best fit by a 1/T variation, indicating that paramagnetic minerals are

the dominant carriers of MS. A few samples have difficult to interpret low-T MS data

wherein no Verwey transition is evident, but the change in MS with T does not fit a 1/T

variation (Fig. 2.7d-f). It is possible that either oxidized minerals such as maghemite, or

ultra-fine superparamagnetic minerals may be present in such samples.

We found no clear relationship between the carrier of MS and fault rock unit.

Samples of foliated breccia had either ferrimagnetic, or paramagnetic MS. Samples from

clay and granular gouges all have ferrimagnetic MS, with some having pronounced

transitions indicative of magnetite, while others do not have a clear Verwey transition.

2.8.2. pARM

To further characterize the magnetic properties and magnetic fabrics in these

samples, partial anhysterestic remanent magnetization (pARM) and anisotropy of pARM
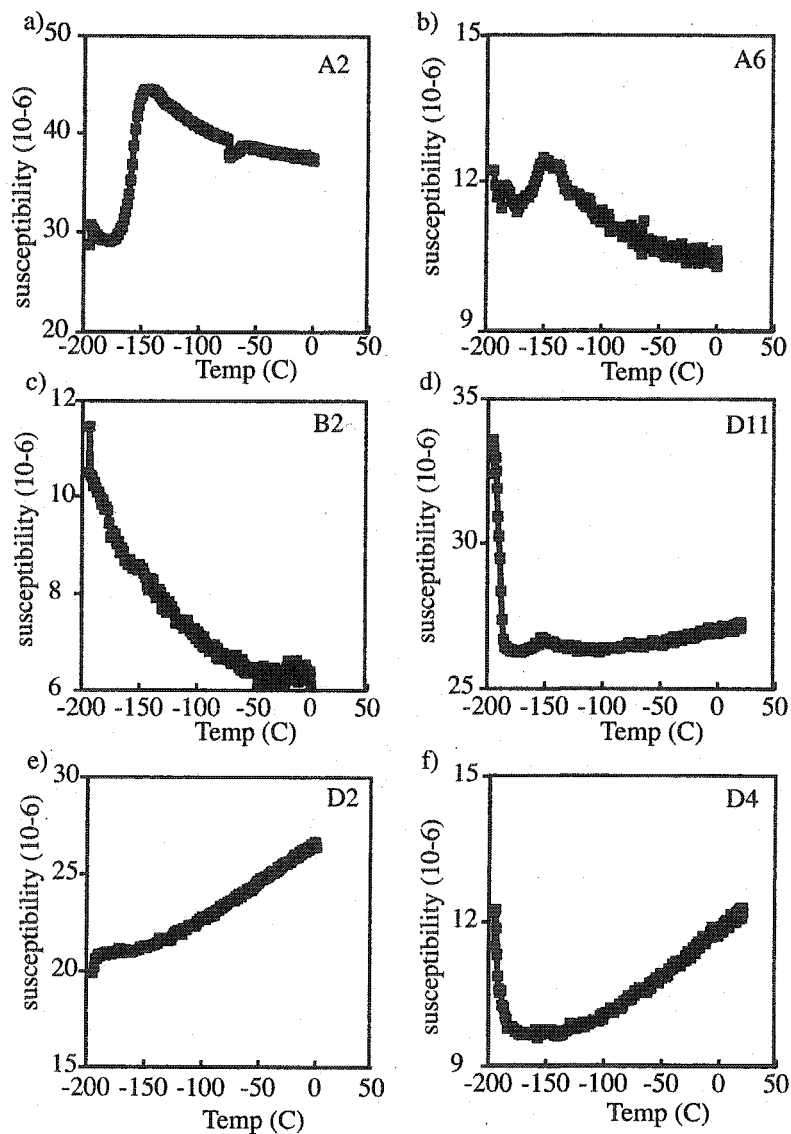
Figure 2.7. Representative results of the low-temperature experiments on the fault rocks. (a) a typical spectrum for the samples from Copper Canyon demonstrating a magnetite-controlled AMS. (b) A6 has a weak Verwey transition suggesting that the magnetite has an ultra-fine grain size, or that there is some alteration of the magnetite to maghemite. (c) A spectrum for sample B2 is best-explained by 1/T behavior due to paramagnetic minerals, such as clay minerals. (d,e,f) The Badwater clay gouges have a weak-to pronounced drop in MS between –200 C and –150 C, and a consistent increase in MS from –150 to 0 C suggesting that a mixture of paramagnetic clay minerals and oxidized or ultrafine (perhaps SP) magnetite is the carrier of the AMS.

experiments (e.g. Jackson, 1991) were performed on selected samples from each

lithology. The method is advantageous in that only magnetite fabrics are measured, and

grain-size sub-populations as identified by pARM can also be separately measured, both

of which minimizes the complications of fabric interpretation by isolating a single carrier

of magnetization.

The pARM results (Fig. 2.8) have pronounced peaks that occur between 10 and

50 mT, which are consistent with multi-domain (MD) to pseudo-single-domain (PSD)

magnetite (Jackson, 1991). Sample B2 (Fig. 2.8b) has notably higher coercivities, with a

break in the pARM intensity between 100 and 150 mT. Based on the pARM

measurements, the ApARM experiments for samples A1, B2, and D2 used a window

from 10 to 60 mT for the pARM, sample D4 used a window from 5 to 35 mT, and an

additional window between 100 and 160 mT was also selected for sample B2 to measure

the fabric of the high coercivity fraction. The ApARM experiments revealed that, with

one exception, the AMS and ApARM fabrics are essentially coaxial (Fig. 2.8e-h, Table

2.4). The exception is sample D4, which has a ApARM fabric that has its minimum

pARM axis rotated approximately 45° degrees clockwise from the AMS k_3 axis, and a

maximum (intermediate) pARM axis that is adjacent to the AMS k_2 (k_1) axis. This may

indicate that the AMS of sample D4 is a composite fabric, of either two "normal" AMS

sub-fabrics, or includes an "inverse" AMS sub-fabric.

2.8.3. Fault rock petrology

The comparison of SPO to AMS, the pARM results, and most models for the

kinematics of flow require the assumption that the fault rocks have two populations, the
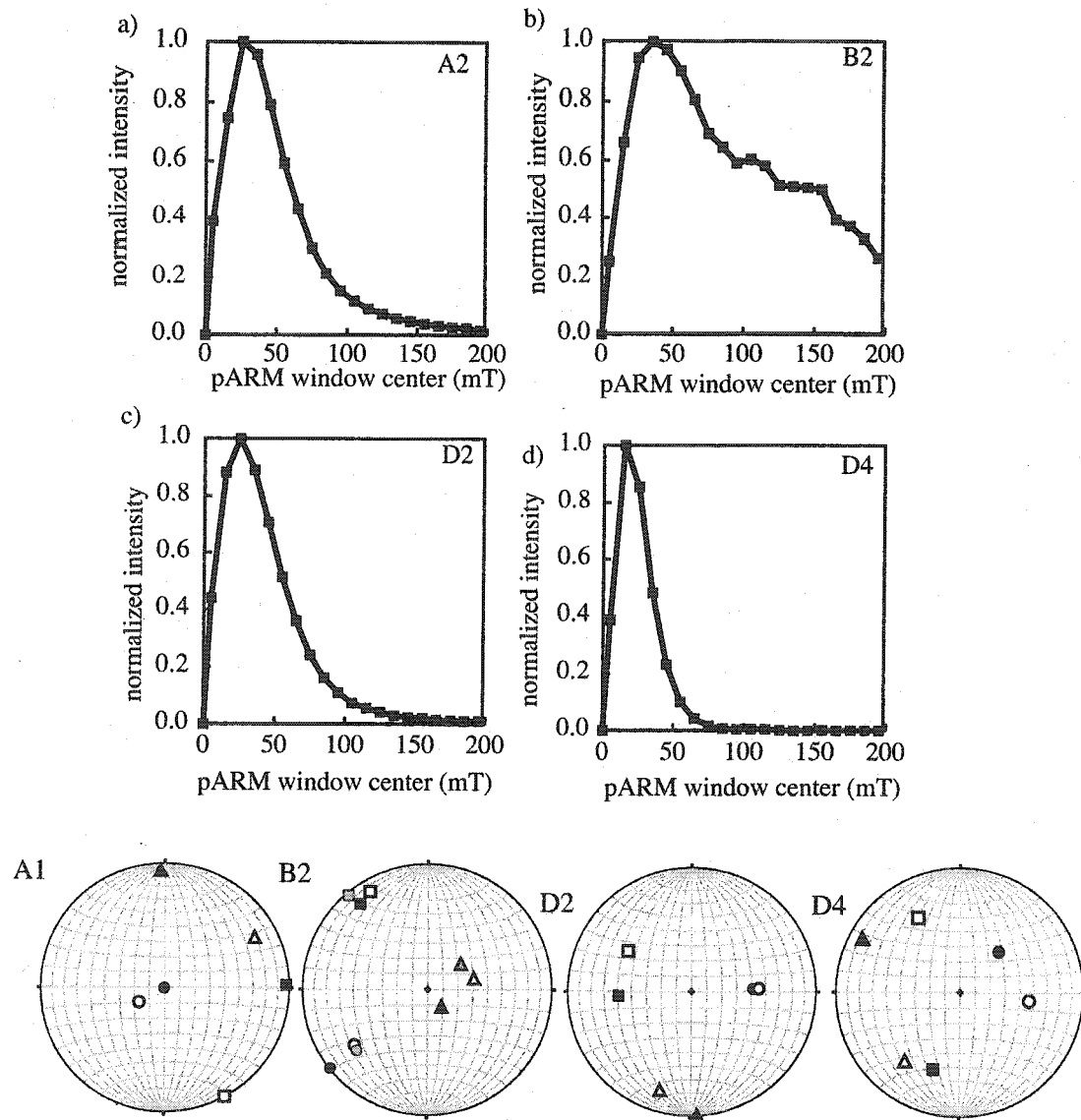
Figure 2.8. aARM/paRMRepresentative pARM curves from the fault rocks. For all curves, the center of the 10-mT wide pARM window is plotted versus normalized magnetization. The Copper canyon samples (a) have a single pARM peak at 25 mT, indicating MD and PSD sized magnetite, the Mormon Point granular gouge (b) has a bi-modal pARM curve, with peaks at 50 and 100-150 mT that indicate finer-grained magnetite, and both Badwater clay gouge (c,d) samples have single pARM peaks at 10 to 25 mT. (e-h) stereoplot of principal vectors of the pARM demonstrating near-coaxiality of the ApARM and AMS. The symbolic convention is the same as for Figure 6 with open symbols the axes for AMS and solid or gray symbols the axes for ApARM.

larger population with grain sizes roughly from 10's of microns to millimeters, and the finer grain sizes from nanometers to a few microns (Fig. 2.9). The larger clasts are dominantly of the same lithology as the footwall: quartzofeldspathic or micaceous schists and gneisses or less common dolomitic gneiss. In some sections there are as much as 10% clasts derived from the hanging wall including cemented sediment, angular fragments of non-mylonitic crystalline rocks, and rare volcanics. The larger clasts are deficient in mafic and opaque minerals: less than 5% of the observed clasts have opaque grains as major constituents.

The bulk-rock Fe_2O_3 wt% (the oxidation state is not differentiated) weakly correlates with K_{mean} (Fig. 2.10) such that all samples with $k_{mean}>10^{-3}$ have $Fe_2O_3 \geq 6$ wt%, and samples with $k_{mean} \leq 10^{-4}$ have $Fe_2O_3 \leq 6$ wt%. We note that K_{mean} only directly correlates to %Fe for samples with paramagnetic susceptibility (Tarling and Hrouda, 1993), and the relationship between K_{mean} and %Fe for samples with a magnetite-produced MS is a function of grain size variation as well as magnetite concentration. Nonetheless, samples with demonstrably ferrimagnetic MS belong to the high Fe_2O_3 group.

The matrix mineralogy is dominated by clay minerals. X-ray diffraction (XRD) patterns of <2μm separates are dominated by varieties of polytypes and a range of swelling components in illite and chlorite. Petrographic textures observed by BSE and transmission electron microscopy (TEM) reveal that the micrometer and sub-micrometer scale mineralogy is heterogeneous and includes dolomite, feldspar, and different oxides mixed with the clay minerals. However, the dominant fabric-defining minerals are illite,
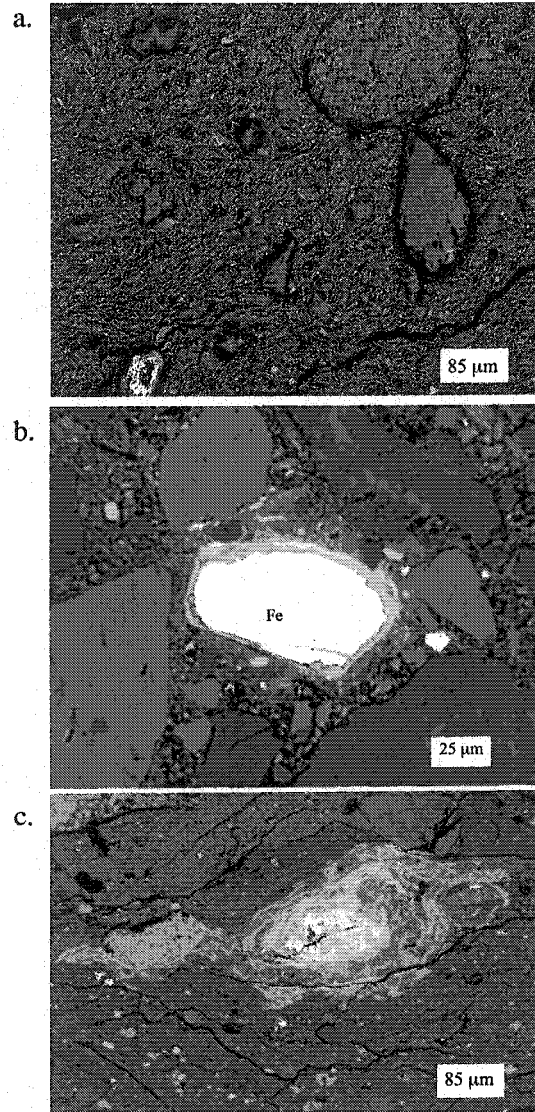
Figure 2.9. a. Back-scattered electron image (BSEI) of Badwater clay gouge D4. The large (ca 50 μm) clasts are either dolomite, quartz, or lithic fragments inherited from the footwall. We interpret the rounded clast on the top-center-right of the image to be a cemented and remobilized clast of the matrix material. The surrounding matrix is an aggregate of clay-sized minerals, the majority of which are phyllosilicates that demonstrably grew in situ. b. A prolate clast of an iron oxide. This is the larges size-fraction of possibly ferrimagnetic grains, and roughly the same size as the smallest size-fraction of the grains that define the SPO. Surrounding this grain is ultra-fine secondary Fe-phases that, along with the disseminated micron- and sub-micron-scale oxides, define the AMS in most samples. c. Manganese oxides disseminate around a parent clast. We interpret this texture to indicate precipitation of oxides and subsequent distributed deformation very late in the history of the detachment, an instructive example of the interplay between authigenesis and deformation.
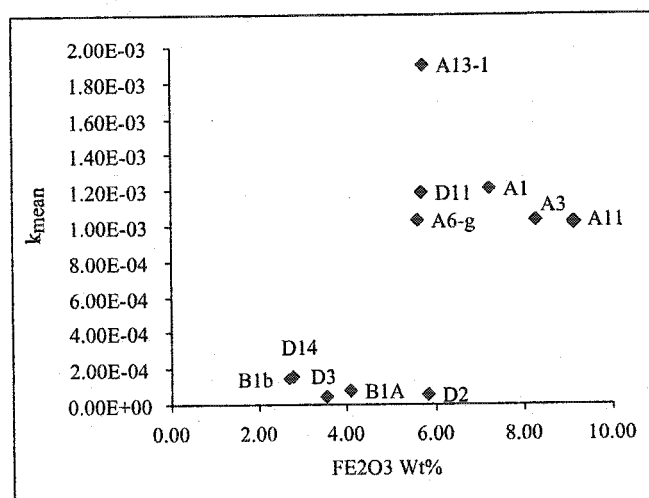
Figure 2.10. A comparison of bulk susceptibility vs. Fe2O3 wt % demonstrating that, in general, high samples with a high kmean (>10-3) have a high bulk rock Fe2O3 (inc. magnetite) (≥6 wt %).

illite/smectite, and chlorite (in B- and D-series samples) or a swelling turbostratic —

turbostratic refers to the rotation of crystallographic layers about a zone axis — polytypic

chlorite wherein (in A-series samples). We studied sample D4 in considerable detail by

TEM. Energy dispersive Xray spectroscopy (EDS) analyses of illite on dispersed grain

TEM mounts, revealed stoichiometrically disproportionate amounts of Fe. A second

TEM grid of this sample was prepared by ion milling a millimeter-diameter epoxy-

impregnated sample. Several of the observed grains of illite had inclusions of iron oxides

(Fig. 2.11a). Under high resolution TEM (HRTEM), the iron oxides were shown to be

nanocrystalline magnetite with grain sizes on the order of 30 nm (Fig. 2.11b). Selected

area electron diffraction patterns of the oxide clusters confirm the magnetite structure.

Diffraction patterns and EDS spectra are not presented here in the interest of brevity.

To summarize, the low-T MS experiments, measurement of ApARM,

compositional analyses, and electron microscopy observations collectively support the

hypothesis that the dominant magnetic carriers in the Death Valley fault rock are *not* the

large grains used to measure the SPO. Rather, the magnetic carriers are fine (micron-

scale), and ultra-fine (micron-to-nanometer-scale), grains found in the matrix. In some

samples, particularly the clay-rich gouges, the magnetic carriers are magnetite, whereas

in other samples, particularly the gouges and breccias from Mormon Point (B-series), the

magnetic carriers are the clay minerals.

a.   b.
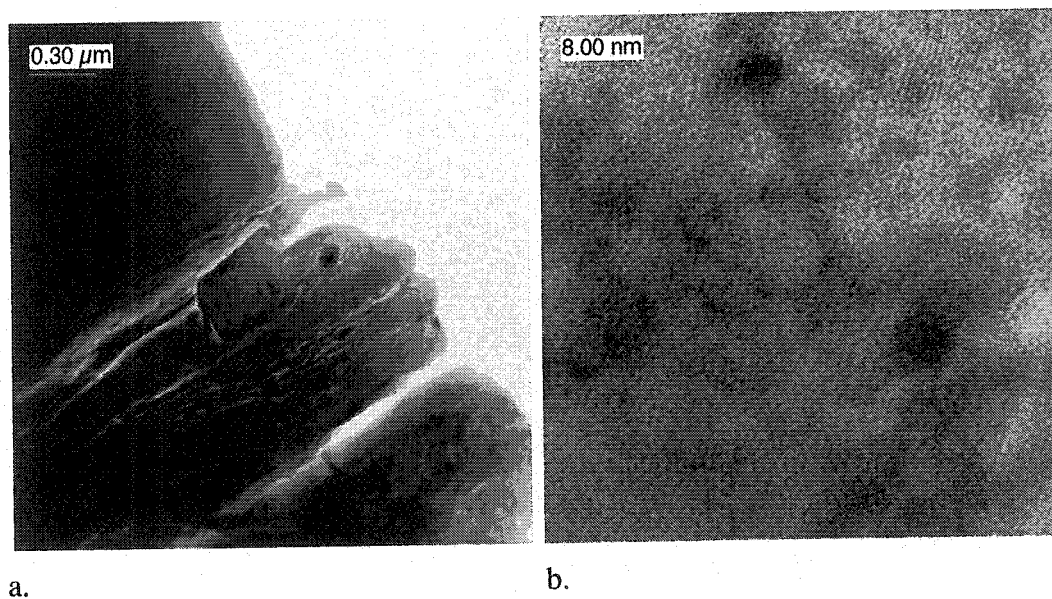
Figure 2.11. (a) TEM image of a grain within the fine-grained matrix of clay
gouge D11. The lath in the center of the image is interstratified illite/smectite
with a rhomb-shaped inclusion (late?) of dolomite. Adjacent to the dolomite is
a small inclusion of an Fe-bearing phase. (b) A high-resolution image of this
inclusion resolves a patch-work of 2.8Å lattice fringes, consistent with {110}
of sub-domainal magnetite.

2.9. Discussion

Studies of gouge and breccia have broad implications for understanding the mechanisms for the stability and strength of faults. In Death Valley, the gouges and breccias within the Black Mountain detachments partly control the structure of the basin near the range front, and play a role in the dynamic effects of seismicity, possibly promoting stable, aseismic, sliding. In this inductive context establishing magnetic and clast fabrics with kinematic significance within the fault rocks is an important finding. Relevant to the neotectonics of Death Valley, northwest geodetic motion (Miller et al., 2001) should impart oblique components of slip onto north-striking, west-dipping segments of the detachments. Similarly, hinge areas of the turtleback anticline should accrue slip parallel to the axes of the folds, but oblique to the local dip of the detachments. AMS and SPO fabrics in the X_1-X_2 plane in some samples may indicate a modest pitch to the north on some north-striking segments of the detachments and near the hinges of the turtleback anticlines.

We further explore the kinematic and mechanical significance of the AMS and SPO fabrics by comparing the natural fabrics observed in the Black Mountain detachments to fabrics produced by a kinematic model of foliation and lineation development over time. The deformation within the Black Mountain detachments has been previously approximated by simple shear (Cowan et al., 2003), and general shear at steady state and constant volume (Cladouhos, 1999b). However, prolate AMS fabrics and some SPO fabrics are characterized by lineations in b, parallel to the strike direction (X_1).

The orientations of linear fabric elements raise the possibility that a kinematic model involving a modest component of transpression (Sanderson and Marchini, 1984) appropriately describes the kinematic evolution of the AMS and SPO fabrics. Furthermore, the most thorough formulation of a kinematic model for AMS development also invokes transpression to explain the orientation of linear fabric elements (Jeˇzek and Hrouda, 2003). Rather than explore every assumption needed to properly apply a quantitative kinematic model— changes in width of the shear zone, the introduction or expulsion of material from the shear zone and partitioning of strain onto discrete slip planes are not considered in the solution — we present a model as a point of departure from which we can make some statements about the SPO and AMS, and inspire future analysis.

We have empirically demonstrated that the AMS in most samples from the Black Mountain detachments is produced by the SPO of magnetite, and CPO, roughly equivalent to SPO, of clay minerals in a few cases. Therefore, both data and theory (e.g. Richter, 1991) support the abstraction of the AMS and SPO as vectors within a flow field. Following Jeˇzek and Hrouda (2002), the motion of any line or plane in a flow field can be modeled kinematically without regard to forces or mechanisms. The vector that represents the line or plane in the flow field is operated on by a tensor, L_{ij}, with components of strain rate ($\dot{\varepsilon}$). Components with $i \neq j$ correspond to non-pure-shear such that $\dot{\varepsilon}_{12}$ is the component of simple shear, equivalent to the shear strain (γ) in X_2-X_3. These components can be related to the regional tectonics and wall-rock reference frame of the shear zone via:

$$\dot{\varepsilon}_{i=j} = \frac{\upsilon}{d}\sin\alpha; \dot{\varepsilon}_{i\neq j} = \frac{\upsilon}{d}\cos\alpha \qquad (7)$$

where α is the angle between the motion of the wall rock, υ is the rate of change of thickness of the shear zone, and d is the initial width of the shear zone. The L_{ij} tensor produces an instantaneous increment of small displacement that can be related to a small increment of time, t, via:

$$d(t+\Delta t) = I + L(t)\Delta t \qquad (8)$$

where I is the identity matrix, and d is the displacement. The displacement function operates on a vector (x):

$$x(t+\Delta t) = x(t)d(t+\Delta t) \qquad (9)$$

One of the underlying principles of this type of analysis is that the shape of the object that is rotating within the flow field affects its response to strain, and therefore its final orientation (Jeffery, 1922; Ghosh and Ramberg, 1976; Oertel, 1985). Ježek and Hrouda (2002) implement the sensitivity to shape by splitting the L_{ij} into the symmetric and anti-symmetric tensors E and Ω and a shape factor q where:

$$D(n\Delta t) = (I + (q\mathrm{E}+\Omega)\Delta t)^n; q = \frac{r^2-1}{r^2+1} \qquad (10)$$

for grains of axial ratio, r, and n increments of displacement. If q is positive then the shape is prolate and if q is negative then the shape is oblate. Finite strain, approximated by P for AMS (Borradaile, 1991), is determined by the stretch (DD'), and therefore the model allows us to monitor both the change in orientation and shape of the AMS (or SPO) ellipsoid.

We approximate the dimensions of deformation within the detachments as d=10m, and υ= 1 mm/yr (=1 km/My), and α=1° (nearly simple shear). A 10m wide shear zone provides for minimum estimates of the amount of shear strain because deformation becomes strongly localized within shear zones <1m wide. The solution of the kinematic analysis for these dimensions results in the foliation, such as defined by an oblate AMS or SPO, approaching a stable orientation at a low angle to the X_1-X_2 plane at relatively low shear strains of γ>50, after roughly 0.5 million years of strain accumulation. This result is consistent with the observation in the field of lenses of Quaternary-age sediment parallel to the foliation within the detachment shear zones (Cowan et al., 2003). Secondly, any prolate particle, or lineation, "flips" from X_2-parallel, to X_1-parallel or X_3-parallel orientations. This is a natural consequence of the inversion of the principal axes of the finite strain ellipsoid with large transpressive strain (Tikoff and Teyssier, 1994). The prolate fabrics that are parallel to X_1 (lineation in b) or X_3 (inverse fabrics) therefore require γ>250, or 2.5 Ma given Death Valley strain rates. Some of the fault rock is certainly older than 2.5Ma given early Pliocene sediment in the hanging wall of the detachments (Holm et al., 1994).

The kinematic model of Je˘zek and Hrouda (2002) adequately explains some of the essential properties of the SPO and AMS fabrics from the Black Mountain gouges and breccias. The model does not, on its own, explain why the AMS fabrics are more dispersed in orientation than the SPO measurements. The explanation that we favor for the difference between the SPO and AMS data is that the two are measurements of two different generations of particles. The grains that define the SPO are inherited from the
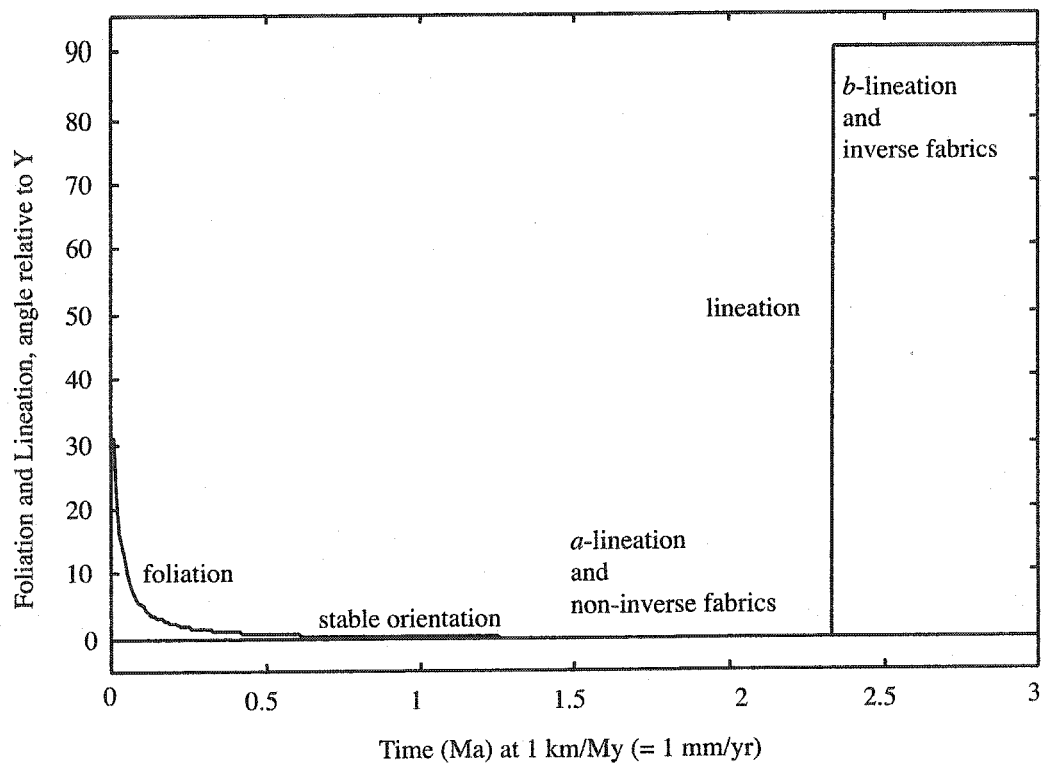
Figure 2.12. Changes in orientation with shear strain of foliation (solid) and lineation following Je˘zek and Hrouda (2002).

footwall of the shear zone, and are therefore roughly as old as the shear zone itself. The magnetic carriers on the other hand are primarily authigenic, and precipitated within the fault zone at some later stage in the history of the detachments. According to our hypothesis, the AMS measures less finite shear strain than the SPO. Although more general kinematic models or further exploration of the model of Je˘zek and Hrouda (2002) could result in alternative hypotheses, we contend that the general approach we present here adequately describes many of the features that we observe in the gouges and breccias from the Black Mountains.

Kinematic models do not address forces or the relationship between stress and strain during the deformation of the material. However, there are assumptions about the rheology and mechanics of materials that are built into specific kinematic models. For example, the kinematic model of Je˘zek and Hrouda (2002) is rooted in the equations developed by Jeffery (1922) to describe the motion of particles within a viscous medium. In fact, the medium need not be viscous, but merely needs to allow the free rotation of particles so that they track the kinematics of deformation without the complication of having to overcome large traction from the medium. Media with more complex rheology, such as wax and clay with approximately elastic-viscous or elastic-plastic rheologies have been used to study Jeffery's kinematic model (e.g. Ghosh and Ramberg, 1976), for example. Alternatively, it has been suggested that in nature, pressure solution, rather than plastic failure, might accompany the rotation of particles within a matrix (Oertel, 1985).

In the gouges and breccias of the Black Mountain detachments, the fabric within the matrix (AMS) is to a first approximation similar to the fabric in the clasts (SPO).

Similar fabric at different scales is inconsistent with a strict application of the Jeffery model even though such behavior describes the kinematics of deformation. Therefore, we hypothesize that *granular flow* (e.g. Wolf, 1997) describes the deformation of the gouge and *cataclastic flow* describes a related type of deformation wherein fracture accompanies flow. Granular flow allows for the dynamic interaction of grains, but is not in conflict with treating the flow field as obeying *kinematic* models similar to those of Je˘zek and Hrouda (2002). Supporting this conclusion is that the interaction of particles with friction contact laws and different sizes produces fabrics and structures in numerical simulations (Morgan and Boettcher, 1999; Morgan, 1999) that resemble those we describe here.

Granular flow in nature can exhibit interesting dynamic properties that phenomenologically resemble fluids and plastic materials, even when the governing mechanics are frictional (Mitchell, 1993). Furthermore, the static strength of granular materials varies with the arrangement of the particles (Mitchell, 1993). If the granular flow model is the correct mechanism to describe gouge deformation, it might explain the apparent weakness of the Death Valley detachments, and the apparent contrast in rheological behavior as preserved by sharp slip surfaces and wider shear zones.

2.10. Conclusions

The shape preferred orientation (SPO) of >50μm-scale clasts, and the anisotropy of magnetic susceptibility (AMS) of the bulk-rock define meaningful deformational fabrics in gouge and breccia from the Black Mountain detachments, Death Valley CA.

The grains that define the SPO are mechanically inherited from the footwall crystalline rocks, and relatively deficient in ferrimagnetic particles. In contrast, the grains that produce the AMS are fine-grained (micron-scale) and ultra-fine grained (sub-micron-scale) magnetite in most samples, and clay minerals in a few samples. The AMS and SPO fabrics are kinematically significant when compared with regional constraints on fault slip, and when compared with the results of established kinematic models. However, the similarity of the fabric in the fine-grained matrix (the AMS) to the larger clasts (the SPO) suggests that the deformation mechanism of the gouges and breccias was similar to granular flow, rather than more dispersive modes of deformation or simple stick-slip behavior across a continuum.

Table 2.1. Sample descriptions and results of Cladouhos, 1999a. $\underline{v}$ is the orientation of the SPO vector in degrees clockwise from the Y-orientation, $\underline{a}$ is the vector strength, and $\underline{R}$ is the average axial ratio of the clasts.

sample	type	V	a	R
A1	Clay Gouge	156	0.34	1.96
A3	Foliated Breccia	144	0.59	2.17
A6	Granular Gouge	178	0.46	1.9
A11	Scaly Clay Gouge	159	0.65	1.98
A13	Clay Gouge	164	0.56	2.05
B1	Granular Gouge	9	0.59	1.89
B2	Granular Gouge	10	0.38	1.97
B34	Foliated Breccia			
D2	Granular Gouge	176	0.71	1.78
D3	Foliated Breccia	165 (BSEI)	0.36	1.71
D4	Clay gouge			
D11	Clay Gouge	163	0.59	1.81
D14	Slip Surface	170 (BSEI)	0.5	1.8

Table 2.2. Shape Preferred Orientation data from this study. The X1-X2 (fault plane), X2-X3 (dip plane) and X1-X3 (strike plane). Other indices are defined in the text and in the caption for Table 1.

sample	V: X2-X3	a: X2-X3	R: X2-X3	V: X1-X3	a: X1-X3	R: X1-X3	V:X1-X2	a: X1-X2	R: X1-X2
A11	172.55	0.4	1.89	11.43	0.46	2.16	162.86	0.17	2.09
B1	179.57	0.59	1.96	0.48	0.38	2.07	154.7	0.22	2.01
B34	157.64	0.43	1.98	18.66	0.34	1.93			
D2	1.03	0.37	2.01	10.93	0.65	1.98	125.35	0.09	1.95
D4	162.86	0.18	1.89	1.79	0.14	2.04	166.34	0.33	1.89
D11	170.53	0.63	2.06	178.52	0.5	1.95	162.67	0.12	1.96

Table 2.3. Anisotropy of magnetic susceptibility of fault rocks. K1, K2, and K3 are the principal axes of the AMS ellipsoid, P, L, F, and T describe the shape of the ellipsoids as defined in the text.

Sample	k_1	Dec-k_1	Inc-k_1	k_2	Dec-k_2	Inc-k_2	k_3	Dec-k_3	Inc-k_3	kmean	P	L	F	T
A1	1.0034	267	41	1.002	177	0	0.9946	87	49	1.21E-01	1.0088	1.0014	1.0074	0.683
A3	1.0181	225	27	1.013	125	20	0.9689	4	56	1.03E-03	1.0508	1.005	1.0455	0.7959
A6	1.0261	349	34	0.9925	131	50	0.9813	245	19	1.03E-03	1.0457	1.0339	1.0114	-0.4927
A11	1.0513	113	19	1.012	205	6	0.9307	313	70	1.02E-03	1.1296	1.0388	1.0874	0.3751
A13	1.0171	169	16	0.997	262	10	0.9858	22	71	1.90E-03	1.0318	1.0202	1.0114	-0.2758
B1	1.0098	241	21	1.0062	146	12	0.984	28	65	7.37E-05	1.0262	1.0036	1.0226	0.7282
B2	1.0126	321	14	1.0011	231	0	0.9863	141	76	1.49E-04	1.0267	1.0115	1.015	0.1301
B34	1.0102	13	21	1.0015	280	1	0.9883	173	68	9.54E-05	1.0222	1.0087	1.0134	0.2125
D2	1.017	89	3	1.0063	358	7	0.9766	202	82	5.91E-05	1.0414	1.0106	1.0304	0.4765
D3	1.0157	51	23	1.0076	145	9	0.9768	255	65	4.91E-05	1.0398	1.008	1.0315	0.5893
D4	1.042	199	35	0.9856	298	12	0.9725	44	53	7.11E-04	1.0715	1.0572	1.0135	-0.6116
D11	1.0278	258	17	1.004	167	2	0.9681	69	72	1.19E-03	1.0617	1.0237	1.0371	0.2169
D14	1.0219	114	51	1.0155	239	25	0.9626	343	28	1.61E-04	1.0616	1.0063	1.055	0.7913

Table 2.4. ApARM vs AMS for UW Fault Rocks

sample	pARM	D max	I max	D int	I int	D min	I min
A1: AMS, c		267	41	177	00	87	49
A1: ApARM, cb	100 mT, 60-10 mT	302	39	197	18	87	45
B2: AMS, c		321	14	231	00	141	76
B2: ApARM, cb	100 mT, 60-10 mT	329	11	233	28	78	59
B2: ApARM2, cb	200 mT, 160-100 mT	320	2	230	27	54	63
D2: AMS, c		89	3	358	7	202	82
D2: ApARM, cb	100 mT, 60-10 mT	151	0	61	19	241	71
D4: AMS, c		199	35	298	12	44	53
D4: ApARM, cb	100 mT, 35-5 mT	330	32	219	30	97	43

AMS – Anisotropy of Magnetic Susceptibility from Kappabridge
Demag - AF Demagnetization level for pARM
pARM – partial Anhysteretic Remanent Magnetization window utilized for ApARM
ApARM – Anisotropy of partial Anhysteretic Remanent Magnetization calculated with k15_s.exe by L. Tauxe.
C – core coordinates
cb – core coordinates, processed with initial demag before all 18 positions

Table 2.5. XRF vs. mean susceptibility.

sample	mean sus	FE2O3 %
A1	1.21E-03	7.25
A3	1.03E-03	8.26
A6	1.03E-03	5.61
A11	6.06E-05	5.39
A13	1.90E-03	9.13
B1	7.37E-05	4.42
B2	1.49E-04	4.05
B34	9.54E-05	
D2	5.91E-05	2.65
D2	9.91E-04	6.79
D2	5.87E-05	5.83
D3	4.91E-05	3.54
D4	7.11E-04	
D11	1.19E-03	5.68
D14	1.61E-04	2.77

Chapter 3: Fault-rock evolution within the Death Valley detachment.

3.1. Introduction

Recently active, mature shear zones exposed at the surface of the earth typically contain specific fault rocks, namely gouge and breccia (Sibson, 1977). Such shallow crustal fault rocks can be seals for reservoirs of hydrocarbons (Knipe, 1992) and contain indications of the direction and amount of tectonic translation on a fault (Chester and Logan, 1987). In addition, rock mechanics experiments raise the possibility that gouge and breccia partly control the strength of faults and the propensity for frictionally unstable, possibly seismic slip on faults (Wu, 1978; Marone and Scholz, 1990; Scholz, 1998; Morrow, 2000).

Fault rocks develop through a combination of the chemical effects of fluids and deformation (Wintsch et al., 1995; Vrolijk and Van der Pluijm, 1999). However, determining the deformation mechanisms and chemical processes that operated within shallow crustal fault rocks is not straightforward. Although grain-scale ductility is suppressed in the upper crust, deformational textures indicative of *mesoscopic* ductility are observed in many gouges and breccias (Rutter, 1986). Furthermore, the reactions between fluids and rocks in the cool, upper crust do not favor equilibration of a single mineral assemblage across the entire shear zone, thereby restricting the utility of metamorphic petrology in understanding the conditions under which deformation occurred.

I present a study of gouge and breccia from low-angle normal, detachment faults exposed on the west flank of the Black Mountains, Death Valley, California. These faults

accommodated Pliocene-Recent extension and have relationships with subsidiary structures that yield information about the mechanics and dynamics of the detachments (Hayman et al., 2003; Chapter 1). The history of the fault rock within the centimeter-to-meter wide detachments is now obscured by large shear strains and at least two generations of mineral growth. I use field relationships, microscopy, geochemistry, and simple geochemical and mineralogical models in an attempt to discern the geologic history of the fault rocks.

Three particularly interesting outcomes of this study are: (1) The gouge and breccia developed in a footwall reference frame as the footwalls were uplifted through the top 3-5 km of the crust; (2) Granular flow superseded cataclastic flow during this denudation; (3) Accompanying denudation was the precipitation of phyllosilicates and oxides via reactions between meteoric water and the fault rock. Point (3) in particular is an important finding because unlike other fault zones (Evans and Chester, 1995; Manatschal, 2000; Yonkee, 2003) evidence for large compositional differences between the fault rock and protolith is lacking, as is the evidence for large fluid flux along the fault plane. Rather than propose a singular controlling mechanism for the strength and the stability of the detachments, I suggest that the change in deformation mechanism from cataclastic to granular flow along a retrograde reaction pathway creates conditions favorable for the faulting observed on the Black Mountain front.

3.2. Methods

Structural mapping of the hanging-wall fault system described in Hayman et al. (2003) (Chapter 1) was conducted with a LEICA laser range finder. A hand-held GPS, Brunton compass, and the geologic maps of Wright and Troxel (1984), Drewes (1963), and Miller (1992a&b) facilitated sampling and analysis of field exposures. Sample names and descriptions are presented in Table 3.1.

The ExxonMobil Production Research Technology Company provided thin sections, X-ray diffraction (XRD) patterns, X-ray fluorescence (XRF) analyses, particle size distribution (PSD) analyses, and silicate oxygen isotope analyses of 45 samples (Table 3.7). ExxonMobil uses a freeze-thaw method to disaggregate samples.

Thin sections prepared at the University of Washington were impregnated with a low-viscosity epoxy (LR-White) under vacuum at 60°C and then trimmed and polished dry. Back-scattered electron images (BSEI) were acquired on the JEOL 730 superprobe at the University of Washington. Electron dispersive spectroscopy was used to identify the composition of mineral phases, although the spectra are not presented here. Element maps were produced by acquiring EDS for specific ranges of the energy spectrum that correspond to outer-shell transitions of the element of interest while rastering the probe across the region. Though not normalized to background, these maps give an indication of the relative abundance of elements within each pixel of the BSEI.

Separations of size fractions were done by immersing the sample in de-ionized water and 0.5% $(NaPO_3)_6$ as a dispersant, and placing the solution in an ultra-sonic cleanser for 2 minutes. Some samples required about 30 seconds of direct impact with a

mortar and pestle. The disaggregated sample was wet-sieved with a 63 μm mesh. 2 μm

separates were prepared with a centrifuge assuming stokes settling. XRD mounts were

prepared by settling the 2 μm separate onto a milipore filter that was then placed face

down on a glass slide. Additional XRD and Laser Particle Size Analyses were done in the

Department of Materials Science and Quaternary Research Center, University of

Washington. Washington State University, Pullman, supplied additional commercial

XRF analyses (Table 3.4).

Transmission electron microscopy (TEM) was conducted in the Department of

Astronomy, University of Washington, and the Department of Earth and Planetary

Science, Johns Hopkins University. Grain mounts for reconnaissance investigation in

120kV TEM were prepared by settling a suspension of clay particles onto a copper grid.

Two samples, B1 and D4 were studied in more detail with a 120kV and 300kV TEM,

each equipped with an energy filter (EDS). A TEM grid of sample B1 was prepared with

ultramicrotome, and sample D4 was prepared for TEM with ion milling.

3.3. The Black Mountains

The Black Mountains flank the east side of Death Valley (Fig. 3.1) and are the

culmination of Miocene through Recent tectonic processes of magmatism, extension,

denudation, and uplift. The Black Mountain detachments bound the Mormon Point,

Copper Canyon, and Badwater turtleback — *turtleback* refers to the antiformal shape that

resembles a turtle shell (Curry, 1938; Wright et al., 1974) — faults, and the Gregory Peak
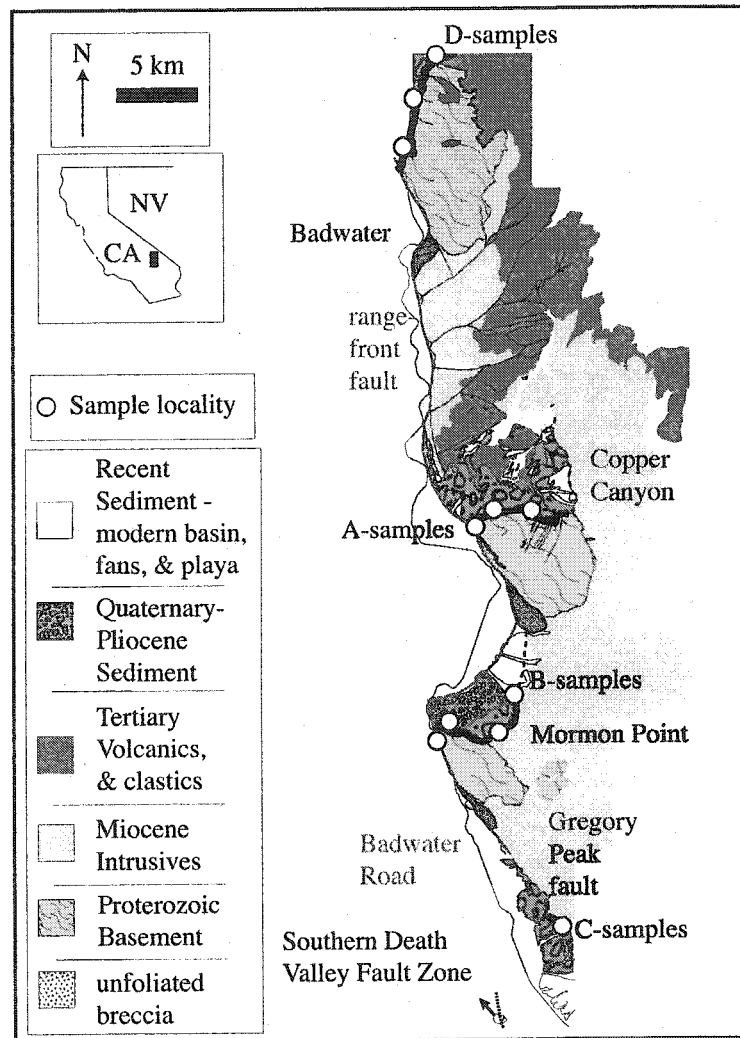
Figure 3.1. Geologic map of the Black Mountains. Fault traces from Miller (1991), Wright and Troxel (1984), and Drewes (1963).

fault (Otton, 1977), also referred to as South Mormon Point (Hayman et al., 2003; Chapter 1).

3.3.1. Geology of the Black Mountains

The turtlebacks are the footwall of the detachments and comprise dolomitic and siliceous gneisses of Proterozoic age. The intermediate Willow Springs diorite and felsic Smith Mountain granite, each of late Miocene age, intrude the Proterozoic section. Research to date has determined that the three turtlebacks ascended from 10 km to less than 4 km between 13 Ma and 6 Ma (e.g. Holm and Dokka, 1993), assuming a geothermal gradient of 30°C/km (Sass et al., 1994). Basaltic dikes and sills post-date all other intrusive rocks and some dikes in the area may be as young as 6-7 Ma (Pavlis, personal communication, 2003), though few reliable dates from these intrusive basalts have been published.

The hanging walls of the detachments are sediments of Pliocene-Quaternary age. Alluvial fans, local playa, and less common sedimentary breccia sheets cover the modern range front and valley floor and are preserved in the sedimentary facies of the older sediments. The oldest sediments contain 5-6 Ma tephra and make up the hanging walls of the Copper Canyon detachment (Copper Canyon formation) and segments of the Badwater detachment (Artists Drive formation) (Holm et al., 1994). The next youngest sediment in the Black Mountains is the Funeral formation, a well-bedded conglomerate that contains Pliocene age tephra such as the 3.1 Ma Mesquite Springs tuff (Holm et al., 1994). The Quaternary-age sediment in the region is the Mormon Point formation that contains the 1.2 Ma Upper Glass Mountain ash, the 0.77 Ma Bishop tuff, and 0.66 Ma

Lava Creek B ash (Knott et al., 1999). The entire section is covered by gravel that was deposited during Oxygen Isotope Stage 6, roughly 0.1 Ma (Ku et al., 1998).

3.3.2. Structure and tectonics of the Black Mountains

Modern Death Valley is 15-20 km across and has opened in the last 5-7 Ma, coeval with the deposition of the Copper Canyon, Funeral, and Mormon Point formations. The three detachments transport and extend these sediments and define the upper surface of the turtleback anticlines. Late Pliocene-Recent extension largely post-dates the basement folds and involves slip on multiple high and low-angle fault segments (Pavlis et al., 1993) that contribute to irregular basement topography expressed in the isostatic residual gravity anomaly (Blakely et al., 1999).

The detachments are coupled with high-angle faults that cut the hanging-wall sediment but do not cut the detachments. At least 14% of Quaternary stretch, or >600m lateral extension ($\cong$1 km of net throw) occurred in the last million years across a 5 km section line of the high-angle fault system (Hayman et al., 2003). The difference in the rate of northwest-directed movement between geodetic stations in the Funeral and Panamint Range is roughly 4 mm/yr with 2-3 mm/yr accommodated on the Black Mountain front (Miller et al., 2001). The geodetic rate of extension is >1mm/yr greater than the measurable extension across the hanging-wall. One proposal to explain this slip deficit is that there are structures other than the detachment system that are responsible for Death Valley extension (Miller and Pavlis, 2003). An alternative hypothesis is that there are intervals of translation on the detachments without internal faulting of the hanging-wall sediment. The proposal for translation on the detachments is consistent with

exposures of the detachment sharply cutting the down-dip limit of the hanging-wall faults requiring an interval of translation on the detachment without hanging-wall faulting. Furthermore, there is > 4 km of exposed footwall up-dip of the exposures of the detachments. The exposed footwall has steep and localized valleys, but erosion does not appear to control the overall shape of the turtlebacks and detachment surfaces. Translation on the detachments is considered to be the most important mechanism for denudation of the turtlebacks.

Fabric elements in the mylonitic footwall, gouges, and breccias, and striae on slip surfaces within the detachment indicate dominantly NW-directed slip, parallel to the hinges of the turtleback (Miller, 1992b; Keener et al., 1993; Hayman et al., 2003; Chapter 1; Chapter 2). Mylonites develop via crystal plastic deformation mechanisms that dominate between 275-400°C depending upon the relative amount of carbonate, quartz, and feldspar in the rock (Tullis, 1990). Therefore the NW-directed slip has persisted since the late Miocene when the turtlebacks were last at temperatures >275°C. Despite the evidence for predominately NW-directed slip, studies of striae and kinematic indicators within the detachments have produced conflicting reports on the kinematics of deformation within the detachment. There are reports of indications for oblique slip on some west-dipping portions of the Black Mountain front (Keener et al., 1993) and fabric elements from some samples are oriented oblique to the cross-sectional plane of the detachments, possibly indicating a pitch to the north in the slip vector on certain fault segments (Chapter 2). The reports for oblique slip and out-of-plane deformation conflict with the measurement of striae that plunge down the dip of slip surfaces in the

detachments and field analyses of kinematic indicators (Hayman et al., 2003; Chapter 1; Cowan et al., 2003). Notwithstanding the conflicting reports of the slip direction, the aspects of the detachments discussed here are not adversely affected by making the simplifying assumption that slip was down-dip and in the dip-plane.

3.3.3. Mechanics and dynamics of the Black Mountain detachments

Below temperatures Ca. 300°C, or above 10 km depth, the failure of rocks is thought to obey the Mohr-Coulomb criterion wherein fault slip is resisted by the static friction of the fault (μ) equal to the ratio of shear to normal stress at failure. The normal stress is modified by the ratio of fluid pressure to lithostatic pressure (λ) within the fault. Because typical earth materials have μ=0.6-0.85 at failure (Byerlee, 1978), both Mohr circle analysis and rock mechanics experiments predict that the optimal dip for a fault in an extensional regime is roughly 60°. While the Mohr-Coulomb criterion does not predict the initiation of low-angle normal faults, it does explain how existing detachments slip at a low angle as a coupled system with hanging wall faults. The most complete application of the criterion to the Black Mountains is in the form of the Coulomb wedge analysis (Dahlen, 1984; Xiao et al., 1991). This analysis relates the effective friction (μ_{eff}) of the detachment — effective friction is the static friction corrected for fluid pressure that departs from the hydrostat with depth — to the critical taper of the overlying wedge of sediment.

The application of the Coulomb wedge model to the Mormon Point wedge suggests that the wedge is critical when $\mu_{eff} \leq 0.4$ for the detachment (Hayman et al., 2003; Chapter 1) and this value is probably representative of all of the detachments. The

wedges that form the hanging walls of the detachments are likely near criticality given evidence for both translation along the detachment and internal faulting of the wedges. The frictional properties of the detachments likely determine the taper rather than geomorphic processes because the Black Mountain front is primarily governed by tectonic denudation. For the Mormon Point detachment stable sliding requires that either the fault rocks have a low static friction, or $\lambda > 0.7$,

Aside from controlling the stability of the range front structure, the detachments exhibit contrasting *frictional* slip stability. Several earthquake-produced scarps are exposed on the valley floor (Brogen et al., 1991). The scarps are produced by faults that most probably belong to the hanging-wall fault system that is coupled with the detachments. Therefore, the rupture produced by earthquakes at depth must have propagated up the dip of the detachment planes. Near the surface of the earth the amount of coseismic displacement on a fault plane during an earthquake is less than that near the hypocenter. The coseismic healing and postseismic elastic rebound required to accommodate the change in rupture along the fault plane can cause strain without accompanying seismicity. Furthermore, there are now widely documented aseismic slip phenomena and deformation closely and strongly post-dating major earthquakes (Wald and Heaton, 1994; Linde et al., 1996; Wernicke, 2000). It is therefore reasonable to propose that slip on the detachments has been both seismic and aseismic over geologic time. Rock mechanics experiments support the hypothesis that the seismic and aseismic slip respectively correspond to unstable and stable dynamic frictional responses of gouge material (Marone and Scholz, 1990).

3.3.4. Summary: Problems addressed by fault-rock studies

The study of fault rocks from the Black Mountain detachments addresses several important problems in both the regional tectonics of Death Valley and the understanding of more general structural processes. The strength of the Black Mountain detachments partly controls the manner in which Death Valley extended and continues to extend. The gouge and breccia may preserve a geological record of the mechanisms governing the strength of the detachments. Earthquake rupture must have either nucleated on and/or traveled up the detachment surface across a certain depth-interval. In contrast, there are likely periods of time during which the detachments slipped without producing earthquakes. The geologic record of frictionally stable and unstable slip may exist in the gouge and breccia. Lastly, the structure and slip kinematics of the detachment at depth and over time remain controversial. Many workers favor a model that predicts that the detachments have a high-angle segment in the top 10 km of the crust in contrast to the structure exposed at the surface (e.g. Miller, 1991). Alternatively, the detachments may project to depth as low-angle faults. If it can be established that the gouge and breccia developed at depth, then the kinematic indicators within the fault rock are evidence that the detachment does not have a high-angle ramp.

3.4. Fault Rocks in the field

In the Black Mountains, the *modern detachments* place sediment directly against basement across a <1m-wide fault zone. Cowan et al. (2003) described many of the field relations and some of the mechanical and kinematic implications of the distribution of

different fault rocks across the fault zones. Here, I further document the field appearance of the fault rocks and structures in the wall rocks, focusing on crosscutting relationships and how the different structures participated in the development of the gouge and breccia. Some of the mylonitic shear zones in the Black Mountains accommodated late Miocene extension, and are possibly deeper crustal equivalents of the modern detachments (Miller, 1992b). The mylonitic shear zones, however, are cut by the modern detachments and the surrounding brittle deformation. I therefore begin my discussion of the field appearance of structures with the earliest phyllonites, cataclasites, and damage zone (cf. Caine et al., 1996) rocks in the footwalls of the detachments.

3.4.1. Footwall structures

The earliest brittle deformation in the Black Mountains are shallowly dipping phyllonitic and cataclastic shear zones that contain fractured, centimeter-scale clasts, typically of quartzofeldspathic gneiss, between foliated domains of fine-grained minerals (Fig. 3.2a). 6-7 Ma basaltic dikes (Pavlis, personal communication, 2003) locally cut these shear zones. Some shear zones in the turtlebacks are cut by an Eocene generation of pegmatitic dikes and are interpreted as thrusts (Miller and Friedman, 1999; Miller, 2003). Not all of the phyllonitic shear zones have the configuration characteristic of thrusts and there are localities where the latest slip postdates the dikes. Therefore, I propose that some of these footwall shear zones are the earliest non-mylonitic shear zones in the extensional history of the Black Mountains.

The next youngest phase of brittle deformation in the turtlebacks created damage zones of breccia and hydrothermally altered crystalline rocks that are unevenly
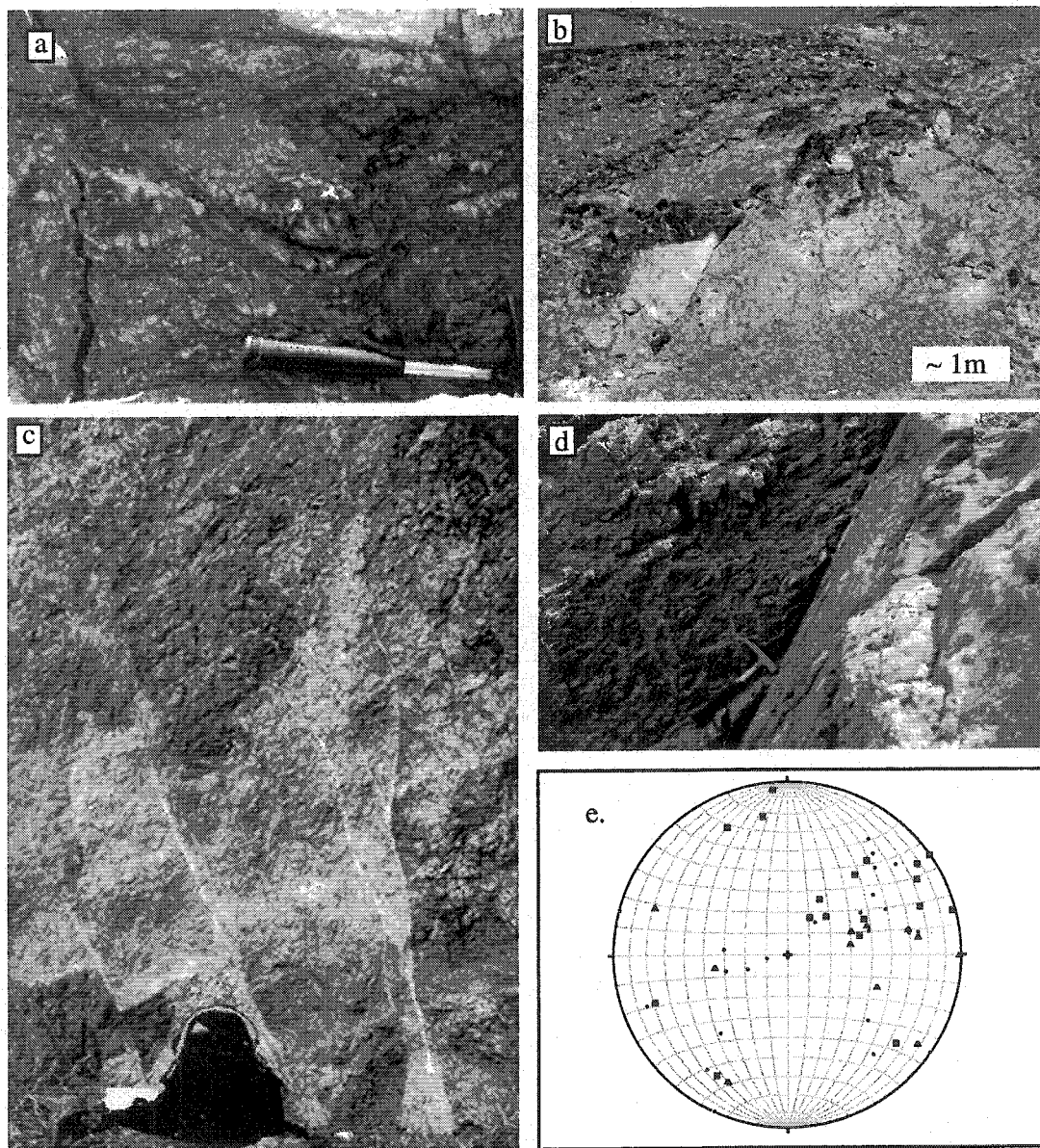
Figure 3.2. structures in the footwall. a. footwall shear zone less than a few meter below (south of) the Copper Canyon detachment and just east of the valley floor. Thin black vein on the left is a basalt dikelet fed from a larger suite of sills and dikes. b. brecciated region at the mouth of Sheep Canyon. Note the semi-continuous layer of quartzite (most of the rocks in the background are part of the Willow Spring Diorite. c. "Damage zone" just south of the Copper Canyon detachment on the valley-wall. d. Footwall fault placing micaceous gneiss against pegmatitic basement on the Badwater turtleback. e. equal area stereoprojection of poles to footwall brittle structures.

distributed along the Black Mountain front (Fig. 3.2b). The deformation that created

these breccias was accompanied by chlorite and epidote mineralization (Byrnes, 1989)

and affected the basaltic dikes. The damage-zone breccias are not associated with a

particular fault or shear zone, but rather coincide spatially with geologic contacts such as

the intersections of fault segments (Pavlis et al., 1993) and the southwestern margin of

the Willow Springs diorite.

Postdating all deformation except for the modern detachments are fractures and

faults that cut the footwall (Fig. 3.2c,d). Although there are several orientations observed

throughout the footwall (Table 3.2; Fig. 3.2e), the fractures, dikes, and faults in the

footwall trend roughly parallel to the strike of the modern detachment in each particular

locality. Many of the fractures are filled with siderite (Fig. 3.3), hematite, or tourmaline

(Byrnes, 1989). Tourmaline is not abundant north of the Gregory Peak detachment.

3.4.2. Breccias

Breccia is a general term for rocks with a clast-in-matrix texture, angular clasts,

and >30% visible clasts in a fine-grained matrix (Sibson, 1977). Layered and bedded

units trace relatively continuously through the damage zones and unfoliated breccias

described in the previous section (Fig. 3.2b) and therefore these rocks do not exhibit

highly localized shear strain that is clearly related to the modern detachments. In contrast,

there are a set of breccias that have deformational fabrics and foliation that are clearly

related to slip on the modern detachments.

Chaotic breccias are the structurally lowest fault-related breccias relative to the

modern detachments. Chaotic breccias contain lenticular, angular clasts of the footwall
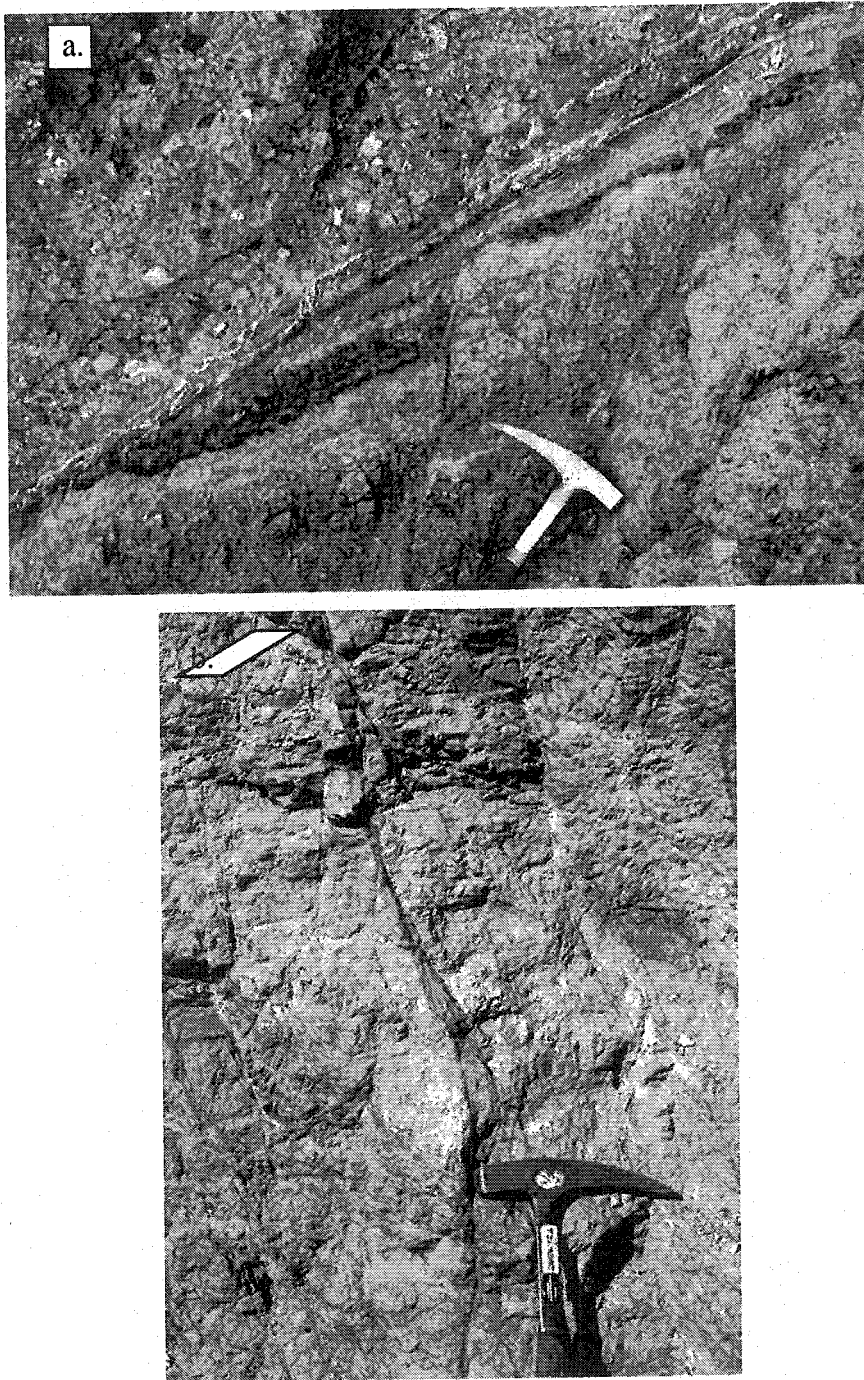
Figure 3.3. Detachment-footwall relationship on Badwater turtleback a. clay-filled fracture intersecting the foliated breccia, but cross-cut by the adjacent gouge layer. b. Clay-filled fractures in the footwall.

carbonates and quartzofeldspathic gneisses that are tens of centimeters across and surrounded by a finer-grained matrix (Fig. 3.4a). The matrix is abundant in silt or sand sized grains and, in places, contains domains of gouge that is rich in green (chloritic and/or reduced) or brown (carbonate and/or hematitic) clays and clay minerals. The large blocks within the chaotic breccia define layering and, in places, folds that shallowly plunge sub-parallel to the strike of the shear zone. Chaotic breccias typically crop out several meters below the exposure of the detachment, and along the NW-striking limbs and the hinge areas of the turtlebacks.

Immediately below the modern detachments are tens of centimeters of breccia with a well-developed foliation (Fig. 3.4b) (Cowan et al., 2003). At the field scale the foliation is defined by the layering of lenticular rock fragments with contrasting lithology, color, or grain size. The rock fragments are derived from the footwall (carbonate gneiss, quartzofeldspathic gneiss, or diorite) and have been extensively altered and strained. The contact between the foliated breccias and underlying footwall rocks is gradational. In places the foliated breccias contain hanging-wall sediment of Quaternary age. In other places, however, the foliated breccias are cut by the surrounding structures, including fractures in the footwall (Fig. 3.3) and the overlying gouge.

3.4.3. Gouge

Most exposures of Black Mountain detachments contain a centimeter-to-tens-of centimeters thick layer of clay-rich gouge (Fig. 3.5, 3.6). Gouge exhibits a variety of structures, textures, and color including both foliated and unfoliated varieties, and brick-red to light yellow or green colors. I follow Cladouhos (1999a) and subdivide gouge into
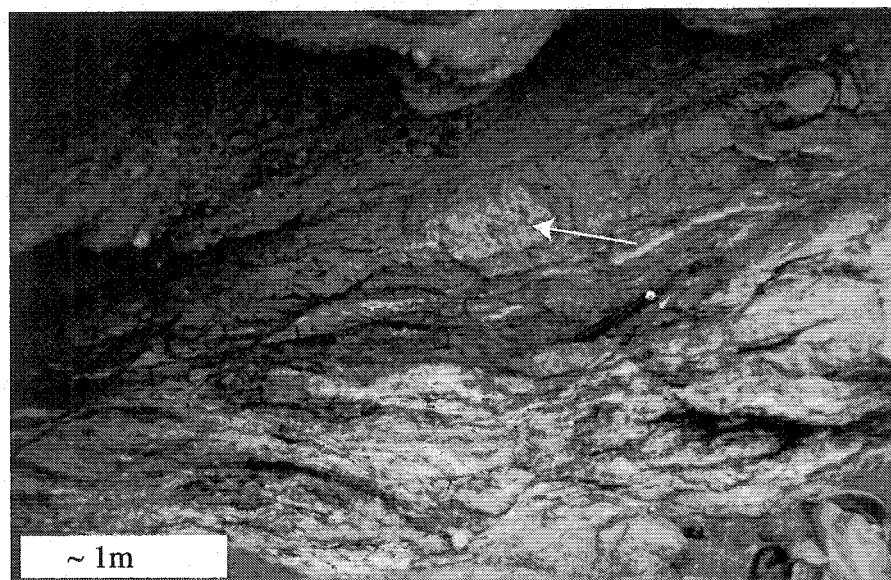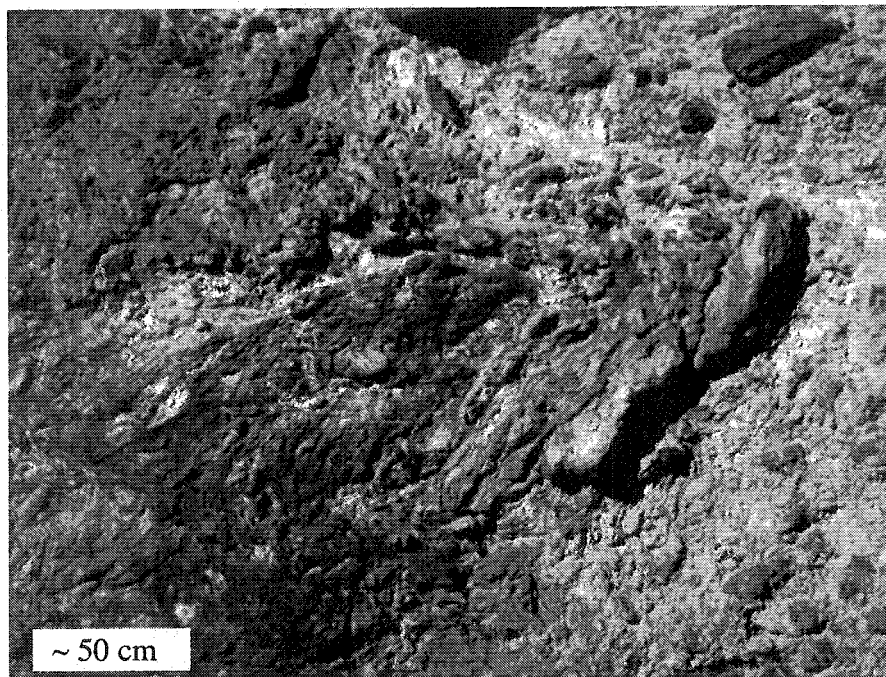
Figure 3.4. breccia units (a) chaotic breccia on west Mormon Point. The lenticular clasts of dolomite are arranged around a SW-plunging fold axis. Small domains of clay gouge are interstitial to the larger blocks. (b) Exposure of the Gregory Peak detachment. The inclined foliation is a P-foliation, and is offset by synthetic riedel shears. Note the layer of hanging-wall sediment (w/ arrow) that is bound by clay gouge.
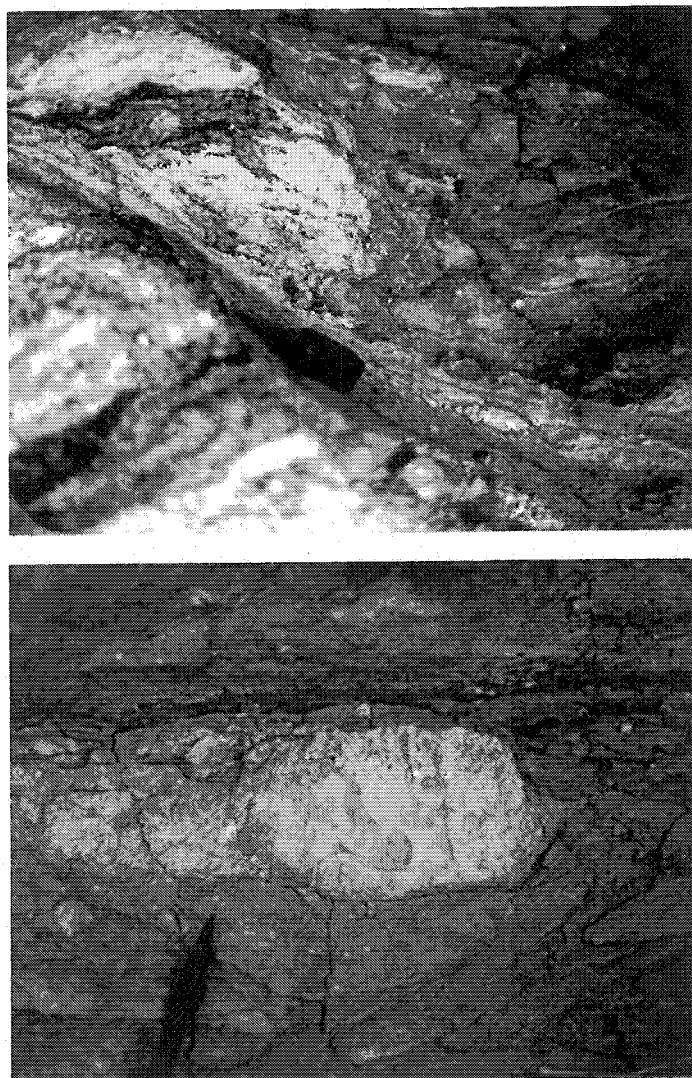
Figure 3.5. Clay gouge. (a) photo from the exposure of the Gregory Peak detachment in figure 3.4b. Clay gouge apparently frozen in the process of abrading the breccia. (b) from an exposure of the Mormon Point detachment at the top, eastern end of Mormon Wash. The upper surface is a slip plane that dips into the plane of the page. A large clast of siliceous gneiss with minor chlorite is surrounding by clay gouge.
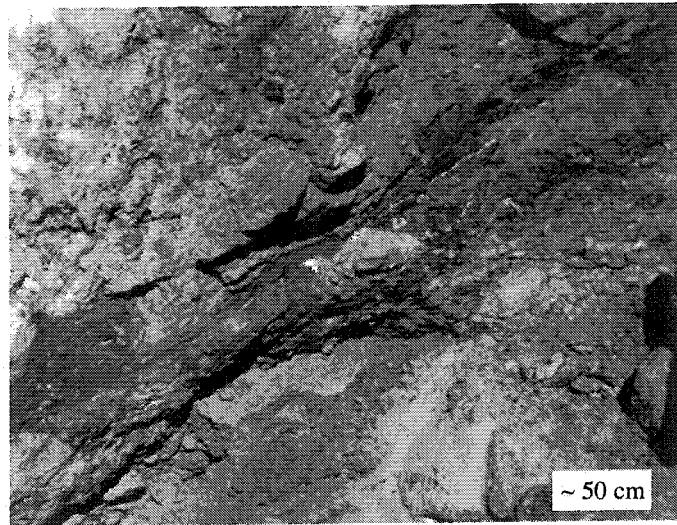
Figure 3.6. Scaly clay gouge. (a) arrows indicate a cross-section of a fracture in the hanging wall of the Copper Canyon detachment filled with scaly clay gouge (left) and a sharp slip plane that cuts large clasts of basalt and carbonate (right). (b) Scaly clay gouge filling a fracture above the Badwater detachment. The fracture is near a fault in the hanging-wall sediment (not shown).

granular gouge with >20-30% visible grains, *clay gouge* with <20-30% visible grains, and *scaly clay gouge* wherein the matrix has an anastomosing, scaly fabric.

Complex structural patterns are observed in the color banding of many gouges (Cowan et al., 2003), including asymmetric tails around larger clasts and infolding of layers. In many places dip-parallel slip surfaces define the boundary between the hanging wall and the gouge, although there are localities where the sharp slip surfaces cut within the gouge. The contacts between the gouge and the hanging wall and between gouge and other fault rocks are not everywhere sharp slip surfaces, but can include more irregular contacts. In many exposures the scaly clay gouge fills fractures and faults in the hanging wall with the scaly foliation roughly parallel to the hanging-wall structures (Fig. 3.6). In other places the faulted blocks of hanging-wall sediment protrude into the detachment and scaly clay gouge wraps around the edges of the fault block.

It is very difficult to tell the composition of the gouges in the field. Bulk-rock X-ray diffraction (XRD) patterns that preferentially measure the coarser-grained, non-phyllosilicate fraction of selected samples demonstrate that quartz, felsdspar, and calcite are the major constituents of the fault rock (Fig. 3.7). Minor salts are present in some samples as well including gypsum (identified in the field) and halite (identified with XRD). Petrographic investigation indicates that in most samples the clasts in gouge are demonstrably from the footwall and dominated by quartz-feldspar or carbonate gneisses (Table 3.3; Fig. 3.8). However, some localities have a thin layer of gouge that is above any slip surface within the detachment, and these gouges contain granite, volcanics, or lithic fragments of the hanging wall. The most dramatic example of
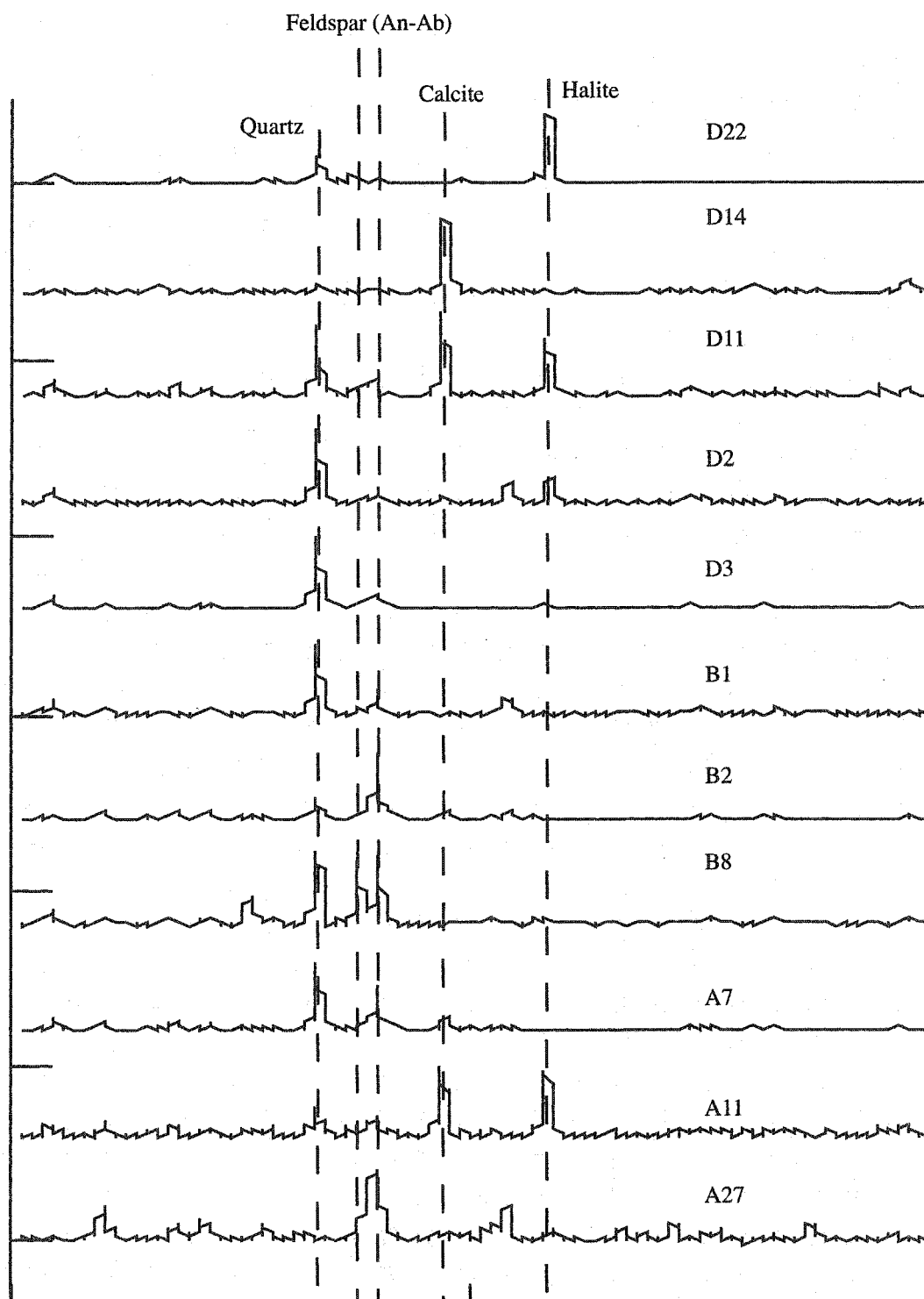
Figure 3.7. Whole Rock XRD analyses. Note that Quartz, Plagioclase, and carbonate are the most prominant peaks, but are not present in every sample.
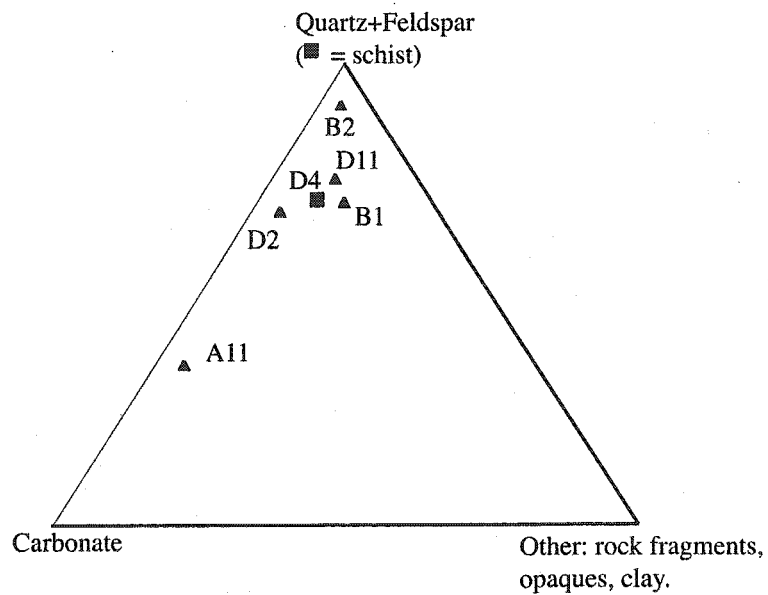
Figure 3.8. Ternary diagram of grain counts presented in Table 3.3. Quartz, plagioclase, and schistose mylonites are from Miocene and older crystalline rocks of the footwall. Carbonates, dominantly dolomite, are also from the footwall. The third (other) category includes rock fragments, clay aggregates, lithic fragments from the hanging wall, and opaque grains. Grains in this category include those that were inherited from the hanging wall sediment.

hanging-wall derived gouge is the Gregory Peak detachment where a 50 cm-thick layer of hanging-wall sediment is bound on each side by a layer of clay gouge (Fig. 3.4b).

3.4.4. Summary: Field relationships

The field expression of the modern detachments, fault rocks, and surrounding structures provides the best evidence for the relative and absolute timing of the different structural units. Clasts of hanging-wall sediment within some gouge and foliated breccias demonstrate that distributed deformation across the detachments postdates deposition of the Pliocene-Quaternary age sediment. Furthermore, the relationships between the gouge and hanging-wall faults are consistent with the hypothesis that distributed deformation within the shear zone is coupled to translation and extension of the hanging wall (Nemser, 2001). In contrast with the hanging-wall related structures, much of the breccia and some of the gouge are isolated from the hanging wall by a sharp slip surface, and contain fragments derived only from the footwall. Layers of gouge crosscut much of the fabric in the foliated breccia (Fig. 3.5) and clay-filled fractures in the footwall either postdate or are coeval with the development of the foliated breccia but predate the gouge (Fig. 3.3). Therefore, the different fault-rock units may have developed over geologic time, since as early as 6 Ma, the age of the oldest sediment in the region and the youngest dikes.

Structures that developed within the fault rock indicate the kinematics and relative amount of strain accrued by the gouge and breccia. The distributed deformation across the shear zone produces several foliation orientations that are approximately parallel (Y-orientation) and inclined (P- and R-orientations) to the dip of the detachment (Cladouhos,

1999a). The foliation exhibits an overall asymmetric zonation from breccia upwards to gouge with increasing parallelism of the foliation with the upper slip surface. Collectively, the fabric elements are evidence that there is systematically more shear strain accrued in the gouge units proximal to the hanging wall, consistent with localization of deformation over time (Cowan et al., 2003).

Estimating the *absolute* amount of strain accrued by the gouge and breccia is not straightforward. Whereas the amount of displacement accrued across the detachments is fairly well known, the expression of the resulting strain varies. For example, any strain across the shear zones is also accommodated by sharp slip surfaces and therefore can only be measured where there are markers for displacement. In fact, clasts that are cut nowhere have a match on the other side of the slip surfaces (Fig. 3.6). Although matching clasts within the fault rock to the wall rock could give a qualitative indication for how much distributed deformation has occurred, in few places can clasts within the shear zones be uniquely correlated with the adjacent wall rock. Despite the uncertainties, one microstructural study (Chapter 2) suggests that the gouge and breccia accrued shear strains >>100, and it is possible that the fabric elements have attained a stable orientation and have not tracked much of the strain within the detachment (Cladouhos, 1999b).

Despite the described valuable information about the relative timing, amount of strain, and overall structural style of the detachments and fault-rock development, less is indicated by the fault rocks about the conditions of their development over time, such as the temperature of formation, or the role of chemically active fluids. Without such information it is difficult to *rule out* that the fault rock developed in the immediate

reference frame underneath young sediments, and accrued relatively modest shear strain. Furthermore, having identified weakening of the detachments and paleoseismicity of the range front, the field analysis of the fault rocks has not, to date, greatly improved our understanding of fault weakening or frictional instabilities. In an effort to better understand the history of fault-rock development, and the mechanisms that operate during their deformation, I now describe the microfabric of the fault rocks in considerable detail.

3.5. Microfabric

Many of the properties of the fault rocks at the field scale are the result of their properties at the sub-millimeter scale. The orientation of grains, the banding of fault rocks at different scales, local slip surfaces, and newly grown minerals are all products of microscopic mechanisms. Studying gouge and breccia is best done with microscopy as many of the grains are too fine grained to identify in the field. Furthermore, continuum descriptions of deformation such as the Mohr-Coulomb criteria are the result of the aggregate behavior of micro-scale mechanisms.

There are two processes involved in fault-rock development: deformation and alteration. Deformation includes both the grain-size reduction (comminution), and the motion of particles (kinematics) to develop fabric. Closely related, and in some cases also a mechanism for accommodating strain, is the precipitation or dissolution of minerals via chemical processes. I present the microstructural observations of the fault rocks and discuss the probable mechanisms for microstructural development, and where and when these mechanisms dominated.

3.5.1. Microfabric and deformation in the wall rock

The microfabric of the wall rock is discernibly different than the fault rock. The footwall of the Black Mountain detachments includes mylonites and phyllonites that exhibit ductile and semi-brittle textures at the grain scale (Fig. 3.9a,b). *Grain scale ductility* requires mechanisms such as intracrystalline strain, and recovery that are crystal-plastic deformation mechanisms requiring the migration of vacancies through a lattice. *Semi-brittle* refers to the combined effect of fracture and pervasive pressure solution, the latter requiring enhanced dissolution along grain boundaries. The mechanisms of grain scale ductility operate in response to changes in strain and interfacial energy above roughly 200-300°C, depending upon the composition and amount of fluid in the system (e.g. Tullis, 1990). Below 200-300°C the energy required to fracture grains is less than that to promote diffusion of lattice dislocations, and the energy required to overcome frictional resistance to sliding is less than that to dissolve grain boundaries. The textures that result from crystal plasticity and pressure solution include continuous layers and micro-domains of insoluble minerals, undulatory extinction of grains in thin section, and strain-free grains that interlock with grain boundaries joining at 120° (Tullis, 1990). In the Black Mountains, younger structures and intrusive rocks crosscut the shear zones that exhibit mylonitic and phyllonitic textures, and geologic constraints place the turtlebacks below 200°C before 6 Ma.

In contrast with the continuous fabric of the footwall rocks, the hanging-wall sediment is characterized by sub-angular to angular grains in a finer-grained matrix (Fig. 3.9c,d). These grains are interlocking in some samples, and supported by the matrix in
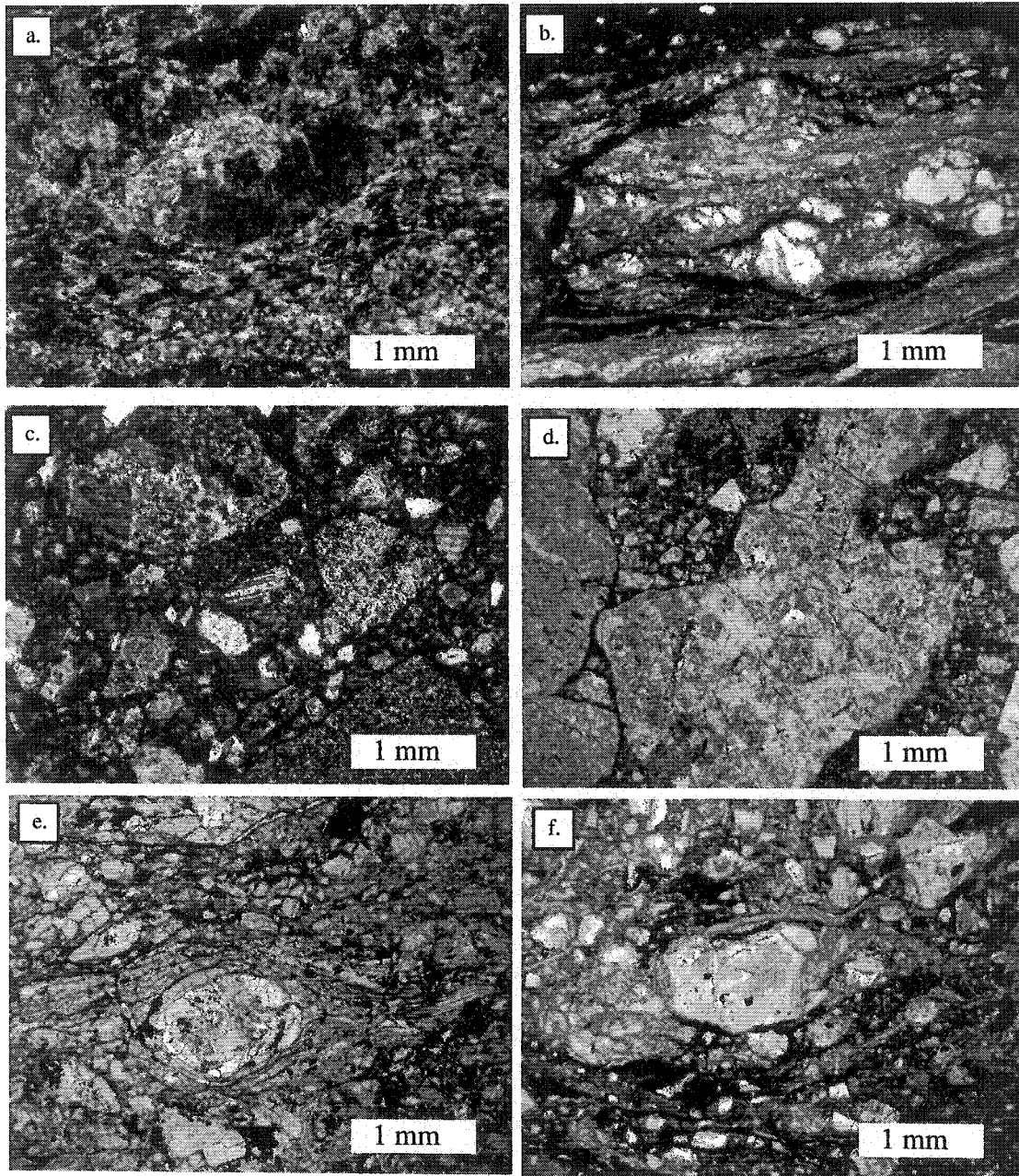
Figure 3.9. Wall rock, gouge and breccia. a. mylonite, b. phyllonite, c. hanging-wall sediment, d. hanging-wall sediment. e. Foliated breccia, f. Gouge.

others. The grains have rough grain-boundaries, and grain fracture is not common.

Although clearly defined at the field scale, bedding cannot be observed at the thin section

scale. Grains within the hanging-wall sediment are mostly crystalline clasts derived from

the Black Mountain footwall exposed to the east. The clasts are dominantly feldspar- and

quartz- rich granite and granodiorite, but basalt, micaceous and/or quartzofeldspathic

schists, and volcanics are also constituents. Deformation across the hanging wall is

localized near faults, although there is evidence for compaction, and non-localized

extension across the hanging wall cannot be ruled out.

3.5.2. Microfabric and deformation mechanisms in the fault rock

The microfabric of the gouge and breccia is differentiable from the footwall

because the fault rocks have a clast-in-matrix, granular texture and not the continuous,

interlocking grain boundaries or folia of the footwall mylonites and phyllonites (Fig.

3.9e,f). The microfabric of the fault rock bears some similarity to the microfabric of the

hanging-wall sediment because each can have a granular texture. However, hanging-wall

sediments nowhere have the weak foliation, pervasive grain fracture, or degree of sorting

observed in thin sections of fault rock. An equally diagnostic difference between fault

rock and hanging wall is the composition of the clasts. The inherited clasts within the

gouge and breccia have a remarkable uniformity of composition. All of the samples have

>60% to as much as 90% clasts of the same lithology: either quartz-rich mylonites with

subordinate feldspar (Mormon Point and Badwater samples), or more varied schists and

carbonates (Copper Canyon and Badwater samples) (Fig. 3.7, 3.8). While it cannot be

ruled out that some of these clasts are derived from the hanging wall, <10% of the clast population in any sample can be indisputably correlated to hanging wall clasts.

The two localized structures observed in the microfabric of the fault rock are fracture and localized slip planes. Fractures vary in character between samples. At the sub-millimeter scale many fractures in the unfoliated breccia are anastomosing and enriched in opaque clay and comminuted material (Fig. 3.10a). In contrast, fracture is confined to individual grains in the foliated breccias and gouges, and the transgranular fractures do not contain comminuted or precipitated grains. Most of the transgranular fractures in the gouge do not extend beyond grain boundaries and are cut by the fabric and structure of the surrounding matrix. In contrast, most transgranular fracture in the breccias is demonstrably syntectonic with the latest deformation.

Another pervasive localized structure in the gouge and breccia are slip planes that cut across both the matrix and clasts (Fig. 3.10b-d). These structures are either planar and parallel to the dip of the detachments (a Y-orientation) or curved and facing down the dip of the detachments (a synthetic riedel orientation). The sharp slip surfaces contain minor amounts of comminuted material, such as sub-micron scale powder that produces aluminum and silicate peaks in electron dispersive spectra (EDS) or enrichment of opaque, likely oxide, minerals. The powder is a mechanical product of wear during slip but the opaque grains are evidence for chemical processes such as preferred dissolution of silicates and/or precipitation of oxides along the slip surface.

Most localities of detachments exhibit a through-going planar and striated slip plane that separates the gouge from the hanging-wall sediment. Interestingly, this
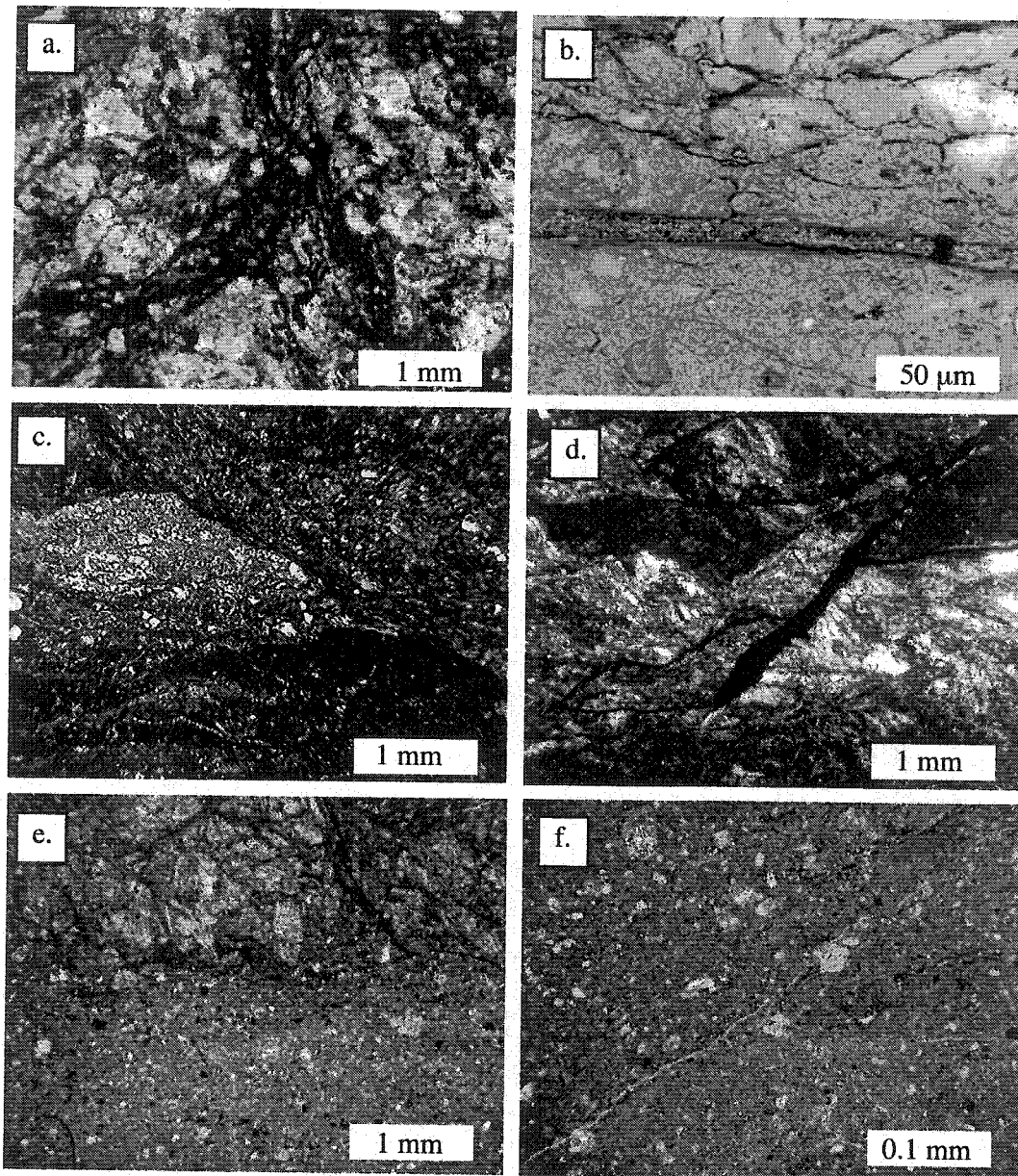
Figure 3.10) Microstructures. a. fracture in footwall. b. slip surface in gouge., c. riedel shear in foliated breccia, d. riedel structure in foliated breccia. e. ultracatclasite below hanging wall sediment. f. close-up of ultracataclasite.

principal slip plane (c.f. Cowan et al., 2003) is not extraordinarily localized in thin section. Rather, the principal slip plane is a <1 mm domain of *ultracataclasite*, distinguished from gouge by having 90-100% comminuted material (Sibson, 1977). Sample D14 is from the slip surface exposed along the Badwater detachment and exhibits several additional noteworthy properties (Fig. 3.10e,f). Firstly, the ultracataclasite contains abundant calcite whereas the adjacent gouges are deficient in calcite. Secondly, the boundaries of the slip surface are irregular as though plucking and abrasion are important processes in the slip plane development. The irregular contacts contrast with localized slip surfaces within the gouges that in most places have sharp boundaries.

Despite the prominence of localized structures, the more characteristic microfabric of the fault rock, and the gouge in particular, is the clast-in-matrix, granular texture (Fig.3.11). Systematic analysis of the orientation of hundreds of grains in several thin sections demonstrates that there is a well-defined shape preferred orientation despite lack of a preferred orientation upon casual inspection (Cladouhos, 1999a; Chapter 2). The shape preferred orientation is present at all grain-sizes, resulting in a magnetic fabric produced by micron and sub-micron grain magnetite and clay minerals (Chapter 2). Another property of the granular fabric is the presence of irregular surfaces between domains of contrasting texture and/or composition in many samples (Fig. 3.11a-d). These distributed textures contrast with the localized slip surfaces that cut across both grains and the fine-grained matrix (Fig. 3.10e, f).

A comparison of the microfabric of several samples reveals a decrease in the number of grains in contact with one another, amount of transgranular fracture, and
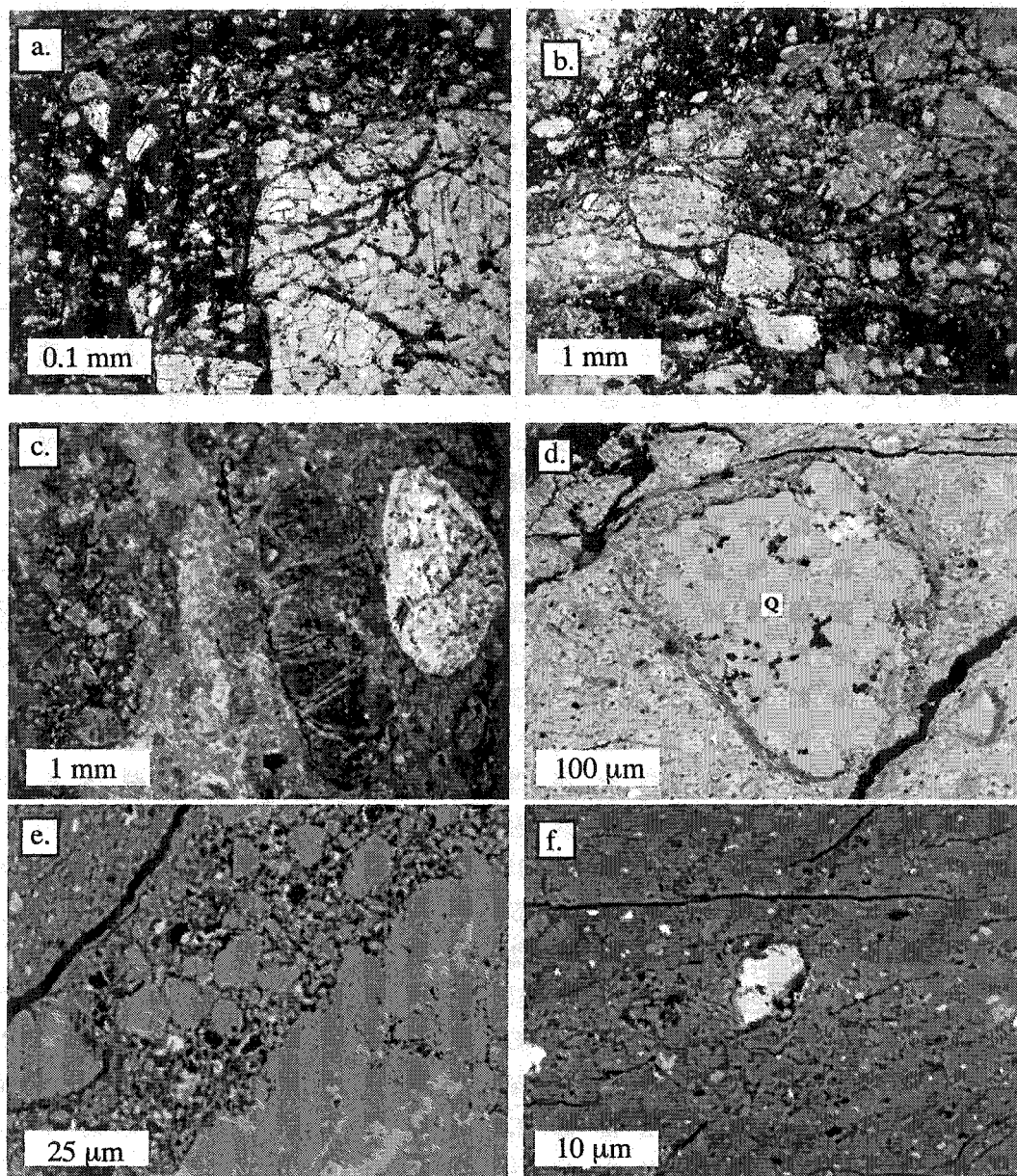
Figure 3.11. Comminution. a. transgranular fractures from brecciation facilitate incorporation of clasts into the clay-rich matrix of gouge. b. Cataclastic flow involved movement of grains and transgranular fracture, effectively comminuting the breccia during flow, c. in the same field of view, well-rounded crystalline clasts next to altered and fractured clasts, and communitued clast, d. abrasion of grain boudnaries of quartz suspended in finer grained matrix. e. close-up of grain boundary that underwent abrasion and plucking. f. small clast of quartz near or at its grinding limit.

intensity of foliation between breccia and gouge. A study of the magnetic and clast-defined fabrics in the fault rock demonstrates that particles of all sizes are arranged in fabrics that developed in response to strain (Chapter 2) such that even sub-micron grains have a preferred orientation that is consistent with the deformation across the shear zones. Stratification of clay-sized grains of contrasting color and composition is present in some gouges and results in irregular contacts between granular and clay gouges (Fig. 3.11). Abraded grain boundaries of large (tens of microns) clasts are present in gouges where the grain contacts between these large clasts are few (Fig. 3.12). The textural observations are evidence for grain-interaction at all scales and illustrate that through this interaction the grains were able to arrange themselves into complicated textural configurations.

One method of quantifying the textures observed in thin section is to measure the particle size distribution (PSD) of the fault rock (Fig. 3.13). While the PSD of any rock or sediment can have gaussian or log-normal distributions with multiple modes of sizes, this detail is largely subsumed within a power-law that describes the PSD in mechanically comminuted materials. The power law is described by the fractal dimension, D, that is related to the number (N) and size (S) of particles by: $N(S) = S^{-D}$.

Sammis et al. (1987) found that many fault rocks had PSDs that fit a power-law with a scale-invariant $D \cong 2.6$. More recent analyses found that D will increase for finer-grained gouges relative to coarser breccias, including D>3, an overpacked fractal dimension (An and Sammis, 1994; Morgan et al., 1996). D also deviates from the power-law at sand and clay grain sizes, suggesting that there is some critical size at which
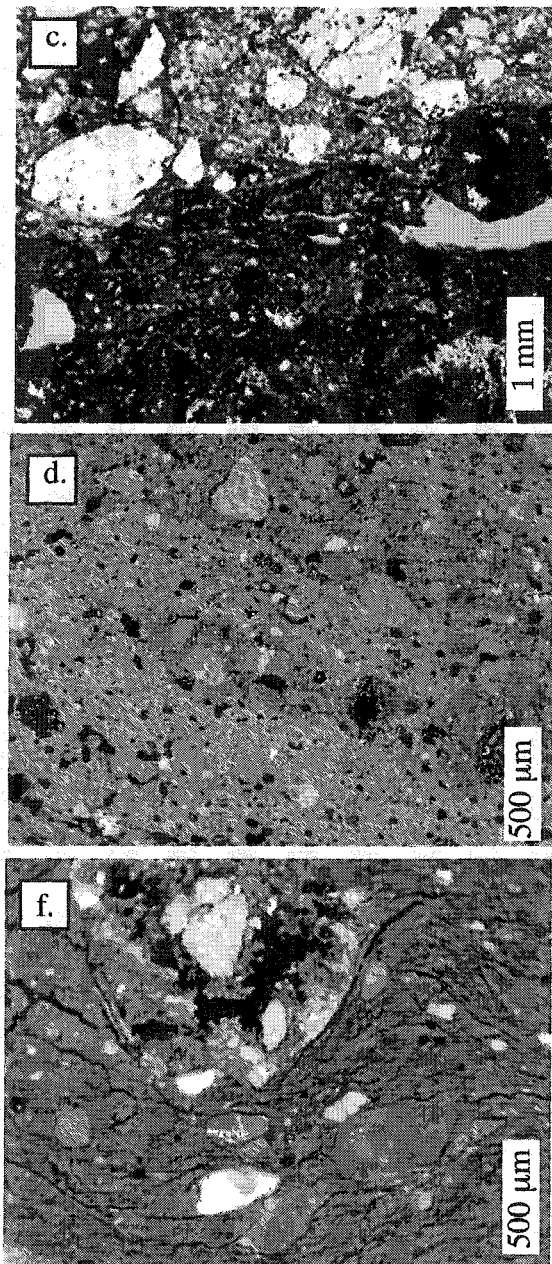
Figure 3.12. granular flow in gouge. a, stratification of contrasting composition of gouge-matrix without a change in fault rock unit. b. domainalization of contrasting composition in texture of clay gouge. c. scaly clay gouge textures.
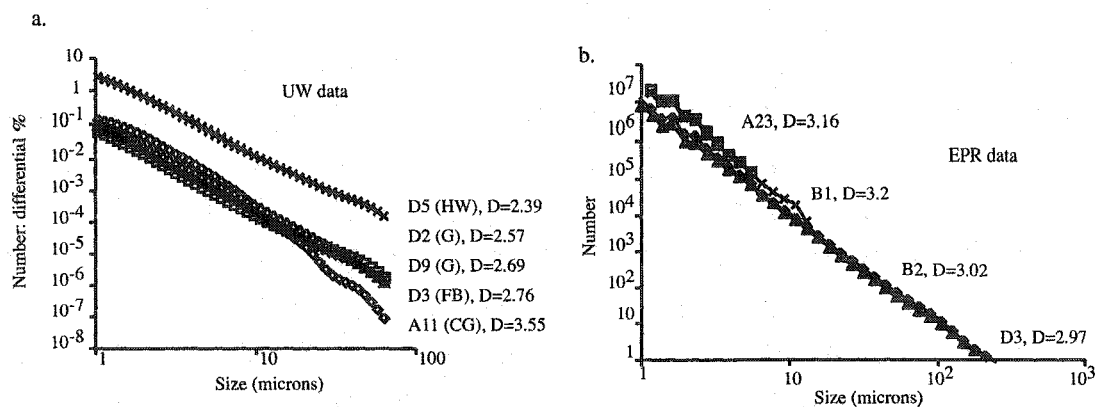
Figure 3.13. Fractal dimensions (D) of particle size distribution. a. Mechanically disaggregated. b. Freeze-thaw disggregation Inconistencies between the data underscore the difference in method of disaggregation and measurement.
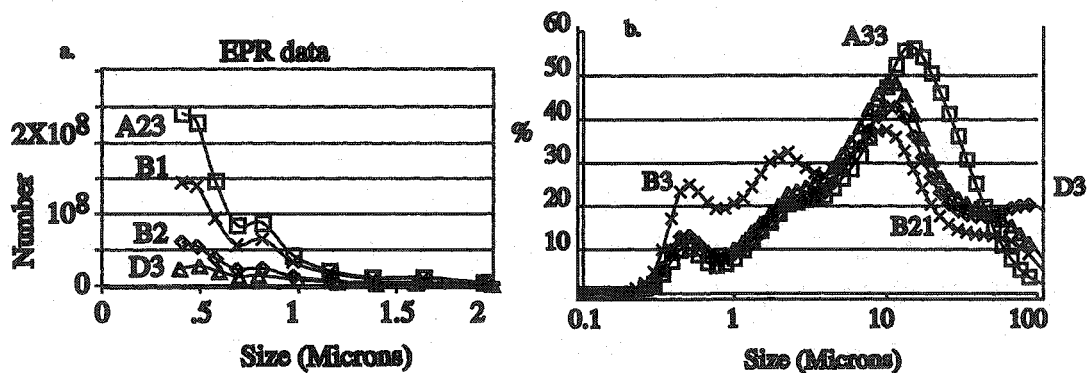
Figure 3.14.Non-fractal PSD. a. clay-sized distribution of particle sizes measured at EPR. b. lognormal distribution measured with a Hareba laser particle size analyzer.

particle interaction deviates from the comminution process affecting the bulk volume. Therefore, D≅2.6 is not a universal value, but rather is a value describing gouges with grain sizes at some critical size lower than the slip distance or amount of strain. In experiments done on gouge analogs, D approaches 2.6 with increasing shear strain, and results in localized slip domains such as riedel shears that have D>2.6 (Marone and Scholz, 1989).

There are three sets of PSD measurements from the Black Mountain detachments (Fig. 3.13; Table 3.7). Two sets of data were produced by disaggregating the sample in solution and then measuring the PSD with a laser particle size analyzer (LPSA). The solution prepared by Peter Vrolijk (Morgan et al., 1996) was prepared by disaggregating the sample with a freeze-thaw method and the other solution was prepared by Hayman with a mortar and pestle. The third set of measurements was attained by counting grains of different sizes in thin section (Scharer, 1996). Calculations of D from thin section are consistently 0.8-1 less than three-dimensional measurements of PSD with laser particle size analyzers (Fig. 3.13c vs. b), roughly consistent with the rule that two-dimensional measurements differ from three-dimensional measurements by $D^{3D}-1=D^{2D}$ (Turcotte, 1992). Separations with a freeze-thaw method increased D by roughly 0.2 relative to those disaggregated mechanically. However, the separations prepared with the freeze-thaw method produced PSD data that compare more favorably with the thin section measurements, and therefore the freeze-thaw method is considered more robust.

Notwithstanding uncertainty surrounding the issue of sample preparation techniques, three general statements can be made about the PSD of the fault rocks from

all of the data. (i) The rocks from the Black Mountain detachments have a range of D from 2.57-3.55 (Fig. 3.13). (ii) One sample of sediment from the hanging wall has D=2.39. (iii) Samples of fine-grained gouge have D>3, whereas breccia and granular gouge have D<3.

Observations of the microfabric and measurements of the PSD collectively illustrate that there are several deformation mechanisms that accommodate strain and controlled the textural development of the fault-rock: comminution, cataclastic flow, granular flow, and slip localization. I discuss the genetic connotations of each of these terms in the Discussion section following further presentation of textural and geochemical data.

3.5.3. Authigenesis

There is a systematic increase in the number of grains with sizes <1-2 μm in clay gouge relative to coarser gouge and breccia (Fig. 3.14a). This enrichment in clay-sized grains is indicated by deviations from the power-law in the size-spectra. Across the size spectra from 2-100 μm breccias have a tri-modal distribution and gouges have a bimodal distribution (Fig. 3.14b). There are several competing processes that give rise to these PSD spectra. Comminution models draw on the empirical and probabilistic grinding limit as an explanation for such behavior (Sammis et al., 1987). Another phenomenon that affects PSD is the tendency for clay particles to flocculate, forming larger aggregates of smaller grains (An and Sammis, 1994). Flocculation contributes to scaly fabrics and has been observed in reconnaissance TEM of the Black Mountain clay gouges.

A third process that can contribute to the relative abundance of grains $< 2\mu m$ is the growth of new minerals, or authigenesis. Authigenesis is likely important to the particle size distribution given grinding limits for material, and the fine grain size favored by the growth process at low temperature. The gouge and breccias are so highly strained that evidence for mineral growth within the rock is cryptic. However, several phases precipitated late in the history of the detachments and provide insight into the mechanisms of authigenesis.

Imagery from the sub-micron scale reveals that nanoscale and unstrained particles nucleated and grew within pores of the gouge and breccia. Low-order, nearly amorphous grains of low-order clay minerals, non-silicate minerals (including Cu- and S-bearring gels) and blocky grains of orthoclase are some nanoscale phases imaged in the fault rock (Fig. 3.15a, b). At the micron scale chlorite fills microfractures in the breccia and footwall, the product of mineral growth and not mechanical inheritance of older metamorphic chlorite (Fig. 3.15c).

Another set of minerals that grew late in the history of the shear zone are non-silicate minerals including iron and manganese oxide, manganese carbonate, and rare manganese silicate (Fig. 3.15d-e, 3.16). These phases are present as sub-micron scale grains and form selvages that fill fractures and coat grain boundaries throughout the fault rock. Their spatial extent is limited. The manganese oxides in particular, are surrounded by finer grained "halos" of the same material (Fig. 3.16). The location and distribution of manganese is more localized and proximal to the parent grain than the distribution of $Fe^{2+/3+}$ and the mobile ions such as K^+. The distribution of Mn^{x+} — the oxidation state of
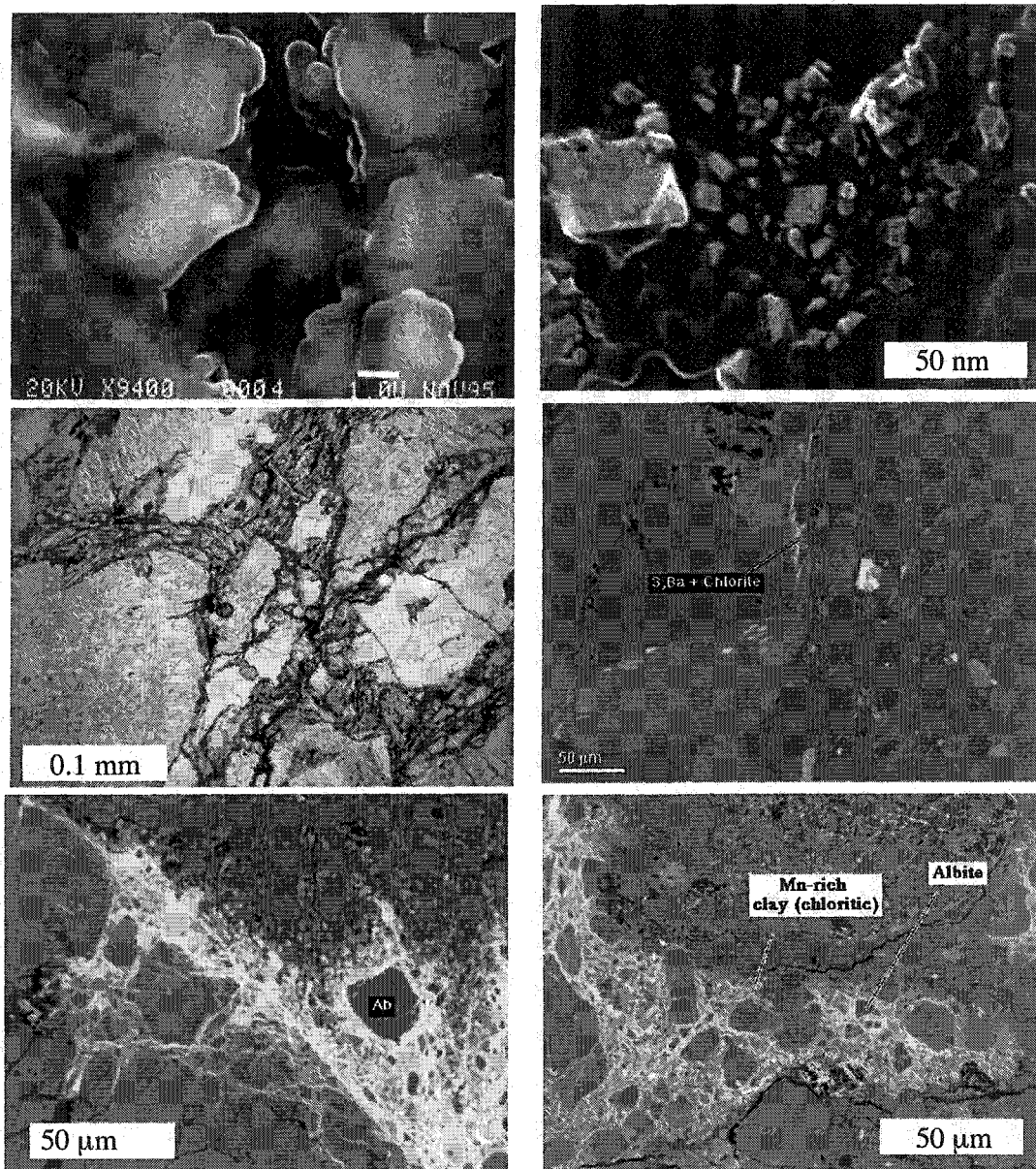
Figure 3.15. Authigenic textures a. low order smectite and associated gels. b. grains of orthoclase. c. chlorite filling a fracture. d. grain of chlorite with inclusions of Ba and S. d. Albite grain in a selvage of Mn-oxides. e. Mn-rich and chlorite selvage forms a reaction front.
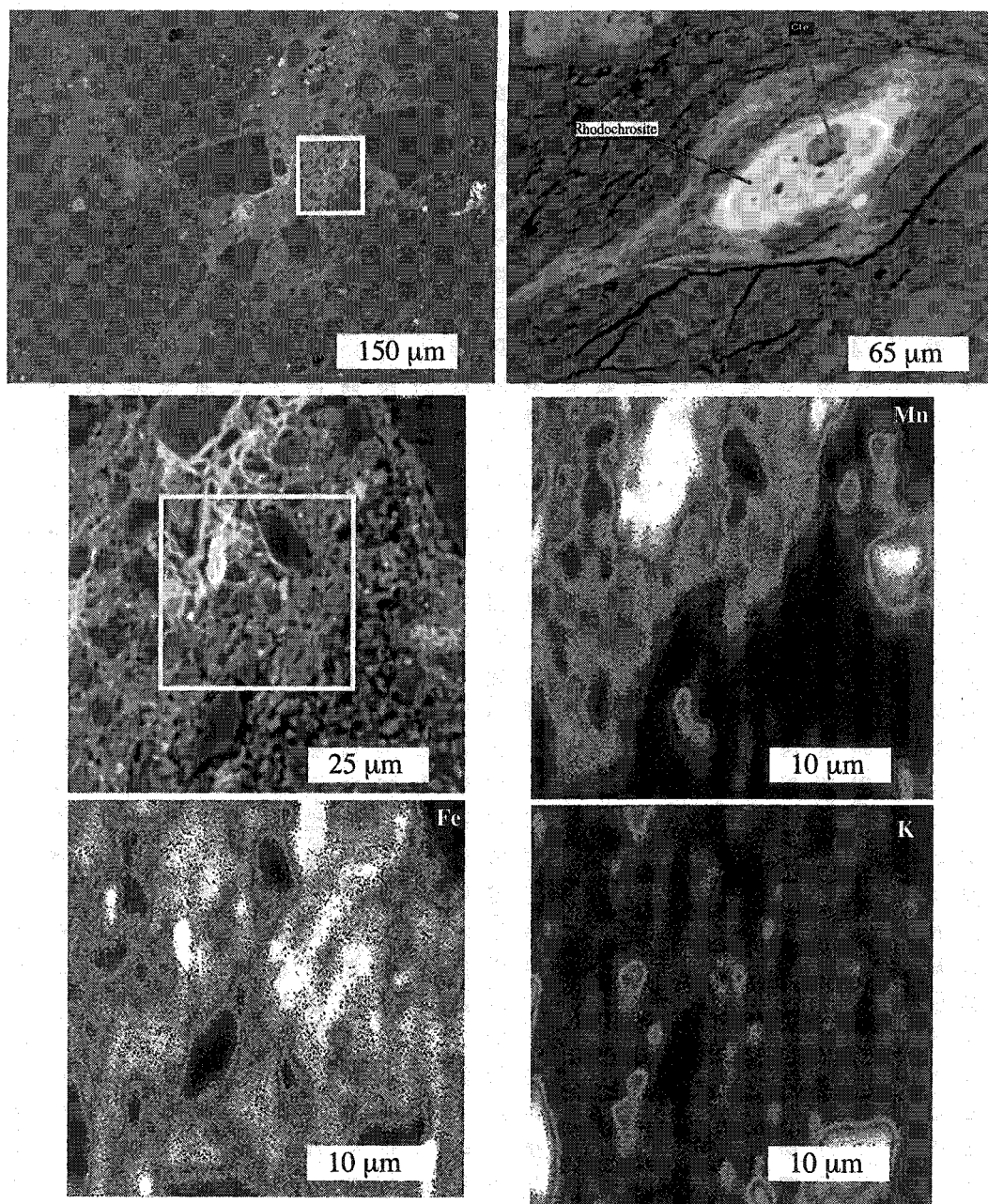
Figure 3.16. Manganese authigenic textures a. Mn-oxide reaction front. b. deformed lens of Mn carbonate. c-f are closeups and (EDS) element maps of the boxed area in a.

manganese is not known, although Mn^{2+} is the common oxidation state of manganese in sedimentary environments — proximal to its parent grain is consistent with transport kinetics governing the distribution of phases, rather than growth kinetics or mechanical mixing (Postma and Appelo, 2000) (Fig. 3.16). Therefore the Mn-bearing phases precipitated along reaction fronts proximal to their parent material.

Suitable interpretations of the authigenic textures are that the nucleation and growth mechanism is precipitation from solution in pore spaces, within fractures, and along grain boundaries. However, any minerals that grew prior to recent shear strain no longer exhibit textures diagnostic of their nucleation and growth mechanisms. For example, the manganese oxides that preserve authigenic textures are strained into elliptical domains enriched with the oxides (Fig. 3.16b). Future deformation would eventually eliminate the growth-controlled microstructure.

The mutual exclusivity of deformational and growth textures is the main obstacle to understanding the history of the clay minerals in the fault rocks. Clay minerals are dominantly phyllosilicates and grew at an earlier stage in a different environment and are now dispersed throughout the matrix of the gouge and breccia. Some aggregates of chlorite have inclusions of S and Ba that are also found in the matrix surrounding late authigenic feldspar (Fig. 3.15b) and perhaps the clay minerals also grew within pores from solution. A precipitation mechanism for the clay minerals is also consistent with the phases present as described in following paragraphs and Discussion.

X-ray diffraction (XRD) of all breccia and gouges demonstrates that the <2µm fraction is dominated by a suite of phyllosilicate clay minerals (Fig. 3.17).
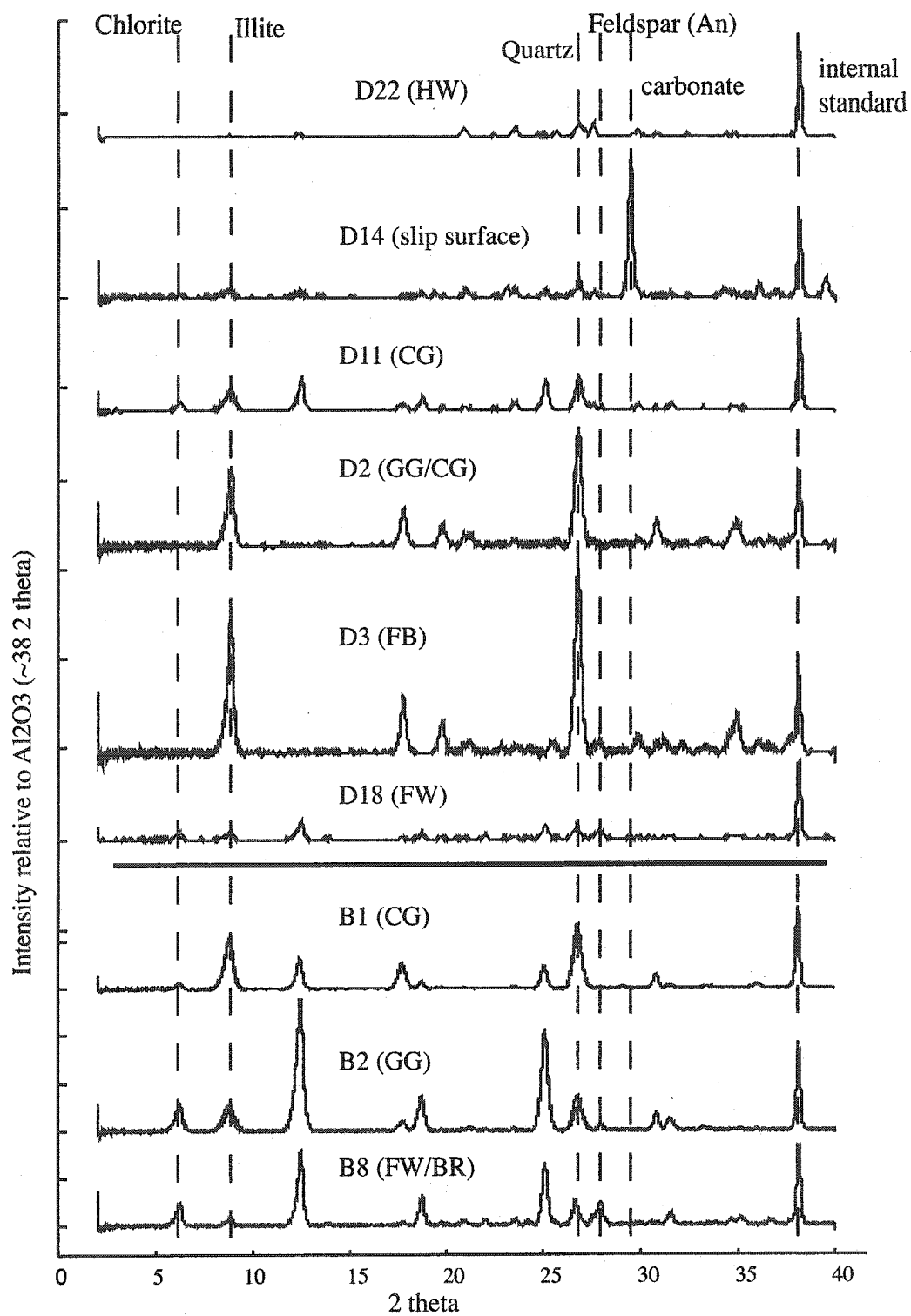
Figure 3.17 (caption on following page)
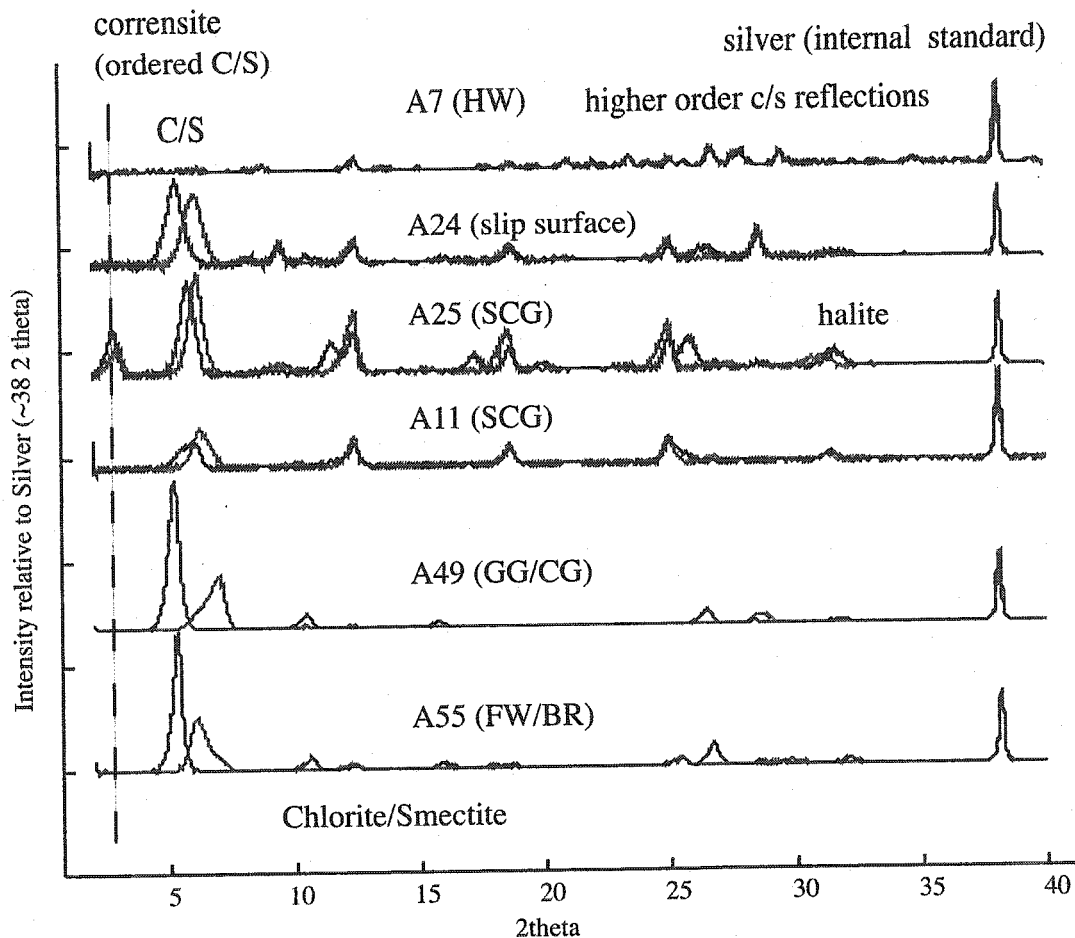
Figure 3.17. Clay XRD patterns. HW=hanging wall, SCG=sclay clay gouge, CG=clay gouge, GG=granular gouge, FB=foliated breccia, BR=breccia, FW=footwall, and slip surface is the slip plane at the contact between the hanging wall and the gouge. The slightly lighter colored pattern shifted to the right is the solvated pattern, and the peak at 38 2theta is an added internal standard. Although swelling clays are not conspicuous on patterns from Badwater (D) and Mormon Point (B), the illite peaks are not exactly at 8 2theta, and a ~0.1 shift in 2theta is observed. The presence of swelling clays and polytypes of illite is confirmed with TEM.

Badwater and Mormon Point are dominated by illite that produces {001} reflections that are not exactly, but close to, ideal 2M polytypes with no swelling component. However, slight (0.1 2θ) shifts in the {001} reflection, and slight deviations in higher order reflections from an ideal 2M illite indicate the presence of some swelling and 1M illite. Samples from Copper Canyon are dominated by a very unusual type of chlorite that is interstratified with saponite, a Mg-rich (trioctahedral), water-bearing clay mineral of the smectite family. The shift in the {001} reflection with solvation is indicative of disordered interstratified clay mineral with randomly alternating layers of smectite and chlorite. The one exception to this disorder of clay interstratification is a scaly clay gouge that has an ordered corrensite phase that produces a prominent peak at <5°2θ. Observation with TEM (not shown) demonstrates that the physical properties of the chlorite-smectite derive from its turbostratic crystallographic ordering with the rotation of the lattice about a zone axis every few d-spacings. It is noteworthy that every sample of scaly clay gouge contains this phase suggesting that the fabric is partly controlled by the crystallographic properties of the swelling chlorite. Another interesting property of the XRD patterns is that the hanging wall sediment of Badwater and Copper Canyon do not have clay minerals similar to those shared by the gouge.

Samples with interstratified chlorite-smectite have few other clay mineral phases. Several of the samples of breccia from Badwater and Mormon Point have only illite, whereas the clay gouges have illite and chlorite with some indication of polytypism and swelling. In an effort to determine the specific clay mineralogy of these samples, and the physical control of the clay minerals on the fabric of the clay gouges, I studied sample D4

Fe-Ch · Il

Mu · Q
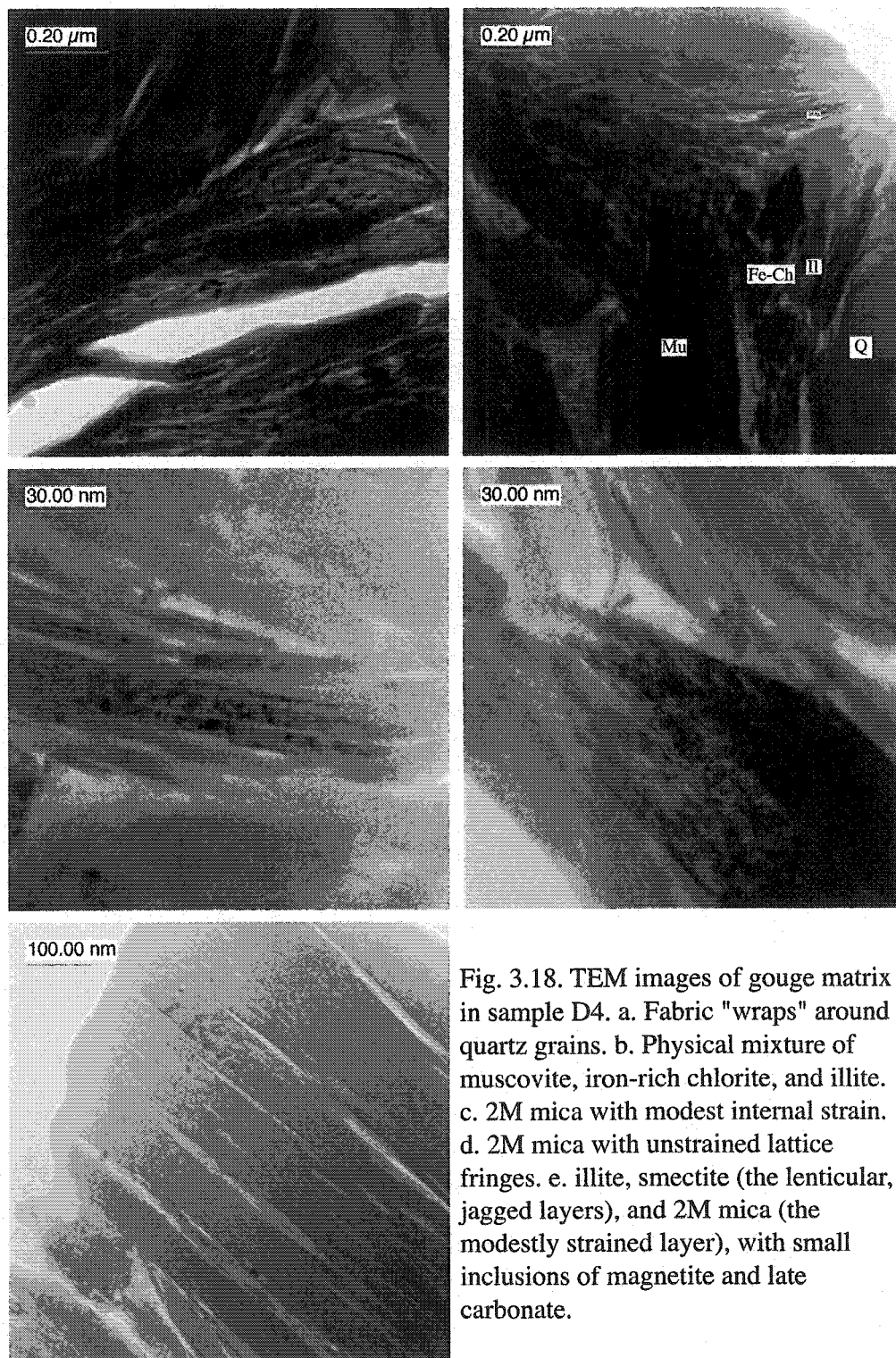
Fig. 3.18. TEM images of gouge matrix in sample D4. a. Fabric "wraps" around quartz grains. b. Physical mixture of muscovite, iron-rich chlorite, and illite. c. 2M mica with modest internal strain. d. 2M mica with unstrained lattice fringes. e. illite, smectite (the lenticular, jagged layers), and 2M mica (the modestly strained layer), with small inclusions of magnetite and late carbonate.

(similar to D11) in considerable detail with TEM and HRTEM equipped with an energy filter (Fig. 3.18). The clay-rich matrix of sample D4 includes finely packed phyllosilicate that are individually lath-like in habit and relatively unstrained, but as aggregates "wrap" around quartz grains. The clays are aggregates of muscovitic illite, chlorite, and smectite. Some of the illite is highly ordered with straight, unstrained, and evenly spaced (10Å) sheets. Other illite has lens-like layers of hydrous clay (smectite) and modest internal strain. Coeval with the growth of much of the illite are nanometer scale grains of magnetite that adhere to the crystals (Chapter 2). Nano-scale carbonate, feldspar, and oxide mineralization is demonstrably later than the growth of the phyllosilicates with the possible exception of magnetite that may have grown coeval with the growth of the swelling phyllosilicates.

3.5.4. Summary: interplay between deformation and growth

The fault rocks have a microfabric that developed via a combination of deformational and growth processes. Crystalline basement was comminuted by fracture and abrasion of grain boundaries during cataclastic flow, and grain boundary abrasion continued even after the gouge developed a granular, clast-in-matrix texture. Cataclastic and granular textures contrast in amounts of syntectonic intragranular fracture (a cataclastic texture), and interstratification of grains of different compositions by mixing (a granular texture). The difference between the cataclastic and granular textures is also marked by differences in the PSD with D<3 and D>3, respectively.

Many of the clay-sized minerals that make up the matrix in the fault rock grew within the fault zone. Feldspar, carbonate and disseminated oxides (notably Mn-oxides)

precipitated within pore spaces and along reaction fronts both post-dating, and just prior to, the most recent deformation within the detachments. An older generation of minerals is phyllosilicates including illite, chlorite, and interstratification of the two with swelling, water-bearing clay (smectite). The clay minerals are now fully incorporated in the deformational fabric.

Several initial conclusions can be made from the observations of the microfabric of the fault rocks. While much of the mineralogy required the presence of an aqueous solution in the history of the detachments, the phases precipitated more-or-less passively within pore spaces and not within through-going fractures or veins as reported in many faults worldwide (e.g. Manatschal, 1999). Furthermore, the deformation of the aggregates of the newly grown minerals did not occur simultaneously with their growth. Minerals precipitated, the shear zone was strained, and the particles developed preferred orientation and other distributed textures. These textures were later affected by localized structures. Lastly, some of the newly grown phases, and the chlorite-smectite phases in particular, have crystallographic properties that partly control their mineral habit. A possibly analogous mineral system is antigorite that commonly forms in veins and fault zones, has a crystallographically controlled flexure to its unit cell, and has frictional properties that favor frictionally stable sliding (Reinen, 2000). A tentative conclusion that can be drawn from the microstructural observations is that the growth of new minerals and not the episodic increase in fluid pressure was the dominant weakening mechanism in the Black Mountain detachments. The "reaction-weakening" (cf. Wintsch et al., 1995)

hypothesis is considered more fully after presentation of important geochemical data attained from the fault rocks.

3.6. Geochemistry of detachments

Research in other fault zones (e.g. Evans and Chester, 1995; Manastchal, 2002; Yonkee et al., 2003), has shown that geochemical variability across faults provides an important record of the flux of fluids along or across a fault plane. In theory, fluids are important to the slip dynamics of a fault. For example, fluctuation in fluid pressure will correspond with intervals of dilation or compaction of fault rock, and this variation should be accompanied by the infiltration of fluids into and out of the local rock volume (Sibson, 1992). With the infiltration of fluids, the new fluid and surrounding rock should be out of equilibrium with one another and reactions should proceed whereby previously soluble minerals precipitate. Because some of these minerals have bonded water, or even water molecules, these phases may provide additional data about the isotopic composition of the water. Non-meteoric water is an indication of such fault-valve behavior as large fluid flux might draw on deeper crustal fluids.

The Death Valley detachments differ in a fundamental way from other fault zones in that there are virtually no syntectonic veins (Cowan et al., 2003). Rather, the record of fluids within the fault is preserved in minerals that precipitated within the pore spaces of the rock over geologic time. Bulk-rock X-ray fluorescence (XRF) analyses provide the most complete measure of the reactivity of the fault zone via the comparison of the wall-rock and fault-rock composition (Fig. 3.19; 3.20; Table 3.4). An *isocon* line (Grant, 1976)
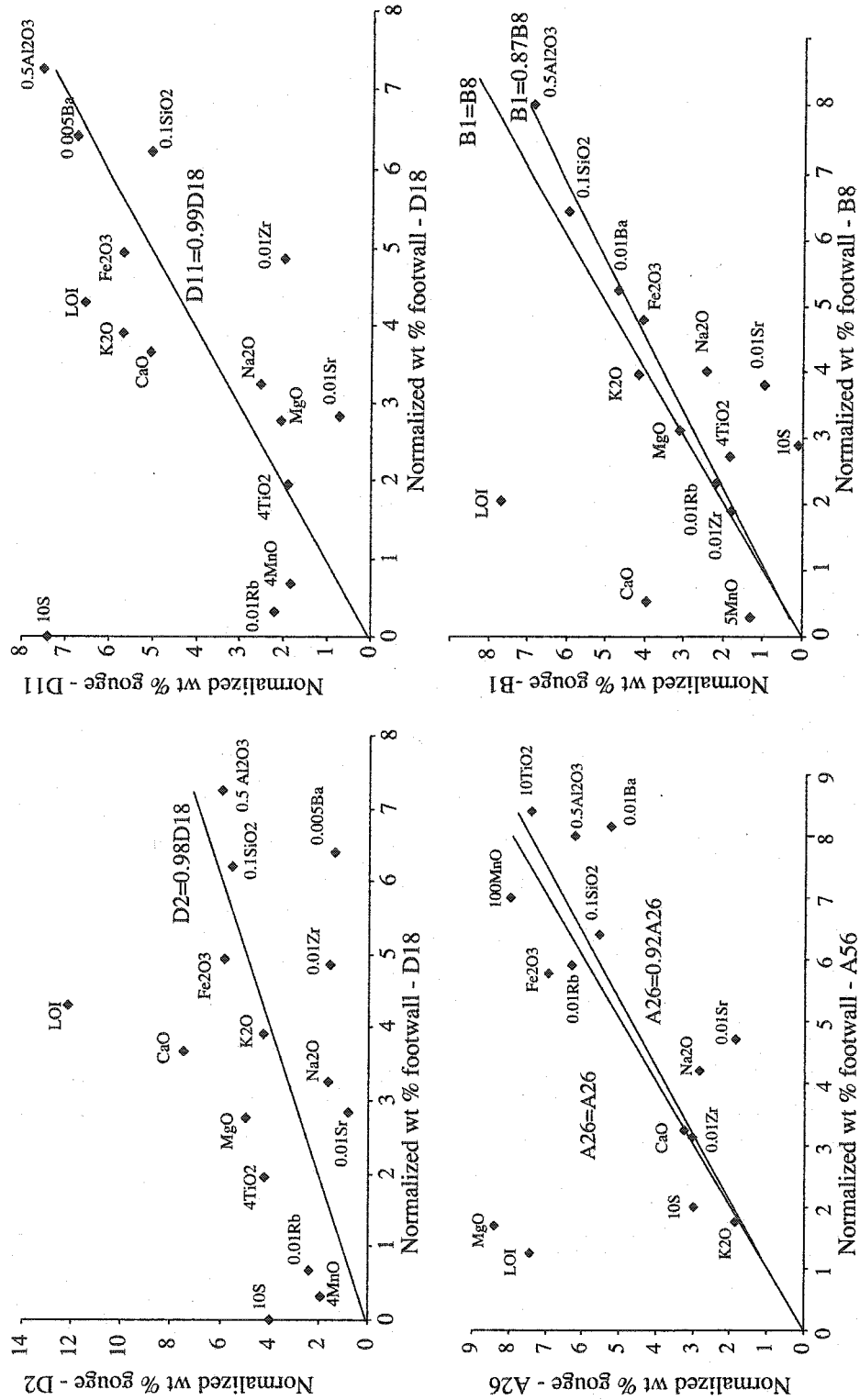
Figure 3.19. Comparison of fault and wall rock bulk composition. All samples have an isocon line with a slope close to unity, although samples A26 and B1 might have had a bulk rock change of 8-13% of the original rock composition. Noteworthy is the increase in LOI of fault rock relative to wall rock, and the dramatic enrichment of MgO in sample A26.
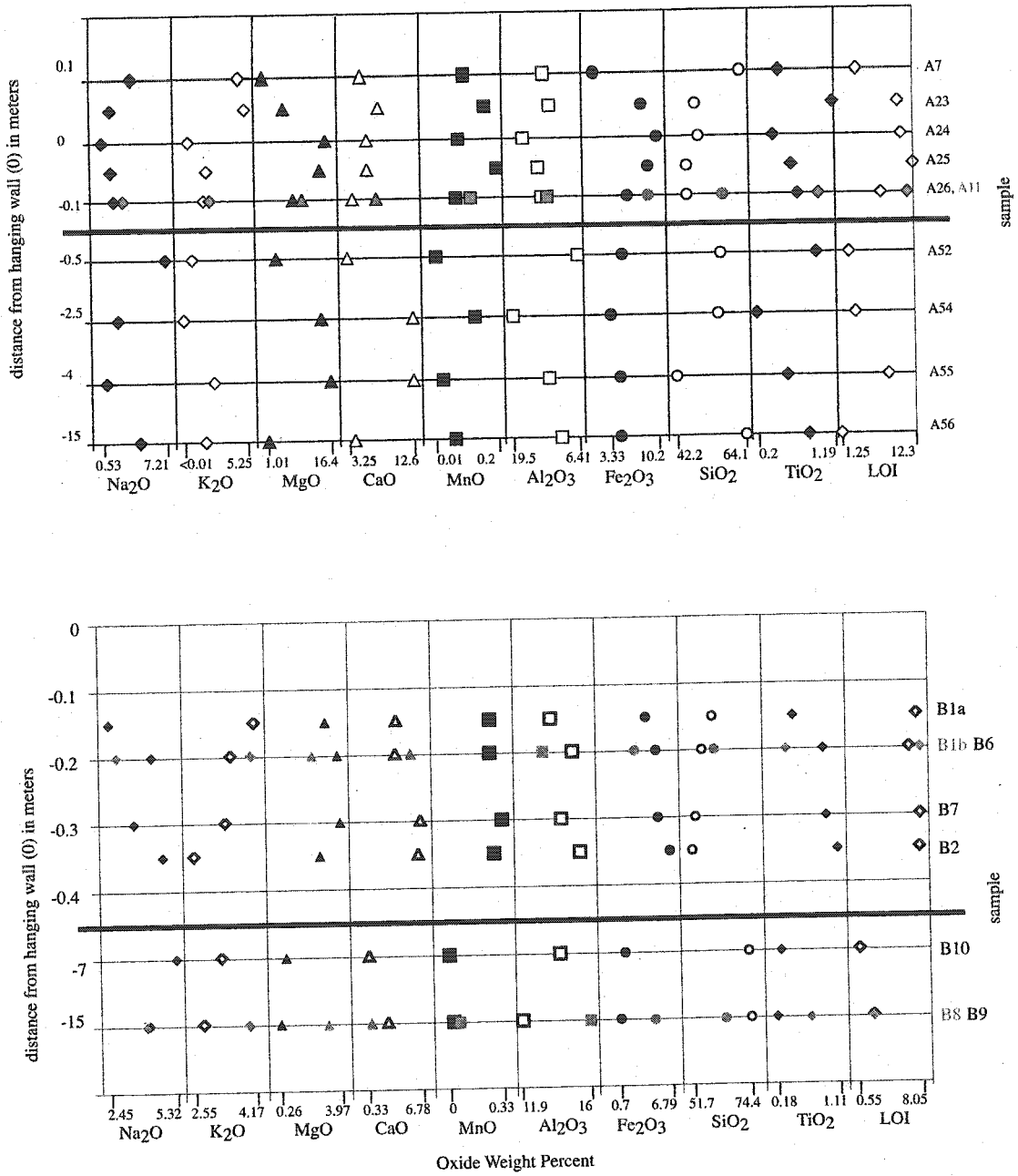
Figure 3.20. caption on following page
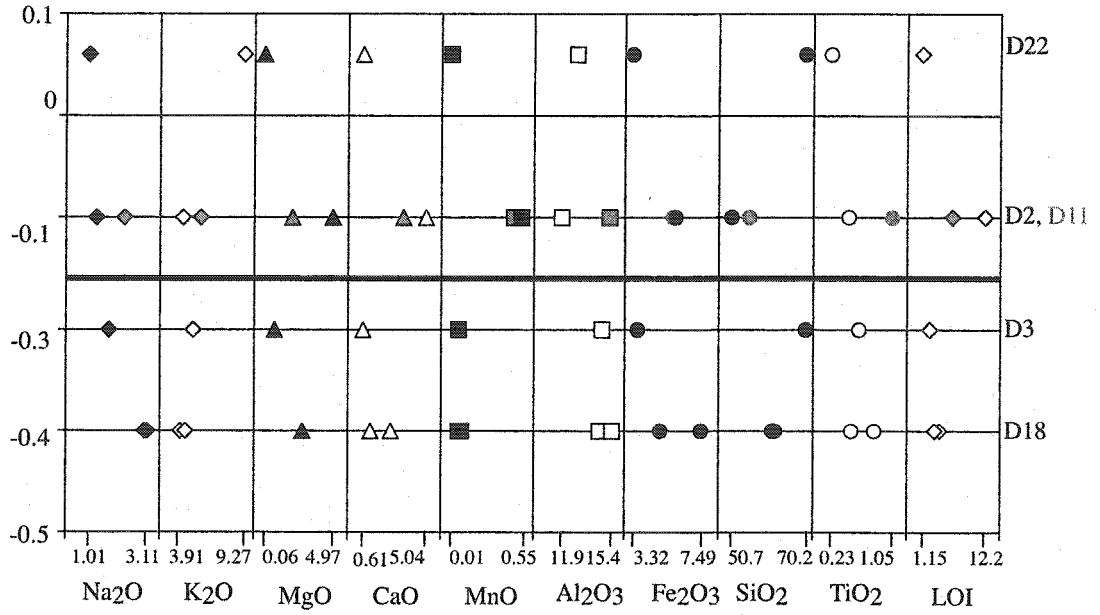
Figure 3.20. XRF transects. Note that the axis for each oxide has a different scale such that SiO2 is from 50-70 wt%, and Na2O is from 1-3 wt%, for example.

is the linear regression of the data in a diagram that compares the composition of the fault rock to its most likely parent. Deviation from a slope of unity for the isocon line indicates a change in the bulk-rock composition. Elements and oxides that do not plot on this line are enriched or depleted relative to the rest of the rock volume, and the distance they plot from the line is proportional to the amount of their change.

Because the isocon diagram relates molecular weight of the two samples, the change in mass, and therefore change in volume associated with alteration, can be studied with the isocon diagram. However, a robust analysis of volume and mass change of the bulk-rock and its individual constituents requires the demonstration that the samples are representative and accounted for, and knowledge of the reaction pathway that caused the alteration. For example, a reaction such as the feldspar-mica reaction:

$$3KAlSi_3O_8 + 2H^+ + 12H_2O = KAl_3Si_3O_{10}(OH)_2 + 6H_4SiO_{4aq} + 2K^+_{aq}$$

will result in exactly the same proportion of K^+ to Si (3:9 vs. 1:3), despite the infiltration of 12 water molecules for every 3 of reactant and a change in the activity (a, concentration corrected for its non-ideal thermodynamic behavior) of K^+ in solution. However, upon inspection it is clear that differences in the aK^+ and the pH of the solution will affect this reaction, possibly producing quartz as a product. Quartz precipitation is pressure-sensitive and prohibitively slow in the shallow crust and in the detachments quartz would more likely have been mechanically incorporated and not newly grown. Regardless of the mechanism, more quartz in the bulk rock will affect the slope of the isocon and create an apparent loss of K_2O and gain of SiO_2.

Rather than attempt to interpret the geochemical variation of the gouge and breccia relative to the wall-rock in absolute terms, the isocon diagram is used here to provide important constraints on the reaction pathway of the fault-rock evolution. The central property of the bulk-rock XRF analyses is that the geochemical system of the shear zones is conservative and controlled by the footwall, overall. Standard linear regression lines have in all cases a slope near unity for plots of the footwall samples against the finest grained gouge (Fig. 3.19). Furthermore, the major oxides and elements vary in concentration in a predictable fashion: In samples where Sr is depleted, CaO is enriched. Al_2O_3 and TiO_2, considered immobile because of their low solubility, plot close to or on the isocon. Material lost on ignition (LOI) (water, for example) plots far off the isocon. Lastly, samples enriched in chlorite have MgO that is greatly enriched relative to the less altered footwall.

The conservation of bulk rock composition across the shear zone is further supported by compositional transects across the fault zone (Fig. 3.20). The background variation in the composition of the wall rock is roughly equal to the variation in composition across the gouges and breccias of the shear zone. Furthermore, the mobile ions – ions such as K^+, Na^+, and Ca^{++} have low solubility products and readily form micas, carbonates, or other silicates depending upon temperature and composition of the solution, and are therefore considered mobile – have systematic variations across the shear zones that are consistent with reactions that produce the most voluminous alteration mineral. For example, Mormon Point exhibits an enrichment of K_2O and depletion of Na_2O from breccia sample B6 to gouge sample B1. The variation in K^+ and Na^+ (K-Na

exchange, *sensu lato*; see Giggenbach (1985) for explanation) is consistent with feldspar-
and mica-involved reactions. Badwater samples also show this K-Na exchange with the
added influence of CaO enrichment in the gouge. Chloritic Copper Canyon gouge
exhibits enrichment of MgO in the gouges relative to both footwall and hanging wall
samples. The largest variation in oxide weight percent is observed in changes of SiO_2.
SiO_2, however, is sensitive to a wide variety of chemical influences and mechanical
inheritance and therefore large variation in SiO_2 in the fault rock is not very meaningful.

Stable isotope analyses further support the conclusion that the shear zones were
more-or-less conservative with respect to geochemical changes imposed from
hypothetical fluid infiltration. Samples from all three localities exhibit a change in $\delta^{18}O$:

$$\delta^{18}O = \frac{\left(^{18}O/^{16}O\right)_{sample} - \left(^{18}O/^{16}O\right)_{SMOW}}{\left(^{18}O/^{16}O\right)_{SMOW}}$$

of less than 2ppm for all samples (Fig. 3.21). The one exception is sample A25 that has a
large depletion in $\delta^{18}O$ and an anomalous abundance of LOI, but maintains the inverse
change in concentration of MgO and major mineral forming oxides.

The stable isotope analyses measure the O from bonded OH in the clay minerals
within the gouge and breccia (Fig. 3.21; Table 3.6). Two size fractions were analyzed,
and, with the exception of clay rich Mormon Point gouge B1, the <0.2 μm fraction
exhibits a 2-4 ppm decrease in $\delta^{18}O$. The fractionation of ^{18}O relative to ^{16}O is governed
by exchange kinetics that are very sensitive not only to temperature, but the bonding
between ^{18}O and different cations in the phyllosilicate structure. The mineral-dependent
fractionation of ^{18}O with respect to ^{16}O is governed by an equation of the type:
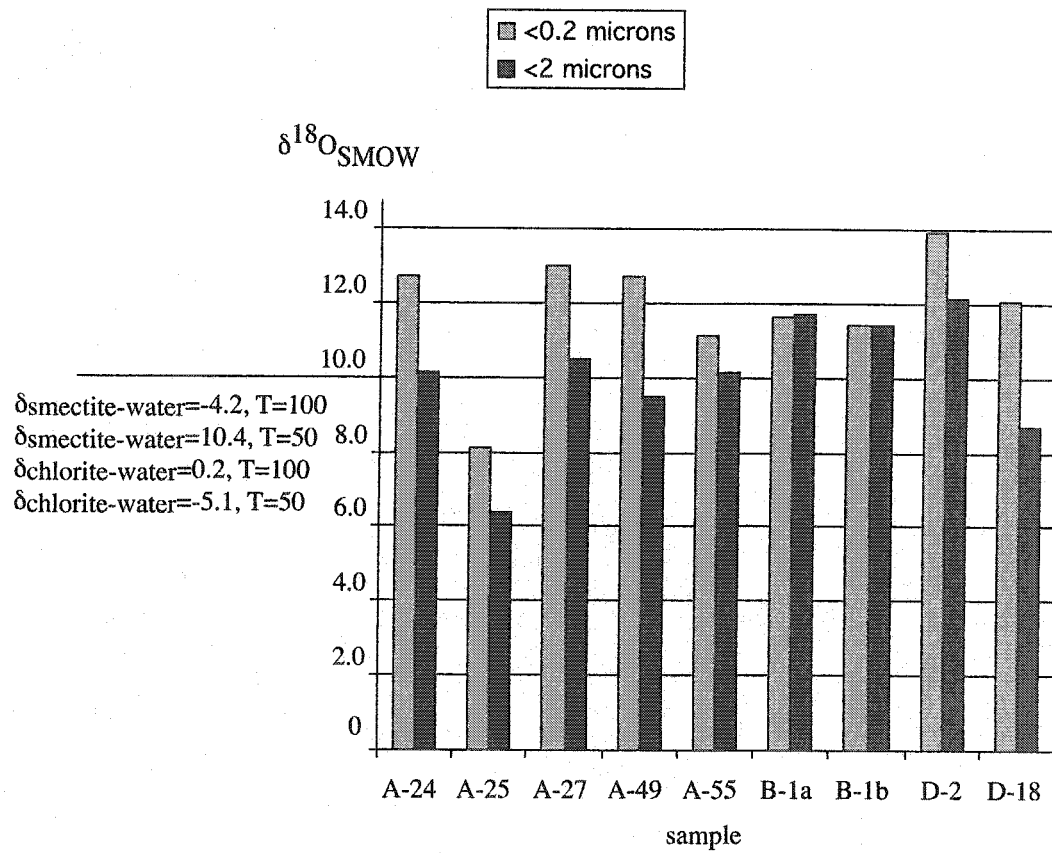
Figure 3.21. Oxygen isotope analyses of silicate separates courtesy of ExxonMobil Production Research Company. Fractionation of 18O relative to 16O is adequately explained by clay mineral fractionation (increasing in abundance in finer size fractions) of meteoric water.
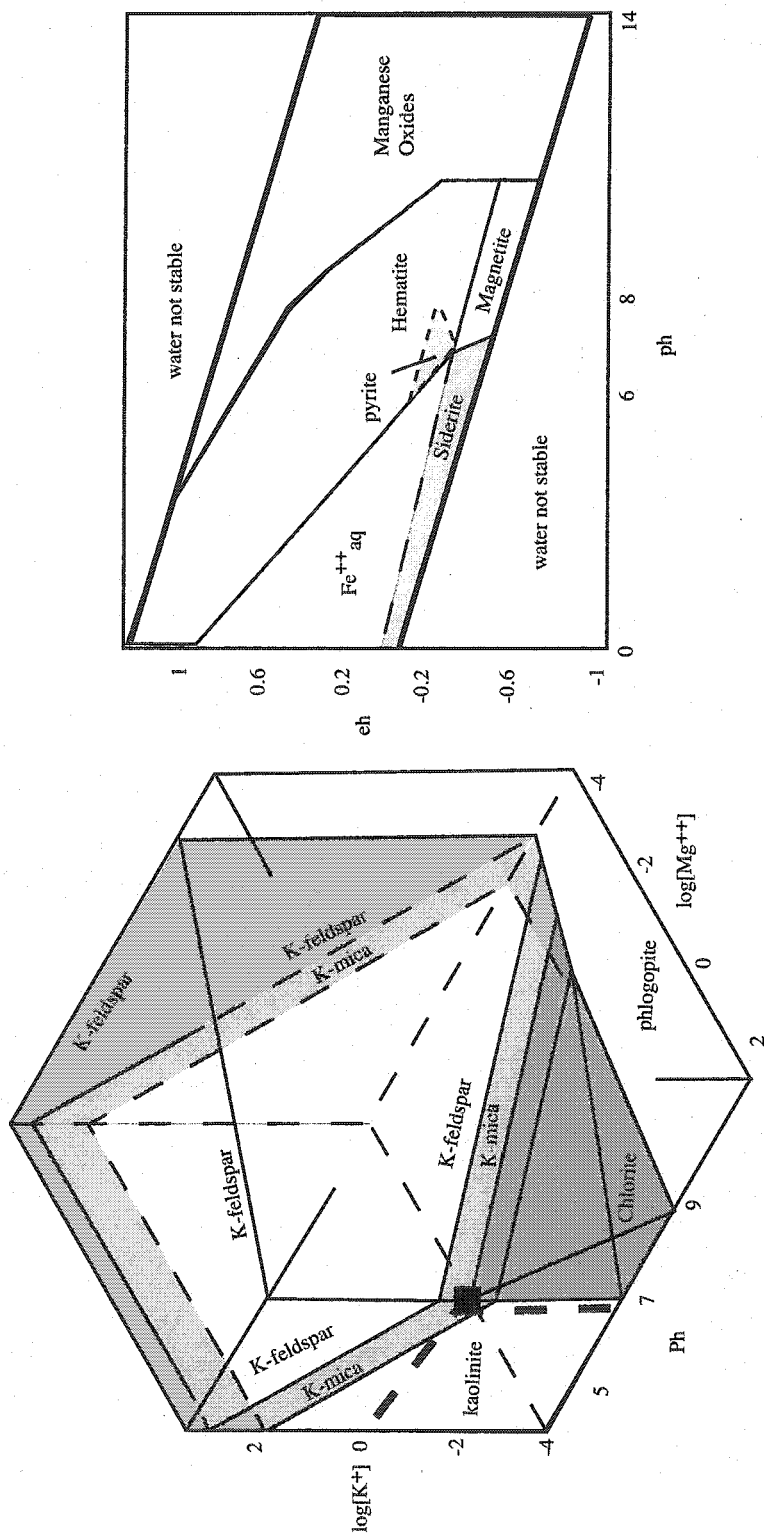
Figure 3.22. Three dimensional, symbolic stability diagram of phases stable with relative ionic concentrations in solution. From Garrels and Christ (1965). (Right) Stability diagram of phases stable with solutions of relative oxidation potential and concentration of hydrogen ions. From Chan et al. (2000) and Garrels and Christ (1965).

$$1000 \ln \alpha_{\text{phyllosilicate-water}} = A \times 10^6 T^{-2} - 4.82.$$

and

$$\alpha_{\text{phyllosilicate-water}} = \frac{\left(^{18}O/^{16}O\right)_{\text{phyllosilicate}}}{\left(^{18}O/^{16}O\right)_{\text{water}}}$$

Although A and α are ideally determined experimentally, low temperature phyllosilicates cannot be produced by reversible experiments (Essene and Peacor, 1995) and therefore reaction kinetics are determined empirically from natural basins. Using values courtesy of ExxonMobil Production Research Company, reference values of A and α for chlorite and smectite at 100° and 50°C were determined for the range of observed $\delta^{18}O$ (Fig. 3.21). Variations of greater than 4 ppm in $\delta^{18}O$ can be attributed to the larger fractionation of ^{18}O relative to ^{16}O of smectite that is observed to be more abundant at sub-micron size fractions. The size-preference of different clay minerals adequately explains the difference in $\delta^{18}O$ between size fractions. The depletion in $\delta^{18}O$ of sample A25 is also considered imposed by an excess abundance of water-bearing clay minerals.

Another interesting observation of the stable isotope data is that the mineralizing water in the detachments was meteoric. For example, water with $\delta^{18}O$ =-10.4ppm that equilibrates with smectite at 50°C will have a $\delta^{18}O$ of roughly 10ppm. Meteoric water in Death Valley should have been somewhat depleted from SMOW since late Miocene uplift of the ranges, and certainly since the uplift of the Sierra Nevada (Feng et al., 1999).

3.7. Discussion

There are two fundamental problems in our understanding of the fault rocks from the Black Mountain detachments. Firstly, how do we place the fault rocks in the tectonic context of Death Valley extension? There is evidence to support the hypothesis that the gouges and breccias developed over the last 6 Ma, are derived from the crystalline basement, but subsequently deformed via coupling with the young hanging wall. Establishing that the relationship between the fault and wall rocks requires a particular pathway over time in temperature and/or depth of the detachments requires further evaluation of the chemical and mineralogical composition of the fault rocks.

The second fundamental problem is: how do we explain the weakening of the detachments? One possible mechanism for fault weakening is for fluid pressure to approach lithostatic pressure, thereby lowering the effective stress acting on the fault (Sibson, 1992). Another mechanism for weakening is that some materials found in faults, notably hydrous phases such as clay minerals, have low values of friction (Wu, 1978; Bird, 1984; Morrow et al., 2000). Structures such as syntectonic veins, and geochemical evidence for large volume loss and deeply sourced, hydrothermal fluids are two characteristics of fault rocks used cited in support of high fluid pressure during fault slip (e.g. Manatschal, 1999; Manatschal, 2000). As noted in previous sections, the geological evidence for high fluid pressure in the Black Mountain detachments is absent. There are localities that are enriched in possibly weakening clay minerals. However, the microstructure of the fault rocks includes both localized and distributed structures, and mineralogically heterogeneous aggregates of clay-sized grains. Therefore, although

possibly applicable, neither model of changing fluid pressure or weak fault rocks fully

and satisfyingly explains the observed weakening of the Black Mountain detachments.

In the ensuing discussion I propose a simple geochemical and mineralogical

model that is most consistent with the hypothesis that the fault rocks developed during

uplift of the detachments and underlying footwall through the top few kilometers of the

crust. I then describe how the progressive comminution of the fault rocks is recorded in

the PSD and microstructure of the fault rock, each related to increasing strain and

changes in deformation mechanism over time. Given the lack of a singular mechanism

for fault weakening such as elevated fluid pressure or weak materials, I propose that the

rheological response of the fault rocks to shallow crustal conditions allowed the

continuation of fault slip and rupture propagation on the up-dip limit of the Black

Mountain detachments.

3.7.1. Water-rock interaction

The geochemical and mineralogical data from the fault rocks support the

interpretation that the gouge and breccia developed in the shallow crust as part of an

overall footwall-controlled, geochemically conservative system that was saturated with

meteoric water and not subjected to large water-rock ratios or the influx of fluids from

deeper crustal sources. Further analysis of the data resolves a record of evolving pore

fluid with the unroofing of several kilometers of sediment.

The composition of all of the rocks is roughly some mixture of feldspar, mica, and

chlorite; carbonate is ignored for the sake of this discussion. A stability diagram that

relates the concentration (denoted with "[]") of $[K^+]$ to $[H^+]$ (pH) to $[Mg^{++}]$ with SiO_2 and
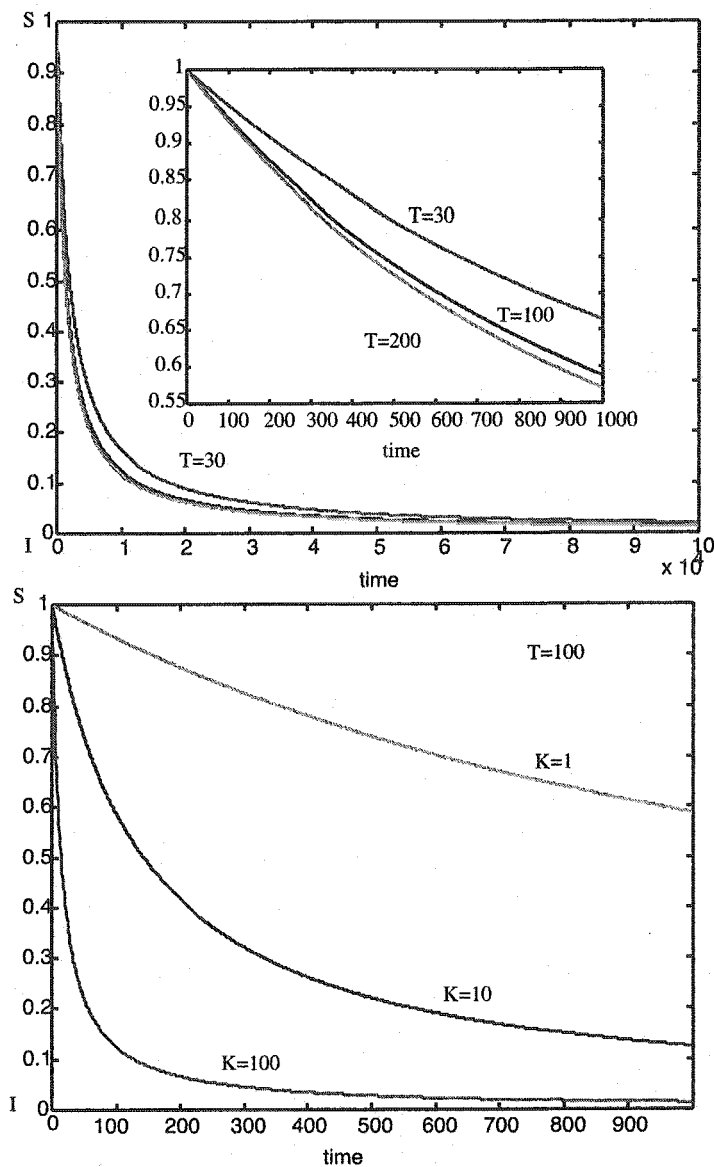
Figure 3.23. Kinetic model for the Smectite (S) to Illite (I) transition. K is the concentration of potassium in solution in moles/liter. Time is non-dimensional, but typically in hours-to-days in most experiments. At low temperature the composition of solution drives the reaction, and at low cation concentration temperature drives the reaction. The model, from Huang et al. (1996) is consistent with the fault rock clay mineralogy having nucleated at K<[10].

water in abundance would appropriately describe the geochemical system of the fault rock at equilibrium with interstitial water that can change in composition within the stability diagram (Fig. 3.22). Although it would be difficult to construct a line in this space in which trioctahedral chlorite and dioctahedral mica are at equilibrium with one another (Giggenbach, 1985), the stability field of chlorite can be juxtaposed against that of mica at a neutral pH (Garrels and Christ, 1965). The resulting triple junction of the three phases is near $[K^+] = 0.1$-1M. The proposed relationship of the three phases is consistent with more recent constructions (Helgelson et al., 1979; Giggenbach, 1985).

According to the stability diagram of the silicates, the pH was near neutral values for most of the gouge formation (pH=7-9). It is therefore noteworthy that the relative stability of siderite ($FeCO_3$) to magnetite (Fe_3O_4) is near neutral pH for typical PCO_2 of crustal waters (Fig 3.22). These two phases are present in the foliated breccia and the earliest gouges, respectively. However, manganese oxides typically found in the shallow crust are not stable at the relatively reducing conditions in which magnetite is stable. In contrast Mn-oxides observed in sedimentary environments are stable in solutions with a high oxidation potential (Eh). Therefore, water would have to become more basic or more oxidizing over time for manganese oxides and related phases to precipitate, whereas magnetite and siderite require relatively reducing conditions (Chan et al., 2000). The change in oxidation potential of the solution within the detachment towards higher Eh, and reaction progress from dominantly phyllosilicates to late oxides and minor feldspar and carbonate require an evolving fluid and/or decrease in temperature. Given the inferred conservative nature of the water-rock system within the detachments, denudation

of the fault zone is a likely mechanism for the change in the oxygen fugacity and cation activity of the fluid.

3.7.2. Illite-Smectite transition

A model for increasing oxidation potential of solution at roughly constant pH and pore fluid composition explains the development of the dominant mineral assemblages, but does not explain the evolution of swelling and non-swelling clay minerals. The abundance of swelling clay minerals is dependent upon temperature and pore-water chemistry and therefore studying the mineral transitions between swelling and non-swelling clays can support the geochemical model for fluid evolution and possibly provide additional information about the temperature of mineralization.

There has been considerable research on the mineral transition for illite and dioctohedral smectite, and this reaction is explored here rather than chlorite-involved reactions. There is some understanding of chlorite-smectite (C-S) interstratification (e.g. Roberson et al., 1999) but less so than for illite. Furthermore, the existing studies of C-S suggest that the ordered interstratified C-S is a stable phase, corrensite. The presence of corrensite suggests that the kinetics governing C-S transitions should be more complicated (i.e. second-order) than those governing illite-smectite (I-S). I-S does not have a stable intermediate phase other than different varieties of smectite that may control the development of end-member phases (Nadeau, 1999).

The I-S reaction is close to:

K-feldspar + smectite = illite + chlorite +quartz (Hower, 1976)

The I-S reaction does not require any change in pH, but does cause a change in $a\text{K}^+$ of solution, consistent with the stability diagram for the assemblage of the fault rock. However, the I-S reaction is fundamentally a kinetically limited reaction rather than an instantaneous equilibration between phases and a water of constant composition and temperature. Therefore, rather than attempt to establish a law of mass action for I-S, successful experiments of this mineral transition have established first-order rate laws that describe the time scale of the transition at different temperatures and pore fluid composition. The rate laws are consistent with changes in temperature and pressure equivalent to burial diagenesis (lithification) of basin shales (Hower, 1976; Huang et al., 1993). The rate law is approximately:

$$-\frac{dSm}{dt} = A * e^{(-Ea/RT)} * \left[K^+\right] * Sm^2$$

where Sm is the % smectite in the I/S. The activation energy (Ea) and rate constant (A) were explored by Huang et al. (1993) and field-tested against active wells in the Gulf of Mexico. Using a solution to the rate law:

$$Sm = \frac{Sm_\circ}{1 + (Sm_\circ * K * A * e^{-\frac{Ea}{RT}}) * t}$$

and the values for activation energy determined by Huang et al. (1993), the relative stability of illite-smectite can be explored for a range of temperature and [K$^+$] (Fig. 3.23). The kinetic model of Huang et al. (1993) demonstrates that either temperature or fluid composition can control the relative stability of different I-S minerals, but that at temperatures <100°C composition is very important, and at very high or low [K$^+$], temperature is very important to the reaction kinetics.

II) gouge dominates
illite-smectite, chlorite/smectite
+/- magnetite, mildly oxidizing

III) oxidizing conditions
hanging-wall faulting and
incorporation of sediment
late-to-post tectonic minerals

fault rock
reference frame
= footwall

I) initial fault rock formation
foliated breccia dominates
silicate-buffered, reducing

0 m

-2400

-4800
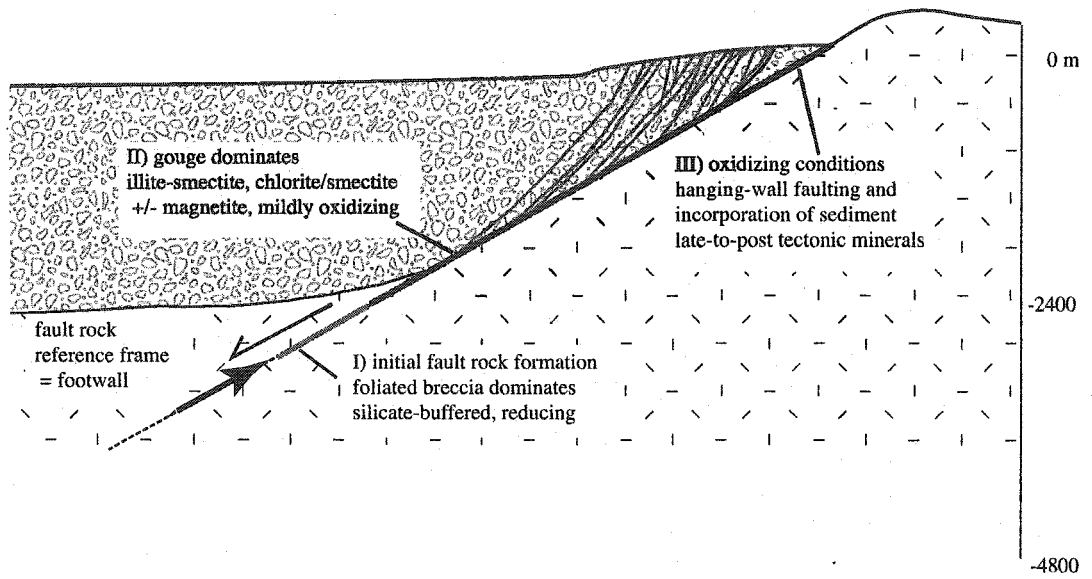
Figure 3.24. Schematic of fault rock evolution in tectonic setting.

In the Death Valley fault rocks there are both chloritic and illitic phases and according to both the kinetic model and the equilibrium model [K$^+$] is in the range of 0.1-10 for most localities. For this restricted range of [K$^+$], temperature would have controlled the abundance of swelling clay. Furthermore, the presence of highly crystalline 2M illite is evidence that the highest temperatures of mineralization during fault-rock development were >100°C, and possibly much higher. However, some of the illite has a swelling component, albeit nowhere >20% smectite, and therefore the temperature of mineralization was <100°C for much of the fault-rock development.

I-S minerals are the dominant phyllosilicate in the Badwater and Mormon Point detachments. In Copper Canyon the dominant swelling clay in much of the fault rock is a swelling chlorite. The C-S found in the Copper Canyon detachment is considered to be a product of the alteration of basaltic rocks. Research in basalts elsewhere has resulted in a model that fluid flow can stabilize corrensite, whereas high temperatures favor less smectitic (or saponitic; saponite is the tri-octahedral smectite) varieties (e.g. Schmidt et al., 1997). Therefore, the reaction kinetics that govern the I-S transition also likely apply to the C-S minerals and their relationship to [Mg^{++}] and temperature.

The development of the clay minerals in the fault rocks required temperatures >100°C, and temperatures <100°C. While it cannot be ruled out that some of the high temperature phases were mechanically inherited from the wall rocks, only some wall rock units have abundant chlorite or mica, and where present the phases are >10μm and highly crystalline. In contrast, poorly crystalline ultra-fine grains of clay minerals are abundant in the fault rock. The I-S and C-S changes could not have taken place via solid-state

reactions because the fault rocks developed in an environment of decreasing temperature and increasing abundance of swelling clay. Most of the swelling clays must have precipitated in pore spaces from solution, perhaps epitaxially on earlier grains. The retrograde pathway of the I-S and C-S transition in the detachments is the inverse of most time-temperature pathways for clay minerals. The implication of the models for geochemical and mineralogical evolution of the fault rocks is that the earliest phases grew at >3 km depth, and later phases grew near the surface of the earth, assuming a geothermal gradient of 30°C/km (Fig.3.24) (Sass et al., 1994).

There is an established semi-quantitative relationship between fluid pressure and swelling clay mineralization wherein increasing swelling clays should correspond to decreasing fluid pressure (Hower, 1976; Bird, 1984). However, swelling clays have low μ_{eff} (Wu, 1978; Bird, 1984), and a propensity for frictionally stable sliding (Morrow et al., 2000). Therefore, the increase in the abundance of hydrous clay minerals should decrease the strength of the detachment and the propensity for seismic rupture. In other words, any decrease in fluid pressure via hydration reactions should be counter-balanced by weakening of the material via the presence of hydrated minerals. Such a feedback between aqueous solutions and hydrous clays may play a role in the weakening of the Black Mountain detachments. However, the discussion of the microstructure of the fault rock in the following section suggests that neither mechanism for weakening operates as a singular process, but rather is accompanied by a changing rheologic response with increasingly shallower crustal levels of strain accumulation.

3.7.3. Deformational history

Comminution, slip localization, cataclastic flow, and granular flow are appropriate terms to describe the deformation mechanisms that operated/operate within the fault rocks. Comminution is the general process of grain-size reduction through fracture and abrasion. The most quantitative measure of this grain-size reduction is particle size distribution. A power-law exponent, D, describes the PSD of the different fault rocks. The experiments of Marone and Scholz (1989) empirically confirm that increasing D is correlated with increasing shear strain. The probabilistic analysis of Sammis et al. (1987) is an intuitive and semi-quantitative way to relate shear strain (ε_{12}) to D. The relationship between D and ε_{12} via an efficiency term that relates the amount of strain per fracture (β):

(2) $\varepsilon_{12} = 3\beta/2(1-2^{D-3})$

Sammis et al. (1987) recommended that $\beta=17$ as an upper value to described comminution and a component of cataclastic flow. The range in PSD of the fault rock demonstrates that the probabilistic relationship between shear strain and fractal dimension does not strictly apply to the detachment fault rocks because there is no real solution for D=3, an observed threshold value between breccia and gouge. Nonetheless, shear strains just greater than 100 are required for D=2.6. Shear strains >>100 are also predicted by a kinematic model based upon the microfabric of the fault rock (Chapter 2; Cladouhos, 1999b). A more sophisticated model of comminution is required to further explore the significance of larger dimensions of PSD.

Fault rocks such as breccia develop via cataclastic flow wherein fracture accompanied the rolling and sliding of grains past one another. Gouge, on the other hand, is not strictly speaking a cataclastic rock as grain fracture did not accompany flow. Transgranular fracture in gouge predates the rotation and translation of grains into their preferred orientation and, despite the fine grain size, abrasion of grain boundaries is still texturally evident. Alternative models of deformation of gouge are that they are either entirely frictional or completely fluid. Gouges from other localities have been explained as the product of comminution but relatively little grain rotation and translation (Chester and Logan, 1987; Chester and Chester, 1998). At the other extreme, gouges have been described as behaving in a completely fluid manner wherein grains are able to either rotate, or rotate and translate completely freely within the flow field (Otsuki et al., 2003). In this latter case the gouge is either truly a fluid or else comprises clasts passively rotating within a viscous or plastic matrix (Oertel, 1985).

I propose that *granular flow* aptly describes gouge development. The dynamic definition of granular flow is: inelastic grain interaction wherein the agitation energy intrinsic to rotation and translation is larger than thermal effects (Wolf, 1998). Granular dynamics is different from its theoretical predecessors dealing with gases because of the inelasticity of particle interaction. The inelasticity of granular flow is because of frictional process where the movement of grains requires overcoming the effective friction of grain-on-grain contacts. In turn, the primary difference between cataclastic and granular flow is that cataclastic flow is limited by the resistance of the grains to fracture (strength) and not only by the frictional contacts.

In rock mechanics experiments localized structures develop in analog gouges in response to unstable slip (Marone and Scholz, 1990; Beeler et al., 1996). By analogy, localized structures in the Black Mountain detachments may be the expression of unstable slip such as must have occurred during the earthquakes that produced the scarps on the valley floor. It is therefore noteworthy that the localized slip planes are not crosscut by the surrounding microfabric and in turn have been suggested to be the irreversible product of a shear strain gradient across the detachment (Cowan et al., 2003). If correct, the interpretation of the localized structures as partitioning frictionally unstable slip requires that the distributed deformation across the gouge and breccia is accommodated by frictionally stable slip on the detachments. In turn, the deformation of the gouge and breccia partly determines stable and unstable configurations of the Coulomb wedge, the dynamics of which evolve over geologic time. Given the two dominant deformation mechanisms that are operative in the fault rocks, cataclastic and granular flow, it is further reasonable to propose that the change in deformation mechanism as the detachment approaches the surface of the earth contributes to the weakness and dynamic behavior of the detachments. Unfortunately, further tests of the hypotheses presented here are difficult to formulate given the propensity of fault zones to record both high and low rates deformation (e.g. Cowan, 1999). Nonetheless, by proposing these hypotheses that are inspired by natural data, new avenues of investigation have been opened, and our understanding of the Death Valley detachments has been significantly advanced.

3.8. Conclusion

The Black Mountain detachments have been slipping as a moderately weakened, low-angle fault with subsidiary structures for the last 6 Ma. During this time they have cooperated in both seismic and aseismic slip, controlled the structural style of range-front extension, and provided several millimeters-per-year extension of sedimentary basins and the modern valley. Within the detachments are breccia and gouge with a distribution and structure indicating that they developed over time through deformation that was isolated from, and possibly older than, the overlying sediment. However, distributed deformation continued until more recent time when deformation within the gouge and breccia was coupled with the present-day hanging wall. Analyses of the gouge and breccia demonstrate that they are derived primarily from the footwall crystalline rocks and also contain several sets of authigenic minerals. The authigenic minerals preserve a record of limited interaction between meteoric, neutral water and the footwall. The mineralizing water became more oxidized through the history of the detachment and clay mineral authigenesis required decreasing temperatures at constant ionic concentrations within the solution. The fault rocks therefore belong to the footwall reference frame and were uplifted through the top few kilometers of the crust over the last few million years. The microstructure of the fault rocks is typified by cataclastic and granular textures with fabrics that developed after shear strains >>100 were accrued. Given the lack of evidence for a singular mechanism of fault weakening, such as elevated fluid pressure or concentration of low-friction minerals, a reasonable suggestion is that the different

rheological responses manifest in cataclastic, granular, and localized textures essentially

function as a mechanism for fault weakening and slip instability.

Table 3.1. Sample key from Black Mountains. Position is relative to the contact between fault rock and hanging wall, and coordinates are in UTM (approximated).

Sample	Rock type	note	position
Basalt Ramp, 3997900, 524000			
CC-94	scaly clay gouge	Type sample	-0.2
A-1	breccia & gouge	hanging-wall related	2
A-3	breccia		0
A-4	granular gouge	hanging-wall related	1
A-5	granular gouge	hanging-wall related	1
A-28	griable andesite		0.2 to 0.1
A-29	granular gouge	green, banded	0.2 to 0.1
A-30	gneiss	footwall	-1
A-31a	Pegmatite	cataclasite	-0.4
A-31b	breccia	basalt	-0.5
A-32	breccia	basalt with clay matrix	-0.3
A-33	gouge	foliated, red, clay-rich	0
A-34	granular gouge	hanging-wall related	0.3
A-35	crystalline rock	cataclasite	0
A-36	foliated breccia	green clay, basalt layers	-0.3
A-37	sclay clay gouge	on hanging-wall faults	1
A-38	conglomerate	hanging wall	1
A-39	Basalt		-1
A-59	basalt	top of dike (at A1-A5)	-0.4
A-60	basalt	middle of dike	-0.7
A-61	basalt	bottom of dike	-1
A-62	gneiss	mountain front	-10
A-63	gouge	float gouge	
A-67	cataclasite/phyllonite	footwall near basalt ramp	
A-68	cataclasite/phyllonite	footwall near basalt ramp	
A-70	cataclasite/phyllonite	footwall shear zone	
A-77	cataclasite/phyllonite	under basaltic sill	
A-78	gneiss	footwall	
Lunch Pass, 399800, 525000			
A-6	granular gouge		
A-7	conglomerate	hanging-wall related	-0.1
A-8	granular gouge		0.1
A-71	clay gouge	lunch pass	-0.3
A-72	clay gouge	lunch pass	
A-73	tephra	tephra	
A-74	breccia	lunch pass	
A-75	clay gouge	lunch pass	
A-76	breccia	lunch pass	
Lower Corrugations, 3997600, 523500			
A-9	foliated breccia	green with red coating on fractures	
A-10	clay gouge	brick red, from injection	-0.2
A-20	gouge	"baked"	0 to -0.05
A-21	conglomerate	hanging wall	0.1 to 0
A-22	gneiss	footwall	0.2 to 0.1
A-23	clay gouge	injection above fault surface	>-15
A-24	clay gouge	brick red, from fault surface	0.05
A-25	clay gouge	brown, with FW-derived clasts	0
A-26	clay gouge	brown & green	-0.02 to -0.04

Table 3.1. Continued

Sample	Rock type	note	position
A-27	breccia	green, derived from footwall	-0.1 to -0.15
A-52	breccia	Friable, green, footwall-derived	-0.1 to -0.15
A-53	breccia	Pale green to white, "crush"	-0.5
A-54	breccia	Pale green, friable	-1
A-55	diorite	Partly chloritized	-2.5
A-56	gneiss	mylonite	-4
A-57	Felsic	intrusive	>-15
A-58	dolomite	boudin	>-15
Range Front, 3997400,523500			
A-11	clay gouge	same as CC-94	
A-12	slip plane	between fault rock and hanging wall	0 to -0.1
A-13-1	clay gouge	foliated, survivor grains	0.1 to -0.1
A-13-2	conglomerate	hanging wall, connects with A13-1	0 to -0.1
A-69	basalt	dike margin in Sheep Canyon	0.1 t 0
Upper Copper Canyon, 3997500,526000			
A-23	vein	in footwall	>-15
A-40a,b	gouge	hanging wall, volcanic clasts	-0.2
A-40c,d	hanging wall	adjacent to A40, a,b	0.3
A-40e	gneiss	footwall	>-5
A-41	breccia	Green and red, fractured	-0.2
A-42	clay gouge	white	-0.1
A-43	breccia	hanging wall	1
Upper Corrugations, 3998000,525000			
A-44	breccia	green, relatively undeformed	-0.4
A-45	breccia	green & red	-0.35
A-46	clay gouge	foliated, brick red	-0.05
A-47	clay gouge	unfoliated, near hanging wall	0
A-48	foliated breccia	foliation	-0.05
A-49	breccia	red veins in green rock	-0.4
A-50	clay gouge	in hanging wall	0.1
A-51	conglomerate	hanging wall	0.5
Melange Pedastel, Mormon Wash, 3989300, 522000			
B-1a	clay gouge	green-yellow flow banding	-0.15 to -0.2
B-1b	clay gouge	no color banding	-0.20 to -0.25
B-2	granular gouge	coarse grained, color banded, Riedels	-0.30 to -0.35
B-3	granular gouge	coarse grained with Riedels	-0.3 to -0.3 ?
B-4	footwall		>-10
B-5	footwall		>-10
B-6	granular gouge	color banding at ying-yang clast	-0.1 to -0.3
B-7	gouge	color banding	-0.3 to -0.4
B-8	gneiss	fracutred, slightly altered	-15
B-9	pegmatite	footwall	-15
B-10	footwall	bleached	-7
B-11	cataclasite	matrix from melange	-2
B-29	footwall		
B-29	footwall		
B-30	footwall	shear zone	
B-31	footwall	shear zone	
B-32	slickenside		

Table 3.1. Continued

Sample	Rock type	note	position
East Branch, Mormon Wash			
B-12	granular gouge	color banding with P, R	-0.5
B-13	granular gouge		-0.2
B-14	gouge/breccia	hanging wall inclusions	0 to -0.1
B-15	slip surface	contact between hanging wall & gouge	0.1 to 0
Mormon Wash, detachment, 3988700, 523000			
B-16	footwall		
B-17	breccia		
B-18	foliated breccia		
B-20	foliated breccia		
B-21	hanging wall		
B-21	hanging wall		
B-22	gouge		0 to 10 cm
B-23	gouge		10 to 20 cm
B-24	breccia		20 to 40 cm
B-24	breccia		20 to 40 cm
B-25	breccia		20 to 40 cm
B-26	breccia		20 to 40 cm
B-27+28	hw-fault	upper plate fault	
Willow Wash, 3989600, 524800			
B33	clay gouge	similar to Copper Canyon gouge	
B34	clay gouge		
Size 36 Canyon, 3981550, 526000			
C-1	clay gouge		0 to -0.1
C-2	breccia	footwall	-1
C-3	granular gouge		-0.2
C-4	metamorphic	footwall	-1
C-5	metamorphic	footwall	>-1
C-6a	clay gouge		-0.2 ?
C-6d	granular gouge		-0.2 ?
C-7	metamorphic	footwall	-20
C-8	granular gouge	red and white banding	-0.2
West Mormon Point, 3989600, 524800			
B-35	breccia	pegmatite	
B-36	breccia	pegmatite	
B-99a	breccia	mixed pegmatite and dolomite	
C-9	slip surface		0
C-10	cataclasite	footwall	0
C-11	cataclasite		0
C-12	cataclasite		0
C-13	granular gouge	flow banded	0 to -0.2
C-14a,b	gouge/breccia	hanging wall	0 to -0.2
C-15	gouge/breccia	hanging wall	0 to -0.2
C-16	gouge/breccia	Unstructured olive-green matrix	0
C-18-20	footwall	altered	
C-23+C24	hanging wall	with gouge	
C-25	hanging wall		
C-26	hanging wall	lens in fault zone	
C-27	clay gouge		
C-28	foliated breccia	foliated breccia	

Table 3.1. Continued

Sample	Rock type	note	position
Elf Canyon, 4014000, 521000			
D-2	gouge	flow-banded	0 to -0.1
D-3	gouge	color banding, crushed boudins	-0.2 to -0.3
D-4	gouge		0 to -0.3
D-5	hanging wall		0.1 to 0
D-6	breccia	footwall	>-0.5
D-7	pegmatite	footwall	>-1
D-8	gneiss	footwall	>-1
D-23	breccia/gouge	tabular layers	0 to -0.03
D-24	breccia/gouge	tabular layers	0 to -0.02
D-25	slip surface	gypsum vein on surface	0
D-26	gouge	manganese weathering/alteration	-0.5
D-42		elf	
Wide Canyon, 4012500, 520600			
D-9	clay gouge		-0.1
D-10	breccia		-0.2 to -0.4
D-11	gouge		-0.1
D-12	breccia		-0.5 to 0.7
D-13	breccia		-1
D-17	granular gouge	cataclasite with P-folia	0
D-18	breccia	crushed breccia	-0.4
D-19	hanigng wall	volcanics	0.5
D-20	gneiss	mylonitic footwall	>10
Green Canyon, 4012500, 520600			
D-1	hanging wall	hanging-wall fault	>10
D-14	slip surface		0 to -0.2
D-15a	hanging wall		+0.1 to 0
D-15b	footwall		0 to -0.3
D-16			+0.1
D-21	hanging wall	dark, red alteration	0.04
D-22			0.06
Natural bridges and surrounding, 4015300, 52100			
D-30	gouge	with gypsum	
D-31	footwall	FW carbonate	
D-32	gouge		
D-33	gouge		
D-34	gouge		
D-35	gouge		
D-36	gouge	hanging wall related	
D-37	gouge	hanging wall related	
D-38	hanging wall		
D-39	footwall		
D-40			
D-41		south of natural bridge canyon	
D-43		south of natural bridge canyon	

Table 3.2. Footwall brittle structures

Sheep Canyon				Badwater			
Structure				footwall fault	352	65	W
fault	352	65	W	fracture	345	88	W
fracture	345	88	W	vein	350	75	W
vein	350	75	W	gouge zone	340	32	W
dike	85	85	S	fracture	340	70	W
dike	335	40	S	cleavage	350	60	W
fault	330	75	E	cleavage	344	40	W
fault	0	80	E	cleavage	310	65	W
chloritic margin	350	60	W	cleavage	325	50	W
joints	80	70	S	dike	0	90	
joints	325	90		fracture in dolomite	65	70	E
fault	295	70	N	fracture in dolomite	310	50	W
mylonite	15	60	W	fracture in dolomite	345	35	W
				mylonitic shear zone	315	25	W
				fracutre in limestone	300	20	W
Copper Canyon - 1				cleavage in limestone	315	60	W
cleavage in dolostone	340	20	E	cleavage in limestone	340	70	W
cleavage in dolostone	345	30	E	cleavage in limestone	350	60	W
bedding	330	30	W	above dike	330	40	W
spaced cleavage	295	90		clay fracture	65	70	E
spaced cleavage	320	70	W	clay fracture	310	50	W
layering along fold	0	90		clay fracture	345	35	W
layering along fold	340	70	E	clay fracture	315	25	W
layering along fold	325	70	E	gneissic foliation	330	30	E
joints in dolomite	300	70	E				
joints in dolomite	330	75	W	**Size 36**			
dike margin	340	70	E	clay-filled fracture	40	70	W
dike margin	325	80	W	footwall shear zone	340	40	W
Copper Canyon - 2				**Mormon Point**			
shear zone in dolomite	305	15	S	cleavage in dolomite	35	90	
entrance fault	0	89	W	cleavage in dolomite	350	65	W
entrance fault	348	60	W	cleavage in dolomite	310	20	W
carbonate veins	80	64	N	cleavage in dolomite	40	50	W
faults in gneiss	350	30	W	cleavage in dolomite	5	30	E
faults in gneiss	350	35	E	cleavage in dolomite	15	90	
joints/clvg	300	30	S	cleavage in dolomite	305	70	E
joints/clvg	310	60	S	cleavage in dolomite	305	70	W
slaty sections	350	10	N	cleavage in dolomite	295	75	E
slaty sections	310	50	E	"mound" structure	20	30	W

Table 3.2. Continued

Copper Canyon - 2			
slaty sections	0	89	W
gneissic foliation	280	15	N
gneissic foliation	335	35	E
cleavage	50	65	W
cleavage	340	75	E
faults	35	80	W
faults	20	70	E
basalt ramp cleavage	20	25	W
crenulation cleavage	335	52	W
footwall shear zone	20	45	W

Table 3.3. Grain counts of five samples

Grain	%		
B2		A11	
Quartz+Plagioclase	91	quartz	35
carbonate	5	dolomite	60
Clay, Rock Fragments, and Opaque	4	opaque, carbonate, gouge	5
D4		B1	
Schist	71	Schist	15
Quartz	19	Carbonate	15
Clay, Gouge, Fe-stain	11	Quartz + Plagioclase	70
D2		D11	
Quartz mylonite	67	Rock fragments, basalt	11
Carbonate	28	clay	14
Opaque, clay, and other	5	quartz and other	75

Table 3.4 XRF analyses, University of Washington, 2003. Major oxides only.

		SiO2	Al2O3	TiO2	FeO	MnO	CaO	MgO	K2O	Na2O	P2O5	Total	LOI(%)
A-11	wr	47.89	15.23	1.045	7.56	0.152	9.25	11.59	2.64	3.47	0.286	99.11	13.30
A-11	<63	48.86	15.90	1.122	8.22	0.100	6.71	12.66	2.67	2.62	0.372	99.23	12.29
A-11	<2	46.14	16.06	1.207	9.71	0.088	5.03	16.30	2.19	1.81	0.320	98.85	11.66
B-1	<63	61.40	17.77	0.579	2.92	0.153	4.54	3.58	5.52	2.86	0.188	99.51	8.37
B-2	wr	52.10	16.70	0.937	3.88	0.369	10.92	6.09	3.49	4.13	0.272	98.89	14.44
B-2	<63	51.49	18.19	1.490	3.93	0.361	9.65	5.92	4.18	3.22	0.420	98.85	13.95
B-16	wr	49.42	16.50	0.691	7.26	0.238	10.14	8.40	2.91	3.30	0.131	98.99	8.83
B-16	<63	38.88	16.03	1.332	15.07	0.425	4.04	18.05	1.14	0.91	0.166	96.04	10.89
B-21	wr	65.19	15.39	0.510	3.03	0.251	4.56	2.92	4.81	2.63	0.165	99.46	7.22
B-21	<63	53.39	15.33	1.006	5.66	1.154	8.91	3.84	4.82	2.15	0.285	96.54	9.36
B-22	wr	60.28	17.13	1.167	5.36	0.249	2.88	3.71	4.02	4.09	0.388	99.27	3.98
B-22	<63	53.95	16.97	1.605	8.31	0.186	3.63	5.75	4.16	3.01	0.550	98.12	5.82
B-24	<63	42.55	16.90	1.121	14.94	0.447	3.01	16.94	1.39	1.47	0.287	99.06	8.67
B-25	wr	50.44	18.25	0.783	6.51	0.256	7.25	8.44	2.91	3.95	0.167	98.96	8.75
B-25	<63	44.24	16.83	1.167	10.81	0.315	7.56	13.00	2.76	1.67	0.234	98.59	11.28
B-34	<63	52.95	19.17	1.998	7.57	0.158	4.91	4.69	2.43	4.40	0.899	99.18	7.39
D-2	wr	52.16	12.87	0.572	5.40	0.412	10.09	6.49	5.91	3.74	0.179	97.82	16.08
D-2	<63	58.78	16.18	0.661	4.18	0.093	4.92	4.06	5.88	3.55	0.205	98.51	10.16
D-3	wr	66.71	13.37	0.420	2.81	0.130	0.54	0.75	4.03	7.66	0.093	96.52	4.06
D-3	<63	61.86	19.46	0.999	5.67	0.082	0.84	1.67	6.40	2.37	0.161	99.51	4.00
D-5	wr	61.22	12.89	0.281	3.72	0.039	11.00	0.96	6.42	2.52	0.098	99.15	8.62
D-5	<63	49.31	13.07	0.464	5.21	0.111	14.26	4.42	4.15	4.42	1.416	96.83	14.02
D-8	wr	71.57	12.51	0.660	4.79	0.144	3.66	1.15	3.40	1.43	0.037	99.35	4.54
D-9	wr	58.73	16.33	1.036	5.56	0.170	5.76	3.10	4.45	3.40	0.306	98.84	7.52
D-9	<63	60.63	21.07	0.905	3.31	0.047	1.46	2.09	7.35	2.57	0.290	99.72	4.86
D-29	wr	63.90	16.20	0.494	3.31	0.108	3.13	2.40	4.29	4.75	0.154	98.74	5.66
D-29	<63	61.59	22.17	1.135	3.30	0.018	0.54	1.65	7.21	2.03	0.287	99.93	3.56
C-8	<63	66.01	14.05	0.727	3.90	0.077	5.19	1.09	5.59	2.01	0.162	98.80	7.69
CC	<63	25.59	12.82	0.812	6.81	0.051	3.43	13.24	0.43	19.80	0.077	83.06	12.95
WW6	<63	56.00	17.58	0.891	5.98	0.091	1.22	8.89	6.24	1.76	0.252	98.91	7.48

Table 3.5. XRF analyses courtesy of Peter Vrolijk. Major Oxides only.

PLUG #	NA2O %	MGO %	AL2O3 %	SIO2 %	P2O5 %	K2O %	CAO %	TIO2 %	CR2O3 %	MNO %	FE2O3 %	LOI %	SUM %
A1	0.98	1.16	14.30	52.2	0.41	9.48	5.96	1.260	0.04	0.13	7.25	5.30	98.6
A3	4.54	5.29	16.50	48.1	0.48	3.06	4.95	1.440	<.01	0.18	8.26	5.70	98.7
A4	1.34	1.55	13.80	59.6	0.23	7.74	3.77	0.799	0.03	0.08	4.34	4.25	97.7
A5	1.26	1.73	14.20	58.8	0.23	8.11	4.08	0.767	<.01	0.08	4.83	4.60	98.8
A6-g	1.18	8.77	10.90	46.5	0.17	3.91	7.95	0.699	<.01	0.62	5.61	14.00	100.4
A6-r	1.07	9.34	10.30	45.8	0.16	3.57	8.32	0.680	<.01	0.77	5.39	14.80	100.3
A7	3.79	1.01	13.10	63.0	0.13	4.68	4.84	0.517	0.05	0.11	3.33	3.90	98.6
A9	2.61	9.19	13.00	51.6	0.18	2.74	3.44	0.760	0.01	0.07	8.03	6.90	98.6
A10	0.48	9.56	9.88	42.9	0.18	2.15	10.90	0.657	<.01	0.08	12.00	11.10	100.0
A11	1.74	10.60	13.40	42.4	0.25	2.38	7.18	0.989	0.02	0.12	9.13	11.60	99.9
A13-1	1.86	3.32	13.90	55.3	0.27	6.87	4.70	0.842	0.03	0.05	5.76	5.70	98.8
A13-2	3.89	1.63	13.20	59.5	0.17	3.53	5.78	0.623	0.05	0.12	4.42	5.55	98.6
A21	4.15	0.65	14.10	67.5	0.13	5.62	2.40	0.439	0.11	0.04	2.67	2.25	100.2
A23	1.41	6.22	14.20	45.8	0.35	5.25	7.39	1.190	0.03	0.17	8.47	10.10	100.7
A24	0.53	16.40	8.57	46.7	0.12	0.68	5.71	0.441	0.16	0.09	10.10	10.70	100.2
A25	1.48	14.80	11.40	42.2	0.16	2.04	5.71	0.670	0.02	0.20	9.17	12.30	100.2
A26	2.85	8.39	12.50	55.7	0.15	1.87	3.25	0.744	0.13	0.08	6.96	7.45	100.2
A27	3.64	10.40	14.80	52.9	0.07	0.13	6.91	0.287	0.04	0.01	5.84	5.25	100.4
A45	3.77	6.76	14.50	49.9	0.10	0.28	9.36	0.625	0.23	0.05	8.93	4.00	98.6
A47	2.09	3.51	14.40	49.2	0.33	6.19	7.96	1.090	0.04	0.13	6.54	8.65	100.3
A49	0.88	13.30	11.70	45.8	0.15	0.33	9.52	0.301	0.03	0.05	10.50	7.50	100.2
A51	3.49	0.89	14.30	65.6	0.16	6.28	2.50	0.510	0.09	0.04	3.20	2.25	99.5
A52	7.21	3.62	19.50	55.2	0.34	0.92	2.37	0.948	0.04	0.02	6.15	2.40	98.9
A53	5.65	6.64	17.00	56.5	0.14	0.32	5.92	0.541	0.19	0.03	3.65	3.45	100.2
A54	2.10	14.50	6.41	54.1	0.47	<.01	12.50	0.203	0.03	0.13	4.90	3.30	98.7
A55	0.75	16.70	13.30	37.9	0.02	2.57	12.60	0.584	0.03	0.04	5.91	8.50	99.0
A56	4.21	1.69	16.00	64.1	0.18	1.75	3.25	0.840	0.32	0.07	5.77	1.25	99.6
A57	8.23	1.10	18.10	58.1	0.07	0.50	4.70	1.610	0.30	0.04	2.40	2.65	98.0
A62	6.85	3.76	15.50	48.3	0.52	0.08	7.61	1.670	0.05	0.12	8.89	6.55	100.0
CC94	1.07	11.30	14.00	44.6	0.28	2.61	4.35	1.040	<.01	0.08	9.75	10.40	99.6
B1a	2.45	3.12	13.80	60.0	0.14	4.17	3.96	0.463	0.02	0.26	4.05	7.70	100.2
B1b	2.80	2.30	13.30	60.8	0.09	4.06	5.60	0.358	0.03	0.25	2.65	8.05	100.4
B2	4.78	2.72	15.50	51.7	0.38	2.55	6.46	1.110	0.03	0.28	6.79	7.95	100.4
B6	4.32	3.85	15.10	55.9	0.30	3.55	3.82	0.909	0.05	0.26	5.27	6.80	100.3
B7	3.52	3.97	14.40	53.0	0.32	3.39	6.78	0.950	0.06	0.33	5.40	8.05	100.3
B8	4.01	3.12	16.00	64.3	0.05	3.96	0.53	0.682	0.09	0.06	4.78	2.05	99.9
B9	4.12	0.26	11.90	74.4	0.03	2.76	2.56	0.184	0.10	0.02	0.70	2.15	99.3
B10	5.32	0.64	14.20	73.7	0.07	3.25	0.33	0.249	0.10	<0.01	1.31	0.55	99.9

Table 3.5. Continued

C1	1.63	0.67	12.70	66.0	0.13	4.61	4.72	0.492	0.02	0.08	3.29	5.75	100.2
C16	1.07	6.72	11.70	46.0	0.12	4.71	10.60	0.498	0.02	0.15	4.03	14.80	100.6
D2	1.63	4.97	11.90	50.7	0.13	4.25	7.51	0.478	0.03	0.55	5.83	12.20	100.3
D3	2.04	0.77	14.70	70.3	0.10	5.07	0.61	0.599	0.06	0.08	3.54	2.15	100.1
D11	2.54	2.07	15.10	55.6	0.30	5.68	5.04	1.050	0.04	0.49	5.68	6.55	100.3
D13	3.34	2.68	14.20	63.1	0.13	4.62	2.47	0.548	0.09	0.07	5.64	3.20	100.2
D14	0.67	3.91	5.91	19.3	0.07	2.44	34.50	0.193	<0.01	0.44	2.77	30.10	100.4
D17	2.83	4.59	14.00	55.0	0.11	3.10	4.57	0.722	0.04	0.11	8.17	7.00	100.3
D18	3.25	2.77	14.50	62.1	0.12	3.91	3.67	0.488	0.06	0.08	4.93	4.30	100.3
D18	3.19	2.78	15.40	61.2	0.09	4.39	1.55	0.791	0.07	0.09	7.49	3.00	100.2
D20	3.17	2.32	14.30	64.2	0.12	5.01	2.55	0.504	0.05	0.06	4.62	3.15	100.2
D21	1.84	0.22	12.30	65.3	0.07	7.94	4.67	0.298	0.18	<.01	2.91	4.45	100.4
D22	1.37	0.06	13.00	70.2	0.06	9.27	0.75	0.229	0.11	<.01	3.32	1.15	99.7
D24	0.67	2.30	5.79	29.7	0.06	2.44	29.40	0.180	0.03	0.04	2.10	27.50	100.3
D26	0.69	3.47	13.40	52.0	0.21	8.87	5.05	0.723	0.13	0.24	7.06	8.40	100.3

Table 3.6. Silicate $\delta^{18}O$ of separates

Sample	Size	d18O	Yield (micromol/mg)	Sample	Size	d18O	Yield (micromol/mg)
A-24	C	10.1	13.42	B-1a	C	11.7	13.91
A-24	M	11.0	12.73	B-1a	M	11.5	14.23
A-24	M	9.8	10.30	B-1a	F	11.6	12.98
A-24	F	12.7	13.17	B-1b	C	11.4	13.58
A-25	C	6.4	14.06	B-1b	M	10.7	13.39
A-25	M	6.5	12.11	B-1b	M	9.4	12.65
A-25	F	8.1	13.47	B-1b	F	11.4	13.39
A-27	C	10.5	13.90	D-2	C	12.1	14.19
A-27	M	11.5	13.52	D-2	M	10.1	13.17
A-27	F	13.0	13.79	D-2	M	11.7	14.23
A-49	C	9.5	13.53	D-2	F	13.9	13.37
A-49	M	10.7	13.38	D-18	C	8.7	13.97
A-49	F	12.7	13.22	D-18	C	8.7	13.96
A-55	C	10.1	11.09	D-18	M	9.0	12.91
A-55	M	10.9	12.07	D-18	F	12.1	>8.15
A-55	F	11.1	12.16	D-18	F	12.1	11.17

Table 3.7. Samples studied with XRD and PSD. XRD from ExxonMobil Production Research, courtesy of Peter Vrolijk and includes whole rock and clay analyses. PSD data from Vroijk (P), Kate Scharer (S), and Hayman (H).Data is available from the author.

XRD		PSD	
CC94	A55	A3-S	B6-P
A1	A56	A5-S	B7-P
A3	A57	A7-P	B21b-H
A4	A60	A7-S	B21-H
A5	B10	A11-H	C3-P
A6	B1a	A-21-P	C4-P
A7	B1b	A23-P	D2-5-S
A9	B2	A23-P	D2-H
A10	B7	A24-P	D2-P
A11	B8	A26-P	D3-H
A13	B9	A27-P	D3-H
A23	C1	A33-H	D3-P
A24	C16	A33-P	D3-S
A25	D2	A43-P	D5-H
A26	D3	A47-P	D9-H
A27	D11	B10-P	D11-P
A45	D14	B1-3a-S	D14a-S
A47	D18	B1-3b-S	D26-P
A49	D21	B1a-P	
A51	D22	B1b-P	
A52	D24	B2-P	
A53	D26	B2-S	
A54		B3-H	

References

Abbott, R.E., Louie, J.N., Caskey, S.J., Pullammanappallil, S., 2001, Geophysical confirmation of low-angle normal slip on the historically active Dixie Valley Fault, Nevada: Journal of Geophysical Research, v. 106, p. 4169–4181.

Agterberg, F.P., 1974, Geomathematics: Elsevier Science, Amsterdam, 596 p.

An, L.J., and Sammis, C.G., 1994, Particle size distribution of cataclastic fault materials from Southern California; a 3-D study: Pure and Applied Geophysics, v. 143, p. 1-3, 203-227.

Anderson, E.M., 1951, The dynamics of faulting: London, Oliver and Boyd, 206 p.

Axen, G.J., 1999, Low angle normal fault earthquakes and triggering: Geophysical Research Letters, v. 26, p.3693-3696.

Axen, G.J., Fletcher, J.M., Cowgill, E., Murphy, M., Kapp, P., MacMillan, I., Ramos, V.E., and Aranda, G.J., 1999, Range-front fault scarps of the Sierra El Mayor, Baja California: Formed above an active low-angle normal fault?: Geology, v. 27, p. 247–250.

Beeler, N.M., Tullis, T.E., Blanpied, M.L., and Weeks, J.D., 1996, Frictional behavior of large displacement experimental faults: Journal of Geophysical Research, v. 101, p. 8697-8715.

Berthé, D., Choukroune, P., and Jegouzo, P., 1979, Orthogneiss, mylonite, and non-coaxial deformation of granites: the example of the South Armorican Shear Zone: Journal of Structural Geology, v. 1, p. 31-42.

Bird, P., 1984, Hydration-phase diagrams and friction of montmorillonite under laboratory and geologic conditions, with implications for shale compaction, slope stability, and the strength of fault gouge: Tectonophysics, v. 107, p. 235-260.

Blakely, R.J., Jachens, R.C., Clazia, J.P., Langenheim, V.E., 1999, Cenozoic basins of the Death Valley extended terrane as reflected in regional-scale gravity anomalies, in Wright, L.A., and Troxel, B.W., (ed.s), Cenozoic Basins of the Death Valley Region: Special Paper Geological Society of America, v. 333, p. 1-16.

Borradaile, G.J., 1991, Correlation of strain with anisotropy of magnetic susceptibility (AMS): Pure Applied Geophys, v. 135, p. 15-29.

Brogan, G.E., Kellogg, K.S., Slemmons, D.B., and Terhune, C.L., 1991, Late Quaternary faulting along the Death Valley–Furnace Creek Fault System, California and Nevada: U.S. Geological Survey Bulletin, v. 1991, 23 p.

Buck, R.W., 1988, Flexural rotation of normal faults: Tectonics, v. 7, p. 959–973.

Burchfiel, B.C., and Stewart, J.H., 1966, "Pull-apart" origin of the central segment of Death Valley, California: Geological Society of America Bulletin, v. 77, p. 439–441.

Burchfiel, B.C., Molnar, P., Zhang, P., Deng, Q., and Wang, Y., 1995, Example of a supradetachment basin within a pull-apart tectonic setting: Mormon Point, Death Valley, California: Basin Research, v. 7, p. 199–214.

Byerlee, J.D., 1978, Friction of rocks: Pure and Applied Geophysics, v. 116, p. 615-626.

Byrnes, S., 1989, A reconnaissance study of brittle deformation along frontal faults of the Black Mountains, Death Valley, California: [M.Sc. thesis], University of New Orleans, 81 pp.

Caine, J.S., Evans, J.P., and Forster, C.B., 1996, Fault zone architecture and permeability structure: Geology, v. 24, p. 1025-1028.

Chan, M.A., W.T. Parry, and J.R. Bowman, 2000, Diagenetic hematite and manganese oxides and fault-related fluid flow in Jurassic sandstones, southeastern Utah: AAPG Bulletin, v. 84, p. 1281-1310.

Chester, F.M., and Logan, J.M., 1987, Composite planar fabric of gouge from the Punchbowl fault, California: Journal of Structural Geology, v. 9, p. 621-634.

Chester, F.M., and Chester, J.S., 1998, Ultracataclasite structure and friction processes of the Punchbowl fault, San Andreas System, California: Tectonophysics, v. 295, p. 199-221.

Chichanski, M., 2000, Low-angle, range-flank faults in the Panamint, Inyo, and Slate Ranges, California: Implications for recent tectonics of the Death Valley region: Geological Society of America Bulletin, v. 112, p. 871–883.

Cladouhos, T.T., 1999a, Shape preferred orientations of survivor grains in fault gouge: Journal of Structural Geology, v. 21, p. 419-436.

Cladouhos, T.T., 1999b, kinematic model for deformation within brittle shear zones: Journal of Structural Geology, v. 21, p. 437-448.

Cowan, D.S., 1999, Do faults preserve a record of seismic slip – a field geologist's opinion, 1999, Journal of Structural Geology, v. 21, p. 2703-2719.

Cowan, D.S., Cladouhos, T.T., and Morgan, J., 2003, Structural geology and kinematic history of rocks formed along low-angle normal faults, Death Valley, California: Geological Society of America Bulletin, v. 115, in press.

Cowan, D.S., and Brandon, M.T., 1994, A symmetry based method for kinematic analysis of large-slip brittle fault zones: American Journal of Science, v. 294, p. 257-306.

Curry, H. D., 1938, "Turtleback" fault surfaces in Death Valley, California: Geological Society of America Bulletin, v. 49, p. 1874-1875.

Dahlen, F.A., 1984, Noncohesive critical Coulomb wedges: An exact solution: Journal of Geophysical Research, v. 89, p. 10,125–10,133.

Drewes, H., 1963, Geology of the Funeral Peak Quadrangle, California, on the eastern flank of Death Valley: U.S. Geological Survey Professional Paper 413, p. 78.

Dunlop, D.J., and Özdemir, O., 1997, Rock magnetism: fundamentals and frontiers, Cambridge: Cambridge University Press, 573 pp.

Essene, E.J., and Peacor, D.R., 1995, Clay mineral thermometry – A critical perspective: Clays and Clay Minerals, v. 43, p. 540-553.

Evans, J.P., and Chester, F.M., 1995, Fluid-rock interaction in faults of the San Andreas system; inferences from San Gabriel Fault rock geochemistry and microstructures: Journal of Geophysical Research, v. 100, p. 13,007-13,020.

Feng, X., Faiia, A.M., WoldeGabriel, G., Aronson, J.L., Poage, M.A, Chamberlain, C.P, 1999, Oxygen isotope studies of illite/ smectite and clinoptilolite from Yucca Mountain; implications for paleohydrologic conditions: Earth and Planetary Science Letters, 171, p. 95-106.

Garrels, R.M., and Christ, C.L., 1965, Solutions, Minerals, and Equilibria: Freeman, Cooper & Co, San Francisco, CA, 449 pp.

Ghosh, S.K., and Ramberg, H., 1976, Reorientation of inclusions by combination of pure shear and simple shear: Tectonophysics, v. 34, p. 1-70.

Giggenbach, W.F., 1985, Construction of thermodynamic stability diagrams involving dioctahedral potassium clay minerals: Chemical Geology, v. 49, pp. 231-242.

Grant, J.A., 1986, The isocon diagram – a simple solution to Gresens' equation for metasomatic alteration, Economic Geology, v. 81, p. 1976-1982.

Hamilton, W.B., 1988, Detachment faulting in the Death Valley region, California and Nevada: U.S. Geological Survey Bulletin 1790, p. 51–85.

Hargraves, R.B., Johnson, D., and Chan, C.Y., 1991, Distribution anisotropy: The cause of AMS in igneous rocks?: Geophysical Research Letters, v. 18, p. 2193-2191.

Hayman, N.W., Knott, J.R., Cowan, D.S., Nemser, E., and Sarna-Wojcicki, A., 2003, Quaternary low-angle slip on detachment faults in Death Valley, California: Geology, v. 31, p. 343-346.

Helgelson, H.C., Brown, T.H., and Leeper, R.H., 1979, Handbook of Theoretical Activity Diagrams Depicting Chemical Equilibria in Geologic Systems Involving an Aqueous Phase at One Atm and 0° to 300°C: Freeman, Cooper & Co, San Francisco, CA, 253 pp.

Holm, and Dokka, 1993, Interpretation and tectonic implications of cooling histories; an example from the Black Mountains, Death Valley extended terrane, California: Earth and Planetary Science Letters, v. 116, p. 63-80.

Holm, D.K., Fleck, R.J., and Lux, D.R., 1994, The Death Valley Turtlebacks reinterpreted as Miocene–Pliocene folds of a major detachment surface: Journal of Geology, v. 102, p. 718–727, 1994.

Housen, B.A., Richter, C., and van der Pluijm, B.A., 1993, Composite magnetic anisotropy fabrics: experiments, numerical models, and implications for the quantification of rock fabrics: Tectonophysics, v. 220, p. 1-12.

Hower, J., Eslinger, E.V., Hower, M.E., and Perry, E.A., 1976, Mechanisms of burial metamorphism of argillaceous sediments: 1. Mineralogical and chemical evidence, Geological Society of America Bulletin, v. 87, p. 725-737.

Huang, W.L., Longo, J.M., and Pevear, D.R., 1993, An experimentally derived kinetic model for smectite-to-illite conversion and its use as a geothermometer: Clays and Clay Minerals, v. 41, p. 162-177.

Jackson, M., 1991, Anisotropy of Magnetic Remnance: A brief review of mineralogical sources, physical origins, and geological applications, and comparison with susceptibility anisotropy: Pure and Applied Geophysics, v. 136, p. 1-28.

Jackson, J.A., and White, N.J., 1989, Normal faulting in the upper continental crust: Observations from regions of active extension: Journal of Structural Geology, v. 11, p. 15–36.

Jeffery, G.B., 1922, The motion of ellipsoidal particles immersed in a viscous fluid: Proceedings of the Royal Society of London, v. 102, p. 161-179.

Jelinek, V., 1978, Statistical processing of anisotropy of magnetic susceptibility measured on groups of specimens: Studia Geophysica et Geodetica, v. 22, p. 50–62.

Je˘zek , J. and Hrouda, F., 2002, Software for modeling the magnetic anisotropy of strained rocks: Computers and Geosciences, v. 28, p. 1061-1068.

Keener, C., Serpa, L.F., and Pavlis, T.L., 1993, Faulting at Mormon Point, Death Valley, California: A low-angle normal fault cut by high-angle faults: Geology, v. 21, p. 327–330.

Knipe, R.J., 1992, Faulting processes and fault seal, in R.M. Larsen, ed., Structural and tectonic modeling and its application to petroleum geology: Stavanger, NPF (Norwegian Petroleum Society), p. 325-342.

Knott, J.R., Sarna-Wojcicki, A.M., Meyer, C.E., Tinsley III, J.C., Wells, S.G., and Wan, E., 1999, Late Cenozoic stratigraphy and tephrochronology of the western Black Mountains piedmont, Death Valley, California: Implications for the tectonic development of Death Valley, in Wright, L.A., and Troxel, B.W., eds., Cenozoic basins of the Death Valley region: Geological Society of America Special Paper 333, p. 345–366.

Kodama, K.P. and Sun, W.W., 1990, SEM and magnetic fabric study of a compacting sediment: Geophys. Res. Letter, v. 17, p. 795-798.

Ku, T.H., Luo, S., Lowenstein, T.K., Li, J., and Spencer, R.J., 1998, U-series chronology of lacustrine deposits in Death Valley, California: Quaternary Research, v. 50, p. 261–275.

Lanphere, M.A., Champion, D.E., Christiansen, R.L., Izett, G.A., and Obradovich, J.D., 2002, Revised ages for tuffs of the Yellowstone Plateau volcanic field: assignment of the Huckleberry Ridge Tuff to a new geomagnetic polarity event: Geological society of America Bulletin, v. 114, p. 559-568.

Linde, A.T., Gladwin, M.T., Johnston, M.J., Gwyther, R.L., Bilham, R.G., A slow earthquake sequence on the San Andreas fault, Nature, v. 383, p. 65-68.

Logan, J.M., Friedman, M., Higgs, N., Dengo, C., and Shimanto, T., 1979, Experimental studies of simulated gouge and their application to studies of natural fault zones. *in* Proceedings of Conference VIII on Analysis of Actual Fault Zones in Bedrock: U.S. Geological Survey Open-File Report 79-1239.

March, A., 1932, Mathematische theorie der regelung nach der korngestalt bei affiner deformation: Zeitschrift fur Kristallographie, v. 81, p. 285-297.

Manastchal, G., Marquer, D., Fruh-Green, G.L., 2000, Channelized fluid flow and mass transfer along a rift-related detachment fault (Eastern Alps, southeast Switzerland): Geological Society of America Bulletin, v. 112, p. 2-33.

Manastchal, G., 1999, Fluid- and reaction-assisted low-angle normal faulting; evidence from rift-related brittle fault rocks in the Alps (Err Nappe, eastern Switzerland): Journal of Structural Geology, v. 21, p. 777-793.

Marone, C., Raleigh, C.B., Scholz, C.H., 1990, Frictional behavior and constitutive modeling of simulated fault gouge: Journal of Geophysical Research, v. 95, p.7007-7025.

Marone, C., and Scholz, C.H., 1989, Particle-size distribution and microstructures within simulated fault gouge: Journal of Structural Geology, v. 11, p. 799-814.

Miller, M.G., 1991, High-angle origin of the currently low-angle Badwater Turtleback fault, Death Valley, California: Geology, v. 19, p. 372–375.

Miller, M.G., 1992a, Structural and Kinematic Evolution of the Badwater Turtleback, Death Valley, California: [Ph.D. thesis: Seattle, WA] xxx pp..

Miller, M.G., 1992b, Brittle faulting induced by ductile deformation of a rheologically stratified rock sequence, Badwater Turtleback, Death Valley, California: Geological Society of America Bulletin, v. 104, p. 1376-1385.

Miller, M.G., 1996, Ductility in fault gouge from a normal fault system, Death Valley, California: A mechanism for fault-zone strengthening and relevance to paleoseismicity: Geology, v. 24, p. 603–606.

Miller, M.G., and Friedman, R.M., 1999, Early Tertiary magmatism and probable Mesozoic fabrics in the Black Mountains, Death Valley, California: Geology, v. 27, p. 19-22.

Miller, M.G., 2003, Basement-involved thrust faulting in a thin-skinned fold-and-thrust belt, Death Valley, California, USA: Geology, v. 31, p. 31-34.

Miller, M.G., and T.L. Pavlis. 2003, The Black Mountains turtlebacks: Rosetta stones of Death Valley tectonics: Earth Science Reviews (in press).

Miller, M.M., Johnson, D.J., Dixon, T.H., and Dokka, R.K., 2001, Refined kinematics of the Eastern California shear zone from GPS observations, 1993-1998: Journal of Geophysical Research, v. 106, p. 2245-2263.

Mitchell, J.K., 1993, Fundamentals of Soil Behavior: Wiley, NY, 437 p.

Morgan, J.K., Cladouhos, T.T., Scharer, K.M., Cowan, D.S., Vrolijk, P.J., 1996, Fractal particle size distributions in Death Valley fault zones; controls on mechanics and kinematics of fault rocks: Eos, Transactions, American Geophysical Union, v.77, p. 717-718.

Morgan, J.K., 1999, Numerical simulations of granular shear zones using the distinct element method 2. Effects of particle size distribution and interparticle friction on mechanical behavior: Journal of Geophysical Research, v. 104, p. 2721-2732.

Morgan, J.K., and Boettcher, M.S., 1999b, Numerical simulations of granular shear zones using the distinct element method; 1, Shear zone kinematics and the micromechanics of localization: Journal of Geophysical Research, v. 104, p. 2703-2719.

Morrow, C. A., Moore, D. E., Lockner, D. A., 2000, The effect of mineral bond strength and adsorbed water on fault gouge frictional strength: Geophysical Research Letters, v. 27, p. 815-818.

Nadeau, P.H., 1994, Fundamental Particles: An informal history, Clay Minerals, v. 34, p.185-191.

Nemser, E.S., 2001, Kinematic development of upper plate faults above low-angle normal faults in Death Valley, California [M.S. thesis]: Seattle, University of Washington, 102 p.

Nye, J.F., 1985, Physical Properties of Crystals: Oxford Science Publications, Oxford University Press, 329 p.

Oertel, G., 1985, Reorientation due to grain shape, in H.-R. Wenk (Ed.), Preferred Orientation in Deformed Metals and Rocks: An Introduction to Texture Analysis: Academic Press, London, p. 259-266.

Otsuki, K., Monzawa, N., Nagase, T., 2003. Fluidization and melting of fault gouge during seismic slip: Identification in the Nojima fault zone and implications for focal earthquake mechanisms: Journal of Geophysical Research, v. 108, doi:10.1029/2001JB001711.

Otton, J.K., 1977, Geology of the central Black Mountains, Death Valley, California [Ph.D. thesis]: University Park, Pennsylvania State University, 155 pp.

Pavlis, T.L., Serpa, L.F., Keener, C., 1993, Role of seismogenic processes in fault-rock development; an example from Death Valley, California: Geology, v. 21, p. 267-270.

Postma, D., and Appelo, C.A.J., 2000, Reduction of Mn-oxides by ferrous iron in a flow system: Column experiment and reactive transport modeling: Geochimica et Cosmochimica Acta, v. 64, p. 1237-1247.

Reinen, L.A., Seismic and aseismic slip indicators in serpentinite gouge, Geology, v.28, p.135-138.

Richter, C., 1991, Particle motion and the modeling of strain response in magnetic fabrics: Geophysical Journal International, v. 110, p. 451-464.

Roberson, H.E., Reynolds, R.C Jr., and Jenkins, D.M., 1999, Hydrothermal synthesis of corrensite; a study of the transformation of saponite to corrensite, Clays and Clay Minerals, v. 47, p. 212-218.

Rochette P, Aubourg C, Perrin M, 1999, Is this magnetic fabric normal? A review and case studies in volcanic formations: Tectonophysics, v. 307, p. 219-234.

Rutter, E.H., 1983, Pressure solution in nature, theory, and experiment: Journal of the Geological Society of London, v. 140, p. 725-740.

Rutter, E.H., 1986, On the nomenclature of mode of failure transitions in rocks: Tectonophysics, v. 122, p. 381-387.

Rutter, E.H., Maddock, R.H., and Hall, S.H., 1986, Comparative microstructures of natural and experimentally produced clay-bearring fault gouges: Pure and Applied geophysics, v. 124, p. 3-30, 1986.

Sammis, C.G., King, G., Biegel, R., 1987. The kinematics of gouge deformation: Pure and Applied Geophysics, v. 125, p. 777-812.

Sanderson, D.J., and Marchini, W.R.D., 1984, Transpression: Journal of Structural Geology, v. 6, p. 449-458.

Sander, B., Gefugekene der Gesteine, Springer, Vienna, 352 pp, 1930.

Sass, J.H., Lachenbruch, A.H., Galanis, S.P. Jr., Morgan, P., Priest, S.S., Moses, T.H. Jr., Munroe, R.J., 1994, Thermal regime of the southern Basin and Range Province; 1,

Heat flow data from Arizona and the Mojave Desert of California and Nevada. Journal of Geophysical Research, v. 99, p. 22,093-22,119.

Scharer, K. 1996, Particle Size Distribution of Death Valley fault rocks, University of Washington senior thesis, 50pp.

Schmidt, S.T., and Robinson, D., 1997, Metamorphic grade and porosity and permeability controls on mafic phyllosilicate distributions in a regional zeolite to greenschist facies transition of the North Shore Volcanic Group, Minnesota, Geological Society of America Bulletin, v.109, p. 683-697.

Scholz, C.H., 1998, Earthquakes and friction laws: Nature, v. 391, p. 37-42.

Sibson, R.H., 1977, Fault rocks and fault mechanisms: Journal of the Geological Society of London, v. 133, p. 191-213.

Sibson, R.H., 1992, Implications of fault-valve behavior for rupture nucleation and recurrence: Tectonophysics, v. 211, p. 283-293.

Snow, J.K., Wernicke, B.P., 2000, Cenozoic tectonism in the central Basin and Range; magnitude, rate, and distribution of upper crustal strain: American Journal of Science, v. 300, p. 659-719.

Tarling, D.H. and Hrouda, F., 1993, The Magnetic Anisotropy of Rocks: Chapman & Hall, London, 217 pp.

Tchalenko, J.S., 1968, The evolution of kink-bands and the development of compression textures in sheared clays: Tectonophysics, v. 6, p. 159-174.

Tikoff, B., and Teyssier, C., 1994, Strain modeling of displacement-field partitioning in transpressional orogens, Journal of Structural Geology, v. 16, p.1575-1588.

Tullis, J., 1990. Experimental studies of deformation mechanisms and microstructures in quartzo-feldspathic rocks, in Barber, D.J., and Meredith, P.G., Deformation Processes in Minerals, Ceramics, and Rocks: Urwin Hyman, London, p. 190-227.

Turcotte, D.L., 1992, Fractals and Chaos in Geology and Geophysics: Cambridge University Press, NY, 221 pp.

Vrolijk, P.J., Cladouhos, T.T., D.S. Cowan, and J. Morgan, 1997, Importance of alteration reactions for the Death Valley fault zone: Abstracts with Programs-Geol. Society of America, 29, 258.

Vrolijk, P. and van der Pluijm, B.A.,1999, Clay gouge: Journal of Structural Geology, v. 21, p. 1039-1048.

Wald, D.J., and Heaton, T.H., 1994, Spatial and Temporal distribution of slip for the 1992 Landers, California, earthquake, Bulletin of the Seismological Society of America, v. 84, p. 668-691.

Wernicke, B., 1985, Uniform-sense normal simple shear of the continental lithosphere: Canadian Journal of Earth Science, v. 22, p. 108–125.

Wernicke, B., and Axen, G.J., 1988, On the role of isostacy in the evolution of normal fault systems: Geology, v. 16, p. 848-851.

Wernicke, B., 1995, Low-angle normal faults and seismicity: A review: Journal of Geophysical Research, v. 100, p. 20,159–20,164.

Wernicke, B., Friedrich, A.M., Niemi, N.A., Bennett, R.A., and Davis, J.L., 2000, Dynamics of plate boundary fault systems from Basin and Range Geodetic Network (BARGEN) and geologic data: GSA Today, v. 10, n. 11, p. 1–6.

Wintsch, R.P., Christoffersen, R., Kronenberg, A.K., 1995, Fluid-rock reaction weakening of fault zones: Journal of Geophysical Research, v. 100, p. 20159-20174.

Wills, S., and Buck, R.W., 1997, Stress-field rotation and rooted detachment faults: A Coulomb failure analysis: Journal of Geophysical Research, v. 102, p. 20,503–20,514.

Wolf, D.E., 1998, Modeling and computer simulation of granular media, *in* Herrmann, H.J., Hovi, J.P., and Luding, S. (ed.s) Physics of Dry Granular Media, NATO ASI series. Series E, Applied sciences, 350.

Wright, L.A., Otton, J.K., and Troxel, B.W., 1974, Turtleback surfaces of Death Valley viewed as phenomena of extensional tectonics: Geology, v. 2, p. 53–54.

Wright, L.A., Troxel, B.W., 1984, Geology of the northern half of the Confidence Hills 15-minute Quadrangle, Death Valley region, eastern California; the area of the Amargosa chaos. Map Sheet: California Division of Mines and Geology, 34.

Wu, F.T., 1978, Mineralogy and physical nature of clay gouge, *in* Rock friction and earthquake prediction, editors Byerlee, J, D, Wyss, M: Pure and Applied Geophysics, v. 116, p. 655-689.

Xiao, H.B., Dahlen, F.A., and Suppe, J., 1991, Mechanics of extensional wedges: Journal of Geophysical Research, v. 96, p. 10,301–10,318.

Yonkee, W.A., Parry, W.T., and Bruhn, R.L., 2003, Relations between progressive deformation and fluid-rock interaction during shear-zone growth in a basement-cored thrust sheet, Sevier orogenic belt, Utah: American Journal of Science, v. 303, p. 1-59.

Appendix 1

A Matlab script that solves the Coulomb wedge problem (Dahlen, 1984) for different values of bmu, the coefficient of friction on the detachment. Cohesion and fluid pressure are not considered.

```
hold off
clear
%figure

%parameters

N = 10001;
phi = 30*pi/180;
phib=21*pi/180;
bmu=tan(phib);

%Sean's minimization function

psib=zeros(length(phib),2);

test=zeros(N,1);

j=1;
test(1)=0;
for i=2:N

  psi=(i-1)*3.141592/20000.;

  test(i)=(tan(2.*psi)/((1./sin(phi))*(1./cos(2.*psi))-1.))-bmu;

  sign=test(i)*test(i-1);
  if(sign < 0.0)
    sign=test(i)*test(i-1);
  if(sign < 0.0)
    psi1=(i-2)*3.141592/20000.;
    if(test(i)-test(i-1) == 0.0)
    psib(j)=-1.*psi;
    else
    psib(j)=-1.*(psi1+(-test(i-1)/(test(i)-test(i-1)))*(psi-psi1));
    end
    j=j+1;
    if(j == 3) break; end
  end
end

end

% Plot function beta,alpha

psio = -pi+.1:.01:pi-.1;
alpha = atan(tan(2.*psio)./(csc(phi)*sec(2*psio)-1));

beta1 = psib(1)-psio-alpha;
beta2 = psib(2)-psio-alpha;
plot(beta1.*180/pi,alpha.*180/pi, 'b', beta2.*180/pi,alpha.*180/pi, 'b')
f_psi=(tan(2.*psi))./(csc(phi).*sec(2.*phi)-1)
```

Vitae

Nicholas Waln Hayman was born in Brooklyn, New York, December 23, 1972. He graduated, *magna cum laude*, from the State University of New York at Albany in 1995 with a bachelor of science. During his undergraduate education he received a student research fellowship from the National Science Foundation to study magnetic anomalies on the East Pacific Rise as a summer intern at Lamont Doherty Earth Observatory, Columbia University. He remained at SUNY Albany and completed a Master of Science with a thesis titled "Pre-thrust normal faults and Post-tectonic micas in the Champlain-Taconic thrust system, West-Central Vermont". One portion of this work was published in a peer reviewed paper: "Reactivation of prethrusting, synconvergence normal faults as ramps within the Champlain-Taconic thrust system" (by Hayman, N.W., and Kidd, W.S.F., Geological Society of America Bulletin, v. 114, p.476-489) and a second paper on slate microstructure is in progress. While attending University of Washington, Hayman has worked as a summer intern with Chevron Production Research, visited fault localities in Death Valley and worldwide, and published one peer reviewed paper:"Low angle slip on detachment faults in Death Valley, California" (by Hayman, N.W., Knott, J., Cowan, D.S., Nemser, E., and Sarna-Wojcicki, A.M., Geology, v.31, p.343-346). He is currently preparing articles on topics including magnetic fabrics, fault-rock petrology, and the kinematics and mechanics of Death Valley, CA. He has presented research at several professional meetings and field conferences and contributed to several publications by other authors. Most recently, Hayman coauthored a funded proposal to the National Science Foundation, Marine geology and geophysics division, with Jeff Karson (Duke University) entitled "Investigation of Fault Rocks from Lavas and Sheeted Dikes of the Fast-Spread Oceanic Crust: Microstructure, Fluid Interactions, and Implications for Spreading Processes". When not studying geology, Hayman enjoys martial arts and science fiction novels. He received his doctorate of philosophy from the Department of Earth and Space Sciences, University of Washington, in 2003.